Changes in Material Characteristics of AISI 430 Stainless Steel Plates Subjected to Repeated Blast Loading

BISRU

BLAST IMPACT AND SURVIVABILITY RESEARCH UNIT

CME

Centre for Materials Engineering

Student: Thobani Paul Shangase

Supervised by:

Dr. Steeve Chung Kim Yuen and Dr. Sarah George

Submitted to the University of Cape Town for the fulfilment of the degree of MSc in Mechanical Engineering

April 2017

PLAGIARISM DECLARATION

I, Thobani Paul Shangase, hereby:

(a) Grant the University free license to reproduce this thesis, entitled "**Changes in Material Characteristics of AISI 430 Stainless Steel Plates Subjected to Repeated Blast loading**", in whole or in part, for the purpose of research.

(b) Declare that:

(i) This thesis is my own, both in conception and execution, and that apart from the normal guidance of my supervisor; I have received no assistance apart from that stated in the "Acknowledgements" section of the thesis.

(ii) This thesis or any part of this thesis has not been submitted in past, or is being, or is to be submitted in this or any other form for a degree at the University of Cape Town or any other University according to best of my knowledge.

(iii) I am now presenting this thesis entitled "**Changes in Material Characteristics of AISI 430 Stainless Steel Plates Subjected to Repeated Blast loading**" for examination for the degree of MSc. in Mechanical Engineering

Signed by candidate

Signature

ABSTRACT

Structures deform at high strain rates and temperatures when exposed to impulsive loads. To accommodate the macro change there are microstructural changes that occur, i.e., grain morphology and shear banding. Most studies report on macroscopic response, i.e., large inelastic deformation and tearing of the structure, while limited studies have reported on microscopic changes that develop in the structure. The microstructure is directly related to the mechanical properties and performance of the material. Therefore, understanding the effect of high strain rate loadings on the microstructural evolution and subsequent mechanical properties of metals and alloys is necessary for mechanical design.

The main objective of this research was to investigate microstructural changes to characterise the strain distribution and plastic deformation, owing to impulsive loading. Features within the microstructure that could be used to characterise deformation included grain size morphology changes, the presence of shear bands and sub-grain networks. The electron backscatter diffraction (EBSD) technique, which used Kikuchi patterns to characterise the strain distribution in the crystal of the deformed material, was also used as a characterisation tool.

The first step in the experimental procedure was to select the appropriate material to investigate these microstructural changes. There was also the systematic investigation into the use of single and double heat treatments. These were used to achieve a large equiaxed grain structure, which was desirable from a microstructural point of view but was not desirable for blast-resistant material selection. The two-step heat treatment was concluded to be the most suitable heat treatment for the annealing and homogenisation of the AISI 430 stainless steel plates. The AISI 430 stainless steel plates used were 244 mm by 244 mm in size and had a circular exposed area of 106 mm. These plates were subjected to repeated explosive blasts, using a plastic explosive (PE4). The charge mass was varied for each test and the stand-off distance was kept constant at 150 mm for uniform loads and 13 mm for localised loads. Two plates were selected to investigate the uniform loading scenario. The first plate, a torn plate, used a charge mass of 30 g and one blast and the second plate, an inelastically-deformed plate, used a charge mass of 10 g and was exposed to three blasts. These two plates offered the same overall charge load with a different strain path. A further two plates were chosen for the investigation into the localised loading scenario. One plate, a petalled plate, used a 6 g charge mass and was exposed to two blasts and the second plate, an inelastically-deformed plate, used a 5 g charge mass and was also exposed to two blasts. The latter two plates offered an investigation into the effect of an increased charge load, where charge load affected the strain rate of the deformation resulting from the blast load. All four plates were sectioned across the midline of the dome and then ground and polished to a mirror finish, using OP-S. The polished samples were analysed, using optical microscopy and EBSD. In addition, Vickers hardness tests were carried out along the midline of the sectional plate profiles, in order to evaluate the extent of strain hardening.

All the plates showed either a response of inelastically deforming or of complete or partial tearing failures when subjected to blast loads. For inelastic deformation failures, a global dome was characteristic of the uniform loading condition and an inner dome superimposed by the global dome was characteristic of the localised loading condition. Variation of charge mass and the number of blasts showed an increasing linear relationship between the impulse and midpoint deflection. The macrostructure showed a large variation of failures in the localised condition. The microstructural characterisation results produced micrographs showing regions of long, flat grains with multiple sub-grain networks, indicating deformed microstructures of the blast loaded plates. Parts of the microstructures displayed equiaxed/recrystallised grains characteristic of restoration processes, owing to high temperatures. Vickers hardness tests indicated an increase in material hardness as the number of blasts was increased, with a maximum hardness in the central region of the plates.

In the first investigation, into uniform loading, the material characterisation results, combined with the fractography results, indicated brittle failure modes typical of high strain rate failures in strain rate sensitive materials, such as the chosen AISI 430 stainless steel plates. In the second investigation, into localised loading, the material characterisation results, combined with the fractography results, indicated a more ductile failure, owing to a 1 g incremental increase of charge mass, which confirmed the strain rate sensitivity of this material.

ACKNOWLEDGEMENTS

Being an individual who comes from a background where no one has had the advantage of acquiring a degree, being offered an opportunity to study for this degree in a top research university has been a blessing. Therefore, I would like to thank the head of Department of Mechanical Engineering, Professor Robert Knutsen, and the deputy head, Professor Genevieve Langdon, for trusting and believing in my ability to start this research and bring it to conclusion. Secondly, I would not have been able to finish this research without the support and patience of my supervisors, Dr Steven Chung Kim Yuen and Dr Sarah George. I know that the generosity, patience and love they have in believing in the capability of students will be extended to other students in need. With that said, thank you a million times. I am aware that words cannot describe how truly grateful I am. But may you continue to be this wise and blessed.

The numerous times of stressing and crying in the laboratories resulted in my asking a lot of questions and searching for frequent assistance from various hands. The guidance of my colleagues, Christopher Long, Dale Warncke and Vinay Shekhar, is very much appreciated. The generosity of Dr Miranda Waldron and Dr Innocent Shuro, who helped me in the analysis of my samples, is what led to the good micrographs and material characteristics produced during this research. I am thankful for their participation and patience. Without them I would not have the knowledge I've acquired today. The assistance of Velile Vilane, Karin Kafer, Sherlyn Gabriels and Candice Mias will never be forgotten. I would like to thank them for always being at my beck and call.

Lastly, I would like to extend a word of thanks to my manager and mentor, Dr Rembu Magoba, and Professional Officer, Mercia Volschenk, for their endless help. Thank you also to Mrs George for her editing and my parents for their limitless love and support.

TABLE OF CONTENTS

LIST OF FIGURES

List of Tables

GLOSSARY

ASB	Adiabatic Shear Bands
BISRU	Blast Impact and Survivability Research Unit
EBSD	Electron Backscatter diffraction
IEDs	Improvised Explosive Devices
UTS	Ultimate Tensile Strength
YS	Yield Strength
SEM	Scanning Electron Microscopy

NOMENCLATURE

Upper Case

A_0 — Loaded Area

A —Plate area

C —Damping coefficient

D —Plate diameter

H —Plate thickness

I —Impulse

L —Half plate length

M_0 — Plate moment

Po —Ambient pressure

R —Plate radius

R_0 —Charge radius

S —Stand-off distance

T —Period of Oscillation

V_0 —Initial velocity

Lower Case

d – Grain diameter

m_p – Pendulum total mass

h – Charge height

Greek Lower Case

α – Johnson's Damage number (circular)

γ – Stand-off distance parameter

δ -Midpoint deflection

ε – Material strain

ζ_c -Loading parameter (circular plates)

λ –Jones Damage number

μ - Mass per unit area (ρH)

ρ - Material density

σ_o -Static yield stress of material

σ_d - Damage stress

σ_y –Yield strength

Φ_c – Nurick and Martin damage

CHAPTER 1

1 Introduction

1.1 Background to project

Landmines and Improvised Explosive Devices (IEDs) represent a considerable threat to military vehicles, peace-keeping missions and medical vehicles. Owing to exposure to landmines, these vehicles can be subjected to repeated blast loads. Repeated blast loading leads to different types of macroscopic responses of the material used in their construction. This structural response depends on the numerous parameters of these blast loads, such as the stand-off distance, the charge mass and the environment (air or sand). The macro-response of single plates to various types of blasts has been studied by many researchers. However, very few studies have focused on changes in the material at a microscopic level.

These microstructural changes in the metal affect the overall material behaviour and mechanical properties of the material under study. Therefore, it is important to investigate the microstructural and mechanical property changes of the material for future design. These changes must involve an assessment of the resistance of the material in question.

1.2 Research Problem Statement

This research was an investigation into the microstructural changes and mechanical properties of AISI 430 stainless steel plates that had been subjected to repeated blast loads. The aim of this research was to study the microstructural evolution that occurred in this material during plastic deformation, as a result of blast loading, under a range of different charge masses and number of blast loads.

1.3 Objectives of project

The objectives of this study were:

a. To determine the effects of uniform and localised loading conditions on the chosen material, AISI 430 stainless steel.
b. To use microstructural features and morphological changes to describe the effect of loading conditions on this material.
c. To use microstructural evolution and mechanical property data to evaluate the choice of AISI 430 stainless steel as a blast resistant material.
d. To draw appropriate conclusions from the findings.
e. To draw recommendations based on the conclusions.

1.4 Constraints of the project

The scope of this investigation was limited to 2 mm thick circular plates with an exposed area of 0.106 m^2, which would be subjected to repeated blast loading, using charge diameters of 34 mm, 40 mm and 25 mm.

1.5 Outline of dissertation

This study contains a literature review in Chapter 2 that explores the material characteristics, types of loadings, studies on impulsive loading of structures, specimen responses and research on microstructural changes. The experimental details and procedures are outlined in Chapter 3. This chapter depicts the two types of loading conditions (uniform and localised loading) used in this project. In Chapter 4, the experimental observations are detailed and discussed, in words or in tabular, graphic or photographic formats. In Chapter 5, micrographs and mapping information of the deformed, cracked and torn plates are presented and discussed, and correlated with previous studies available in open literature. Finally, in Chapters 6 and 7 respectively, conclusions are drawn and recommendations are made for any future research.

CHAPTER 2

2. Literature review

2.1 Material characteristics

2.1.1 Introduction

Materials are likely to be deformed by loads in the period of their lifetime. Most deformations are caused by a stress applied either *quasi*-statically or dynamically. Therefore, it is important to understand how material mechanical properties depend on deformation conditions. According to Sierakowski [1], the variation in material properties with applied strain rate was an important consideration in the mechanical designs of materials used in structures subjected to applied loads. The variation of the engineering stress-strain curve with loading rate was attributed to the microscopic changes taking place in the material. Nangajaro *et al.* [2] demonstrated that the yield stress of steel was affected by the strain rates that are only above $10^{-3}s^{-1}$. A metal could have an infinite number of such values, depending on the definition. Therefore, the speed of testing was important when defining yield stress.

According to Roylance [3], an increase in the loading of the material was accompanied by a large increase in the strain of the material. The relationship between the loading rate and the material strain was influenced by the microstructure of the material. Moreover, Gere *et al*. [4] showed that there were different types of loading modes, depending on the loading rate. However, materials were designed to resist more than one type of loading mode and sometimes combined loading modes, such as bending stress, while there was shear stress being applied. A structure subjected to a number of loadings at once could often be analysed by superimposing the stresses and strains caused by each load acting separately. If the loading rate was slow, the material was said to be loaded *quasi*-statically and if the loading rate was fast it was said to be dynamic.

2.1.2 *Quasi*-static loading

A complete detailed description of a material's behaviour requires information about the response of a material as a function of strain, stress, strain rate and temperature. At low strain rates the load is *quasi*-static. This means that the load is applied slowly, with the result that the structure deforms correspondingly slowly. Therefore, the inertia force is very small and can be ignored. A *quasi*-static deformation process, although time-dependent, is in reality a sequence of states in static equilibrium. Typical illustrations of a *quasi*-static deformation process are creep and relaxation processes of materials.

At strain rates of 10^{-3} s^{-1} to 10^{-5} s^{-1}, Hecker *et al*. [5] investigated the effect of the strain state and strain rates on the mechanical properties and failure mechanisms of AISI 304 stainless steel. Uniaxial tensile tests were conducted in an Instron machine at a strain rate of $10^{-3}s^{-1}$. The results indicated high strain rate sensitivity in this metal. In addition, there was an increase in the ultimate and yield strengths as the strain rate was increased. Moreover, there was emphasis on strong temperature dependence on strain-induced martensitic transformation in the vicinity of room temperature.

In another study by Hadianfard *et al*. [6], engineering tensile tests were performed on aluminium alloys AA5754 and AA5182 at strain rates of less than 10^{-1} s^{-1}. The results indicated negative strain rate sensitivity in these alloys. However, in these tests both the ultimate and yield strengths were reduced as the strain rate was increased. In addition, there was a decrease in the flow stresses, and the strains to failure tended to decrease as the strain rates were increased. Similar results were obtained by Khan and Krempl [7] when they investigated the dependence of mechanical properties on the rate of deformation. Therefore, from these studies it could be observed that stress-strain diagrams, obtained under various constant loading rates, displayed typical elastic response and a subsequent transition to a plastic response, where elastic response was independent of strain rate, and plastic response was highly dependent on the strain rates. Other studies were by Holzapfel *et al*. [8], who described material response and mechanical behaviour deformation in terms of the strain rates.

Tiamiyu *et al*. [9] studied the response of AISI 321 austenitic stainless steels, stabilised with titanium addition, for *quasi*-static loading. This was known to be an attractive material for load-bearing applications. *Quasi*-static compression was conducted using the Instron R5500 mechanical testing system, with a maximum load cell of 150 kN. The specimen was exposed to compressive load at a crosshead speed of 1 mm/min, which generated a strain rate of 4.2×10^{-3} s^{-1}. The results of the tests displayed that, as the deformation proceeded beyond the yield point, strain hardening dominated the deformation process throughout the *quasi*-static compression test.

Material response to *quasi*-static loading depends upon the stress level of the material. The stress-strain relationship may be non-linear and responds according to how the material is loaded. *Quasi*-static tests are performed by imposing pre-defined displacement or force histories on the testing specimen. Singh *et al.* [10] stated that the engineering stress-strain diagram depended on the rate of loading and the loading rate was usually kept constant for loading and unloading in the *quasi*-static state, as displayed by Figure 2.1.

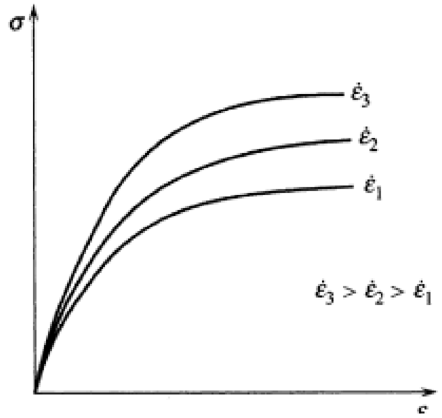

Figure 2.1: Graph of σ vs ε, showing the effects of loading rate [10].

2.1.3 High strain loadings

When the loading rate is high, the mechanical response of a material is generally different from what it would be at a lower loading rate. High strain rate loadings are achieved by impact loading and short-duration loading. These cause strain hardening in the material. Strain hardening is due to the movement of dislocations and their accumulation within the deformed region. Thus, this dislocation accumulation requires additional stress to be applied to further deform the material.

Smith *et al*. [11] studied the failure and response of square mild steel plates caused by blast loading and reported that rupture strains were between 0.2 and 0.3. This was due to high strain rates that lowered the failure strain. Chichili *et al.* [12] demonstrated that strain hardening was greater at high strain rates from 10^4 s^{-1} to $10^6 s$ than at low strain rates of $10^{-4}s^{-1}$ to $10^{-2}s^{-1}$, but strain hardening increased with strain at low strain rates.

In addition, Johnson *et al*. [13] pointed out that in areas where adiabatic heating occurred, materials in service were prone to have signs of strain localisation, because there was not enough time for heat to be dissipated. Adiabatic heating occurred when the heat generated during the deformation of a material was retained, causing a local increase in the temperature of the material [14]. Bassim *et al*. [15] emphasised that if the concentration of heat were high enough it would affect the dual phase 430 and leave microstructural features, such as high strain concentrations or recrystallised grains, and existed as narrow bands, known as adiabatic shear bands.

2.1.4 Dynamic loading

Zukas *et al.* [16] pointed out that there were some engineering designs and applications that required a deep understanding of the mechanical response of materials to dynamic loading conditions. They defined dynamic loading as the subjection of a material to changing conditions, e.g., high temperatures and/or high strains, for very short time periods. According to Clifton [17], elevated temperatures arose naturally in high-rate deformations through the heating associated with plastic working and the insufficient time for heat dissipation. In other applications, such as high-speed machining, the elevated temperatures arose because of global heating of the region of interest, as well as the localised heating associated with shear bands.

In another study by Zhao and Gary [18], adiabatic heating and microstructural changes were said to be due to high loading rates during dynamic loading. When the loading rate was high, the material response was generally different from what it was at a lower loading rate. Such rate dependence could be observed for nearly all materials. Dynamic loading usually happened at high strain rates. There were important applications for the material behaviour at strain rates between 10 and 500 s^{-1}, such as automotive crashes and collisions. According to the US National Research Council [19], it was imperative to understand the nature of the dynamic load by investigating the source of the load, the duration and impulses. Figure 2.2 describes the different types of loading sources with typical peak pressures, load durations and impulses from each source.

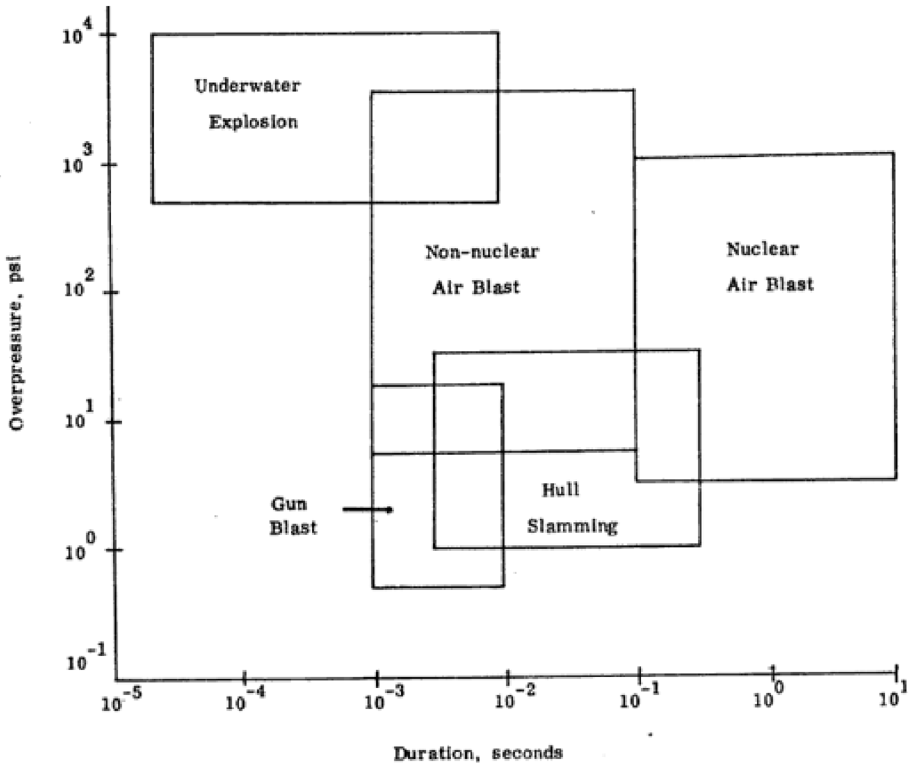

Figure 2.2: Overpressure vs duration of various sources [19].

Lack of experimental tools within these deformation ranges has resulted in the existence of few data on intermediate strain rates (10^{0} to 10^{2} s^{-1}). Harris *et al.* [20] stated that strain rates in drop weight tests and charpy tests were reported to be within these intermediate rates, but these test methods did not provide complete stress-strain curves as a function of strain rates. Clamroth *et al.* [21] stated that dynamic testing conditions were typically not designed to obtain stress-strain responses for materials. Therefore, it was necessary to develop reliable dynamic experimental techniques for materials.

Gerke *et al.* [22] stated that a good technique to test material behaviour at intermediate strain rates 10^{2} s^{-1} was to use a drop-weight tester. During the experiment, a weight, equipped with a striker and guided by rails, was dropped from a certain height and impacted the reviewed component or specimen. Two types of testing devices were distinguished: massive drop towers with a height up to 20 m and drop weights up to 200 kg, and smaller drop darts with a height up to 5 m and drop weights up to 10 kg. The main purpose of drop towers was for component testing, whereas drop darts could be used for tests for the characterisation of a material’s properties.

Drop testers were normally used to test two-dimensional specimens, i.e. plates or dog bone specimens, but beams were also tested by Harsoor and Ramachandra [23] and Liu and Jones [24]. Harsoor and Ramachandra [23] further demonstrated that the load conditions of drop mass experiments were more complex because of combined tension and bending and the results, although extensive, were defective.

The Kolsky bar technique of dynamic loading uses a striker, an incident bar and a transmission bar. The incident bar generates an elastic wave in the incident bar, called the incident wave, which travels through the specimen. However, there is a mismatch of mechanical impedances between the bar and the specimen. Part of the incident wave is reflected back into the incident bar as a reflected wave and the rest of the incident wave is transmitted through the specimen into the transmission bar as a transmitted wave (*see* Figure 2.3).

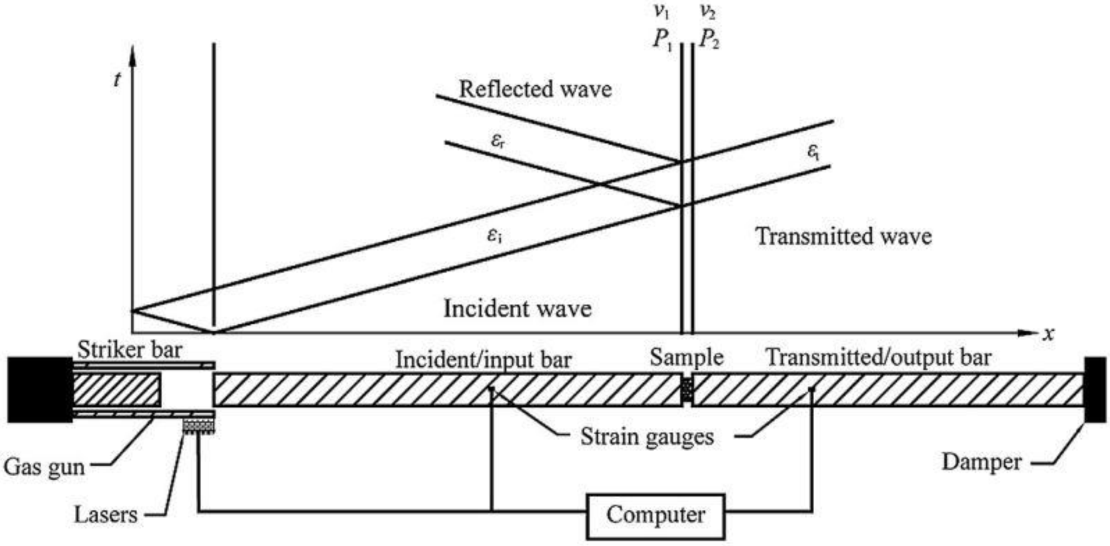

Figure 2.3: Schematic of the Kolksy bar system [25].

Additionally, the Kolksy bar has commonly been used to investigate material response at these intermediate strain rates of 10^0 to 10^2 s^{-1}. However, according to Xia and Yao [25], the challenges included producing consistently low striking velocities, as well as the fact that long bars carried low amplitudes at long duration times. This long duration led to overlapping of the incident and reflected pulses, which were recorded by strain gauges on the incident bar.

Zhang *et al*. [26] studied the dynamic mechanical properties of stainless steel at high strain rates. A dynamic increase factor (DIF) was defined as the ratio of dynamic strength or yield stress to the *quasi*-static strength or yield stress of materials versus the common logarithm of the strain rates that could be obtained. The dynamic response of stainless steel samples was investigated by carrying out compression tests on 5 mm × 5 mm cylindrical samples. These dynamic tests at five different strain rates of 1100 s^{-1}, 2400 s^{-1}, 4000 s^{-1}, 8000 s^{-1} and 16000 s^{-1} were conducted. Concurrently, dynamic Kolsky compression tests were included among these tests at strain rates of 1100 s^{-1} and 2400 s^{-1} and these were on a 12.7 mm Kolsky set-up with 5 mm × 5 mm cylindrical samples. In addition, 2 mm × 2 mm cylindrical samples were used for strain rates of 4000 s $^{-1}$ and 8000 s $^{-1}$, and 2 mm × 1 mm cylindrical samples were employed for the strain rate of 16000 s $^{-1}$. These were tested on a 5 mm miniature Kolsky bar set-up. Based on the above experiments, the relationship between DIF and the logarithmic of the strain rates was obtained, as is shown in Figure 2.3.

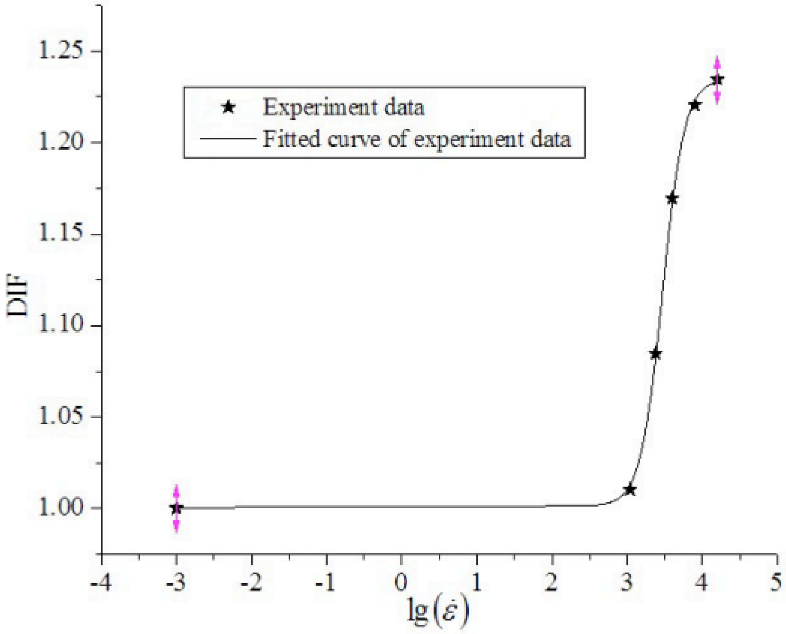

Figure 2.3: Dynamic Impulse Factor (DIF) vs logarithm of strain rates [27].

Shui-Sheng *et al.* [27] stated that the relationship between DIF and the logarithmic of strain rates exhibited three distinct regimes. The strain rate sensitivity was weak in the strain rate range of 0.001 s^{-1} to 1100 s^{-1}. In the strain rate range of 1100 s^{-1} to 8000 s^{-1}, the strain rate sensitivity strengthened, as was shown by the rapid increase in the gradient of the curve (*See* Figure 2.3.) With the increase of the strain rate from 8000 s^{-1} to 16000 s^{-1}, the DIF increased slowly and tended to approach a saturation zone. From this study, it was observed that the DIF played a critical role in the determination of material sensitivity to high strain rates in the dynamic condition.

Another technique to investigate dynamic loading is the use of the ballistic pendulum. According to Rojansky and Bleakney [28], the ballistic pendulum provided a technique for the behaviour of projectiles in air and for armour plates where a projectile was fired.

2.1.5 Repeated Impulsive loading

Impulsive loading implies that the blast duration is short in relation to the response time of the material. An impulsive load consists of a single principal impulse, as illustrated in Figure 2.4. Repeated impact tests against unidirectional, *quasi*-isotropic (cross-ply) and non-symmetric laminates (the target thickness was approximately 4 mm) were reported by De Morais *et al.* [29]. An instrumented drop-weight tester was utilised to obtain load-deflection curves that were used for the evaluation of the current stiffness. Deterioration of the stiffness and an increase of the contact indentor-target duration were noticed as the number of impacts increased.

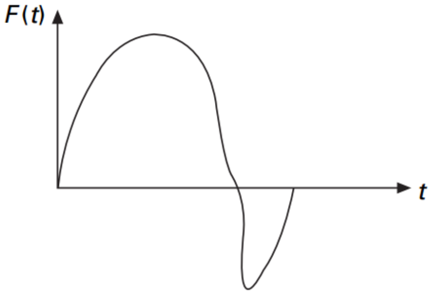

Figure 2.4: A typical impulsive loading curve [28], [30].

Ramulu *et al.* [31] stated that repeated impulsive loading caused progressive accumulation of damage in structures, which might lead to the achievement of a residual stress state in structures. This applied to structures with resultant deformations and failures on the structural surface of the studied material. In a series of experiments, Ranwaha *et al*. [32] investigated the damage and deterioration of steel structures that had been exposed to repeated impulsive loading, which resulted in far more extensive damage than a single blast load would have caused. In subsequent studies, Henchie *et al.* [33] found that repeated load-induced damage increased linearly, proportionate to the number of loads.

However, it was concluded that repeated impulsive loading had an insignificant effect on the resultant impulse of the plate specimens, with little variation evident from a single load up to five loads. Owing to increased loads, the plate response would be different from that caused by exposure to a single blast. Therefore, according to Jacob *et al*. [34], before an investigation into the response of structures to impulsive loads, one would need to understand the initial parameters involved during the impulsive load, such as the charge mass, the number of blast loads and the boundary conditions. Ranwaha *et al.*, Henchie *et al.* and Jacob *et al.* ([32], [33] and [34]) agreed that structural response would widely differ for repeated impulsive blast loads by an increase in the potential frequency of blast damage in the plate specimen surface, depending on the parameters of the blast loading event.

2.2 Principal mechanical properties

Characteristics of materials that describe their behaviour under external loads are known as mechanical properties. It is important to understand material response for mechanical design and damage mitigation. Strength, hardness and toughness are considered as related. However, individually these are very important mechanical properties when material behaviour under external loads is being investigated.

2.2.1 Strength

The strength of a material can be divided into two parts: the yield strength and the ultimate tensile strength. According to Callister and Rethwisch [35], the yield strength was the stress needed to plastically deform a material. Prior to the yield point, the material would deform elastically and would return to its original shape when the applied stress was removed. The optimum strength at which a material could stretch before reaching the point of failure was known as the tensile strength. The tensile strength was useful for the purposes of specifications and for the quality control of a product.

2.2.2 Toughness

According to Ashby *et al.* [36], the ability of a metal to deform plastically and to absorb energy in the process before fracture was termed toughness. To understand the concept of toughness it was critical to understand the definition of ductility. Ductility was a measure of how much a material deformed plastically before fracture, but just because a material was ductile did not make it tough. The key to toughness was a good combination of strength and ductility. A material with a high strength and a high ductility was bound to have more toughness than a material with a low strength and a high ductility. A way to measure toughness was by calculating the area under the stress-strain curve from a tensile test. This value was simply called “material toughness” and it had units of energy per volume. Material toughness equated to a slow absorption of energy by the material.

2.2.3 Hardness

Callister and Rethwisch [35] described hardness as the resistance to permanent deformation. There was a direct relationship between the hardness and the tensile strength of a metal. According to Chandler [37], both these material properties measured the resistance of a material to plastic flow. Peng *et al*. [38] defined hardness as the ratio that depended on the applied test load. This meant that the hardness was the ratio between the size of the indentation and its depth. Again, according to Chandler [37], hardness could be differentiated into macro-hardness, micro-hardness and nano-hardness, depending on the nature of the forces applied. Macro-hardness was a measurement of the hardness of a material when a large force had been applied and was applicable to a large area with a deep indentation. Macro-hardness could be measured using three methods, namely:

- The Vickers Hardness Test, which used a diamond pyramid indenter
- The Brinell Hardness Test, which used a ball-shaped indenter

- The Rockwell Hardness Test, which used a ball-shaped indenter with a load applied repeatedly.

In contrast, micro- and nano-hardness tests measured hardness at very small loads. Micro-hardness testing indicated that the applied load on the indenter was less than 1 kg. Micro-hardness was evaluated by measuring the area of the indentation, rather than the depth. Gong *et al*., [39] emphasised that, when a low load was used, the measured hardness was usually high. However, an increase in test loads decreased the measured hardness. This phenomenon was referred to as the Indentation Size Effect (ISE).

2.3 Adiabatic shear bands

Bassim and Odeshi [40] noted that adiabatic shear bands (ASBs) appeared as a result of strain localisation. Strain localisation occurred as a result of mechanical instability, caused by a local rise in temperature at high strain rate deformations. Shear bands were hard and brittle and made the material prone to crack initiation and propagation. The deformation that became localised as adiabatic shear bands was accompanied by an immediate decrease in the metal’s ability to carry stress.

Adiabatic shear bands were not only caused by adiabatic heating, but also by the deformation process, which caused strain to be concentrated in one area. Odeshi *et al.* [14] pointed out that there were different forms and types of adiabatic shear bands, depending on the intensity of the deformation and the type of material. Boakye-Yiadom and Bassim [41] and Xu *et al.* [42] referred to the two types of adiabatic shear bands reported in literature as:

- Transformed shear bands
- Deformed adiabatic shear bands.

Timothy [43] described deformed adiabatic shear bands as zones of intense deformation, which appeared as severely distorted regions that showed extensive shear deformation**.** These bands usually appeared where the material had undergone a permanent change in the microstructure. This type of shear banding was common in non-ferrous metals, such as copper and aluminum, and it consisted of elongated grains that were distorted and uneven in size. Transformed shear banding was usually observed as white, long lines of extreme strain under light microscopy. Boakye-Yiadom and Bassim [41] further noted that adiabatic shear bands were known to consist of fine equiaxed sub-grains with high dislocation density. This type of shear banding was usual in metals such as steel and hardened steel.

Xu *et al.* [42] stated that shear band formation was an important deformation feature that occurred during high temperature and high strain loadings. Pouget and Reynolds [44] added that extreme strain and high temperature caused the nucleation of a dispersion of fine, equiaxed grains in an area of a microstructure. This was known as dynamic recrystallisation.

According to Murr *et al*. [45], when the temperature was too high, the grain structure that had formed during the dynamic recrystallisation process could not be clearly observed. The structural changes that occurred during adiabatic heating involved changes in the grain morphology, i.e., in size and shape. The grains were usually smaller, characterising the white ASB zone as shown in figure 2.5, or the grain size mixtures could be evidenced by the darker thin bands within the adiabatic shear band zone. Furthermore, other studies by Xue *et al*. [46] and Perez-Prado *et al*. [47] stated that the mechanisms for recrystallisation changed under different high strain rates and temperatures. In response, multiple theories on nucleation mechanisms during recrystallisation were researched and proposed. Recent research has included several theories for shear band development, the process zone theory and the analysis of steady shear band propagation.

Figure 2.5 displays the microstructural evolution of shear localised deformation, obtained at multiple corresponding loading durations. The micrographs show *post-mortem* observations of shear deformation at different sections, loaded at a variety of velocities and times. The time of exposure to stress was five minutes as indicated in figure 2.5. Figure 2.6 displays a schematic that shows the development of shear bands in a metal. In addition, it displays the formation of shear bands by grain structure re-organisation and dislocation density increase. Dislocation density increase is the development of these adiabatic shear bands by the different loading durations in 316L stainless steel.

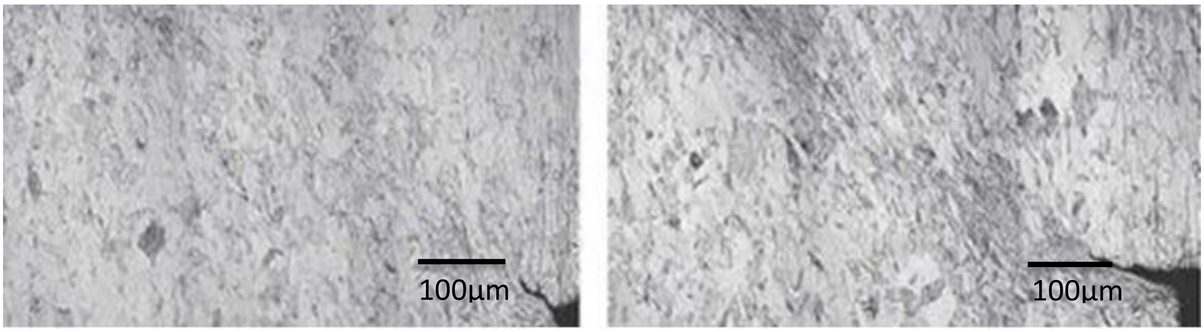

a) t 5, 25.1ms

b) t 5, 31.0ms

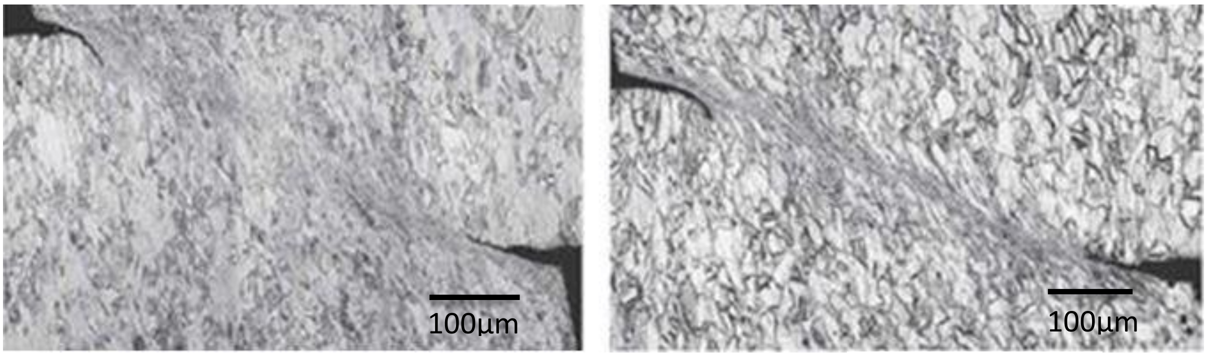

c) t 5, 36.1ms

d) t 5, 41.2ms

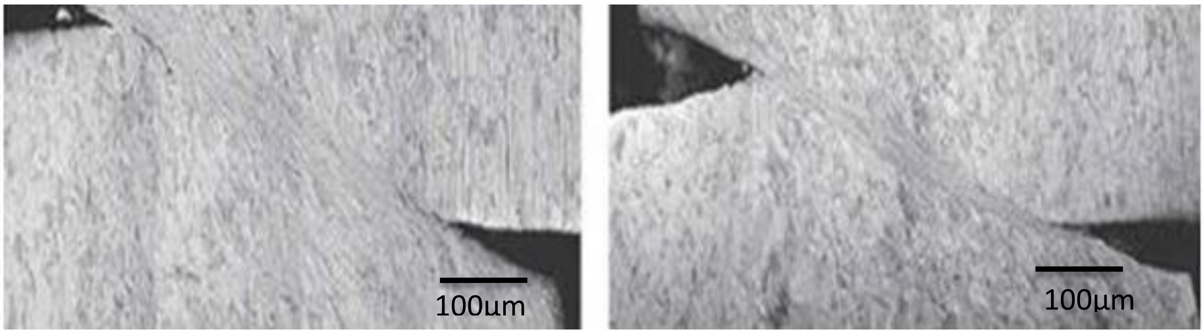

e) t 5, 51.5ms

f) t 5, 61.8ms

Figure 2.5 : Microstructural evolution of shear localised deformation, obtained at the corresponding loading durations, displaying *post-mortem* observation of shear deformation at shear sections loaded[46].

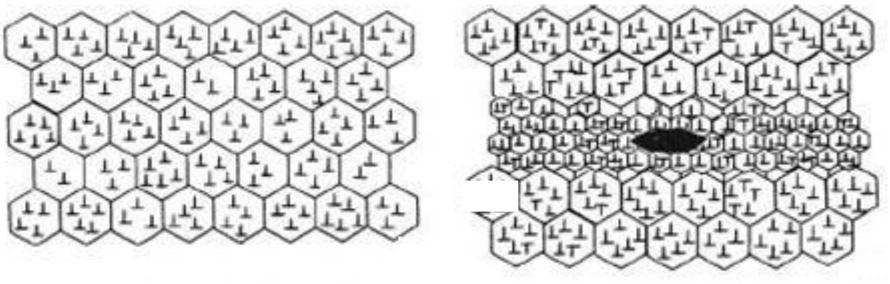

a) Deformed, equiaxed grains (dislocations denoted as ⊥)

d) Shear localisation, creating dense dislocation

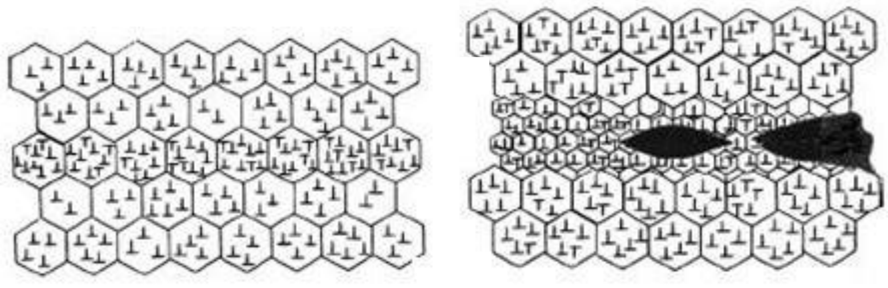

b) Dynamic recrystallisation in dense dislocation zone.

e) Deformation of recrystallised grains in ASB

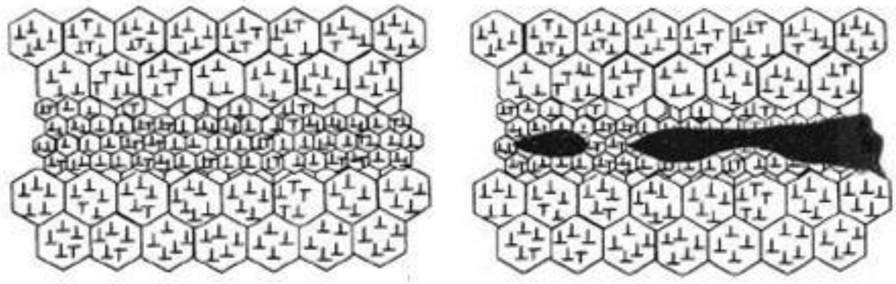

c) Crack growth and propagation in ASB

f) Crack coalescence and propagation in ASB

Figure 2.6: Microstructural evolution of Adiabatic Shear Bands (ASBs)[46].

2.4 Grain structure

The mechanical properties depend on the microstructure of a material. The microstructural features, such as grain size, orientation, morphology etc., can be used to characterise a material and property relationship. When a metal deforms owing to stress application, the grains in a polycrystalline metal change their morphology (size, orientation and shape). According to Humphrey *et al*. [48}, the deformation on a micro-scale corresponded with the macroscopic shape change of the material. This microstructural evolution caused a corresponding change in the local and/or global mechanical properties. This microstructural evolution led to a corresponding change in the local and global mechanical properties.

2.4.1 Grain orientation

Russell and Lee [49] demonstrated that the grain orientation changed during deformation and the changes did not take place randomly. These changes were a consequence of the deformation that occurred on the most favourably-oriented slip planes or twinning systems and it followed that the deformed metal acquired a preferred orientation. Instead, according to Rollett *et al.* [50]*,* the grain orientation changed and the new deformation microstructure consisted of a new boundary grain area (longer flat grains), owing to dislocation creation and motion. The energy resulting from an increase in grain area represented a part of the stored energy from plastically-deforming the metal.

2.4.2 Grain and sub-grain size

Hansen *et al*. [51] observed that the deformation microstructure included an appearance of an internal structure within the grains. This might take several forms, but all of these forms involved grain boundaries. Moreover, Dillamore *et al.* [52] found that high angle boundaries (HAGBs) were typically associated with grains and recrystallisation, while low angle boundaries (LAGBs) were associated with sub-structures that formed within parent grains, often associated with recovery and dislocation re-arrangement.

2.4.3 Hall-Petch equation for grain size

Chao and Varma [53] used the Hall-Petch equation to explore the relationship between grain size and yield strength. Understanding the effect of strain rate on the grain size and mechanical properties in metals and alloys was shown to be necessary for proper mechanical design. Grain size strengthening was explained in detail by Wilsdorf and Kuhlmann-Wilsdorf [54] in terms of mesh length theory, which states that work-hardening is caused by the piling up and multiplication of dislocations in a metal.

The Hall-Petch equation for the determination of grain strength (σ_y) is defined by Eq. 2.1

$$\sigma_y = \sigma_i + k_y d^{-\frac{1}{2}} \qquad \text{Eq. 2.1}$$

where k_y is the Petch parameter, otherwise known as an unspinning constant, σ_i is a material constant for the stress required to overcome lattice friction and cause dislocation movement and d is the grain size diameter.

According to Kumar [117] k_y can also be defined as:

$$k_y = \sigma_o r^{-1/2} \qquad \text{Eq. 2.2}$$

where r is the distance of the source of the dislocation movement from the head of the dislocation pile up.

With an increase in grain size refinement, there will be a situation where the source of the dislocations cannot generate dislocations at a lower stress than the theoretical shear strength. This means that the maximum shear strength of the material is achieved and the material is closer to the point of failure. In this case, the flow stress dependence can be described in accordance with Eq. 2.3. According to Arzt [118], the Hall-Petch equation only breaks down when the sample reaches maximum failure, i.e., the plate is torn and the microstructural grain changes have occurred. A larger sample size develops plane strain conditions and limits ductility.

$$\sigma_3(d) = (1 - (\frac{d-t}{d})^2\sigma_B + (\frac{d-t}{d})^2\sigma_V \quad \text{Eq. 2.3}$$

where σ_B is the strength of the grain boundary and σ_V is the strength of the nano-grain volume.

From Equation 2.1, Firstov *et al.* [55 and 56] concluded that a decrease in yield strength had been observed, with a reduction in grain size, a critical grain size having been reached. The critical grain sizes for air-cooled 430 stainless steel, which were studied by Matthews *et al.* [99], had an average grain size of 10,9µm. In addition, Firstov *et al.* [55] demonstrated that, for smaller sizes, Eq. 2.4 was more suitable:

$$\sigma_1 = \sigma_o + k_1 d^{-1} \qquad \text{Eq. 2.4}$$

where σ_o, the average resistance to dislocation, was motion and k_1 described the difficulty in slip motion through grain boundaries.

Masumura *et al.* [57] further observed that the formulation of the Hall–Petch relationship expressed the dependency of the lower yield point or the fracture stress of iron on the grain size.

2.5 Material deformation

2.5.1 Mechanical response to deformation

Gere and Goodno [4] reported that the mechanical response of a material exposed to an external load (stress) was either by plastic or elastic deformation. According to Callister and Rothwisch [35], an elastic response was such that the material strain was not enough to cause a permanent inelastic deformation, which meant that the material could return to its original geometry. This was further verified by Cain [58] and Dowling [59]. Askeland and Phulé [60], Callister and Rothwisch [35] and Gere and Goodno [4]. All defined plastic deformation as a permanent change in the material’s geometry after the removal of the stress, owing to yield stress having being reached.

2.5.2 Material defects

Ashby *et al*. [36] demonstrated that there were a number of defects that were inherent in the microstructure of a polycrystalline metallic material, namely, point defects, line defects and surface defects, as illustrated in Figure 2.7(a) and (b).

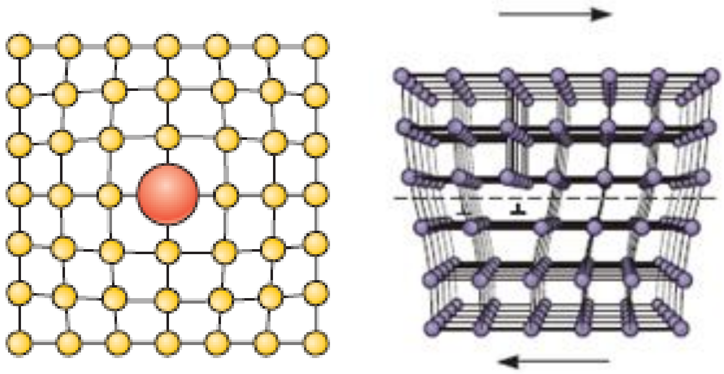

a) Large substitutional atom in a crystal lattice

b) Edge dislocation in a crystal lattice

Figure 2.7:Material defects in a crystal lattice[60]

According to Askeland and Phulé [60], a point defect was caused by a localised disruption in the crystal lattice, leading to the replacement of an atom by a different type of atom. This was referred to as a substitutional defect. On the other hand, a line defect was known as an edge dislocation, where the crystal lattice was disrupted by the introduction of an extra plane of atoms. Callister and Rethwisch [35] described the third type of defect as a surface defect. This would be found on the surface of the material, in the form of a crack or a tear.

Callister and Rethwisch [35] further stated that dislocations were areas where the atoms were out of position in the crystal structure. Dislocations were generated and moved by an application of stress. Under an applied stress, dislocations moved and multiplied. The increase in the dislocation density of the material caused a greater resistance to plastic deformation, thus each strain increment strengthened and hardened the material.

According to Anderson [61], beyond the Ultimate Tensile Strength (UTS) of the material, during tensile testing the cross sectional area continued to decrease until uniform deformation turned into localised deformation. This phenomenon was given the term *necking*. During necking, the material's ability to carry stress decreased because of the reduction in the cross-sectional area. In addition, as the instability of the material increased, the plastic deformation was localised at one point, causing the necking to increase until the point of fracture. Anderson further stated that necking usually occurred as a result of defects that were caused by stress or as a result of pre-existing defects.

2.5.4 Comparison between ductile vs brittle fracture

Anderson [61] further demonstrated that in metallic materials there were two modes of fracture, ductile and brittle. Ductile metallic materials exhibited appreciable plastic deformation after failure, in the form of a macroscopic cup-cone shape, while brittle metallic materials showed little plastic deformation after failure and a flat fracture surface resulted. Hall [62] illustrated this point in Figure 2.7, which displayed two different ways in which materials could fracture. In Figure 2.7 (a), the first image shows a cup-cone ductile fracture, the result of extensive plastic deformation ahead of a crack. The second image shows a brittle fracture surface, which is rough. This roughness is due to the small amount of plastic deformation ahead of the crack. Figure 2.7 (b) is a schematic diagram of the modes of fracture for different types of materials, where the softer the material, the more ductile it would be. However, brittle fractures would occur in cold metals and ceramics.

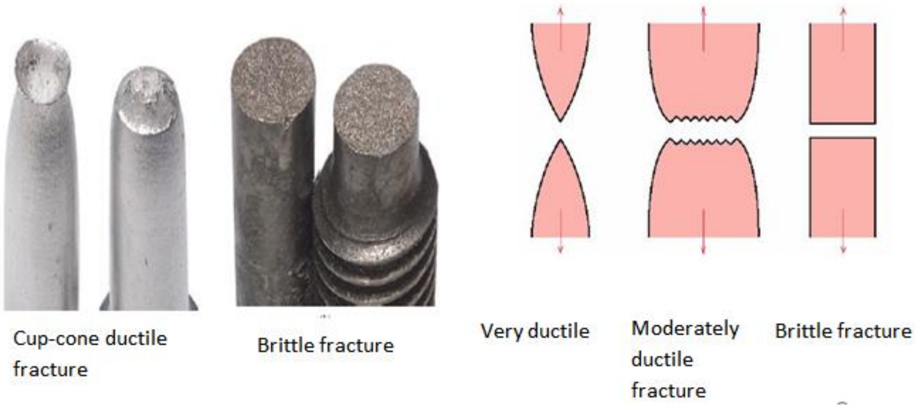

a) Cup-cone ductile fracture and brittle fracture surfaces

b) Modes of fracture

Figure 2.8: Ductile and Brittle Fractures [62].

Hall [62] reported that a crack initiated in a material and the way it propagated in the material could show the mode of fracture it would undertake. For a ductile fracture, the crack would move slowly, with a large amount of plastic deformation. On the other hand, as described by Smith [11], for a brittle fracture, cracks would spread quickly, with little or no plastic deformation. Cain [58] pointed out that a material’s response to stress application differed, depending on the type of stress that was applied.

Shin *et al*. [63] stated that ferritic stainless steel (FSS) sheets, containing 11 – 17% Cr, had been found to develop an undesirable surface corrugation, known as ridging, when pulled or deep drawn. When pulled or deep drawn, FSS showed undulations, with peaks on one side of the sheet coinciding with valleys on the other side, but without change in the thickness. According to Shin *et al*. [63], **t**he ridges had a depth in the range of 20 – 50 µm. Lee [64] further noted that ridging was distinguished from stretcher strain, in that the latter occurred within the range of about 5% elongation, whereas the former became noticeable at a stage of about 5% elongation but, on further straining, the amplitude increased until the point of failure of the specimen.

2.6 Blast loading

2.6.1 Types of explosives

Kinney and Graham [65] defined an explosive material as a chemical substance that released substantial amounts of potential energy upon exposure to heat by detonation. During this process, the explosive material underwent a physical change, in shape and state. Explosive materials were classified into two categories according to their rates of decomposition. These were listed by Davis *et al*. [66] as high and low explosives and were further classified as primary and secondary explosives, depending upon their sensitivity to ignition. Primary explosives differed from secondary explosives because they were used to detonate high explosives, examples being nitroglycerin and mercury fulminate. Furthermore, primary explosives were known to be highly sensitive to ignition. Primary explosives could be initiated by impact, light, heat and changes in pressure. As opposed to primary explosives, secondary explosives required a detonating substance as a supplementary explosion initiator, e.g., lead azide. Secondary explosives had a higher stability under controlled room conditions. However, they required much energy for detonation because of the highly-strained carbon-carbon bonds that existed within their molecular structures. The most common examples of secondary explosives were Research Department Formula X (RDX) and Trinitrotoluene (TNT).

2.6.2 Detonation

Baker [67] stated that during an explosion there was a release of gas that was caused by the combustion of the solid explosive material. During the explosion there was a discharge of high temperature and heat, causing variations in nearby air pressures. Blast wave pressures could rapidly increase to pressures higher than the standard atmospheric pressure. However, after some time the pressure decreased to pressures below the ambient pressure. Ngo *et al*. [68] stated that this effect was known as side-on overpressure, which gradually decreased by decay over time, while the blast wave expanded outwards from the source of the explosion.

The Federal Emergency Management Agency [69] researched the effects of the detonation of explosives and concluded that, during an explosion, the high pressures produced decay and the effect was characterised by a pressure pulse, as represented in Figure 2.8. Two regions in this pulse are evident, namely a positive region and a negative region. The overpressure is depicted by a large peak, where there is a gradual decrease in the wave, which is immediately followed by a negative pressure. After some time, the pressure behind the wave front drops below the overpressure, as indicated in Figure 2.9.

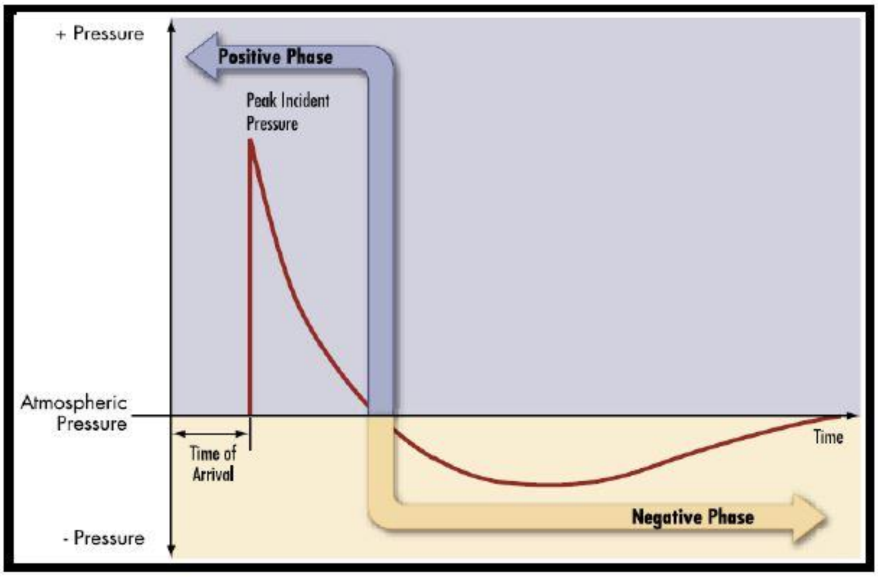

Figure 2.9: Pressure vs time for blast wave propagation [69].

The overpressure phase increases rapidly with the explosive yield energy and with the distance away from where the explosion is taking place. Rajendran *et al*. [70] showed that the pressure vs time blast wave propagation could be represented by the Friedlander equation, given as Eq. 2.5.

$$p(t) = Po + Pm[1 - \left(\frac{t}{t_d}\right) e^{-\alpha t/t_d} \qquad \text{Eq. 2.5}$$

where P_o was the ambient pressure, t was the instantaneous time, t_d was the positive duration of the pressure pulse and α was the waveform parameter, which depended upon the peak overpressure, Pm, of the shock wave.

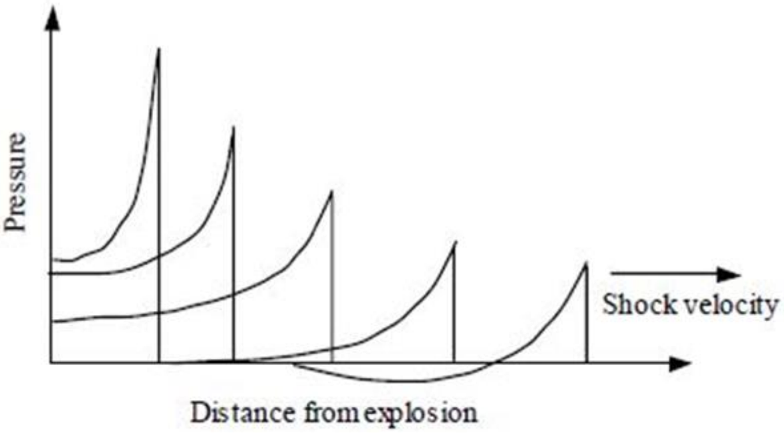

Figure 2.10: Schematic depicting blast wave propagation during an explosion [68].

In addition, Ngo *et al.* [68] described how the blast wave velocity also decreased over time and the pressure decreased as the wave moved distances away from the explosion source, as indicated in Figure 2.10. The parameters most important when dealing with explosive decay were the pressure, the shock velocity, the impulse and the distance from the explosive source. As the wave propagated it decreased in speed and strength.

Lewis and Von Elbe [72] described an explosion as a chemical reaction where molecules of gas were in rapid motion and collided frequently with one another. The chance of collision between molecules was largely dependent on temperature, according to the Arrhenius equation, given as Eq. 2.6.

$$A = e^{\frac{-E}{RT}} \qquad \text{Eq. 2.6}$$

Once the explosion was initiated it would be classified as a nuclear, vapour or chemical explosion, depending on its nature. According to Glass [73], an explosion happened as a result of varying conditions of pressure *p,* with the radius *r*, usually from the shock wave to the boundary of the driving expanding gas. This gas was chemically discharged by the explosive as the shock wave pressure decayed from an increase in distance from the explosion core.

2.6.3 Explosion effects

Sachdev [74] stated that, during the explosion process, the explosive materials, either in solid or liquid form, converted into gas. These gases expanded outwards and generated shock waves in the adjacent air, known as blast waves. A blast wave was a shock wave that expanded at a supersonic speed, outward, from the core of the explosion. Explosive pressures decayed extremely rapidly with distance from the source. Direct air blasts tended to cause more localised damage. According to the Federal Emergency Management Agency (USA) [69], the duration of an explosion event was very short and was measured in milliseconds. Therefore, the mass of the structure had a strong mitigating effect on the response, because it took time to mobilise the mass of the structure. According to Spranghers *et al*. [75], when the shock impulse acted, all material particles were forced to move out-of-plane and were provided with initial velocities. Additionally, when the shock wave had vanished, the plate deformation was driven only by the imparted momentum.

A blast load was considered impulsive, owing to the nature of the interaction of the blast wave and the target structure, where the energy of the load that caused the target structure to deform was transferred to the structure in an extremely short period of time. According to Henchie *et al*. [33], the entire effective load from the blast was transferred to the target before it responded, owing to the mass inertia. The differences in the uniform and localised loading conditions would result in different structural responses.

2.7 Response of single plates to blast loading

Wiehahn *et al*. [76] and Neuberger *et al.* [77] reported that the response of structures to blast loads was in the form of plastic deformation, owing to high strain rates and high temperatures. According to Rudraputna *et al.* [78] and Nurick and Martin [79], the macroscopic response of structures to blast loading included large inelastic deformation failures and tearing failures of the structure and these were dependent on the loading conditions. It was further reported by

Nurick *et al*. [79] that there were two different loading techniques, uniform loading and localised loading.

2.7.1 Response of circular thin plates to uniform loading

The macroscopic response of plates to uniform loading was researched by Teeling-Smith and Nurick [81]. The uniformly blast loaded plate specimens had evidence of thinning at the boundary. The thinning was due to a permanent midpoint deflection, which increased with impulse as the plates were repetitively loaded.

The literature revealed that uniform loading of a plate under study could be achieved, using three different methods:

- Detonating an explosive charge mass at a great stand-off distance (Jacob *et al.* [34]).
- Loading the target plates with the use of a shock tube (Kleinschmit [82]).
- Using concentric annuli of explosive charge in close proximity to the plate under study (Yuen [83]).

According to Teeling-Smith and Nurick [81], repeatedly loading a plate in uniform loading increased the midpoint deflection, owing to an increasing impulse. The midpoint deflection increase depended on the charge mass and the number of blasts. However, as the impulse was increased beyond the point of complete tearing, the midpoint deflection decreased. Kadid [71] pointed out that the failure tended towards complete shear at the boundary edges. This sort of behaviour is shown schematically in Figure 2.11. In addition, a similar behaviour was observed by Nurick *et al*., [84] and Nurick and Martin [85].

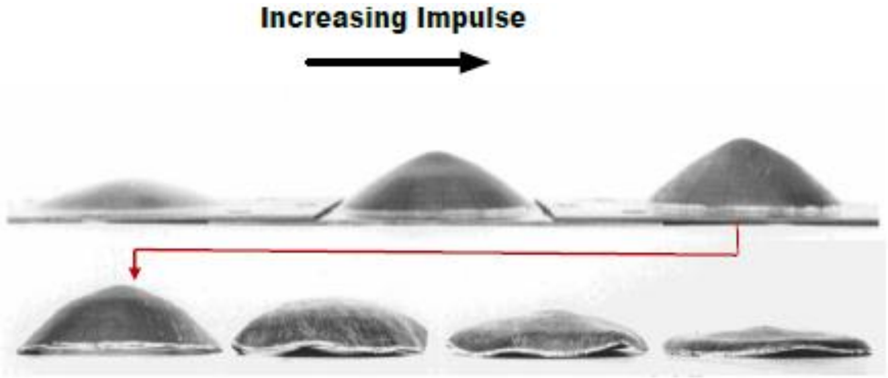

Figure 2.11: Photographs of uniformly loaded circular plates, showing change in midpoint deflection for increasing impulse [81]

Nurick and Martin [79] used mild steel that had been subjected to uniform blast loads and the results displayed a variety of failure modes, as is depicted in Figure 2.12 below.

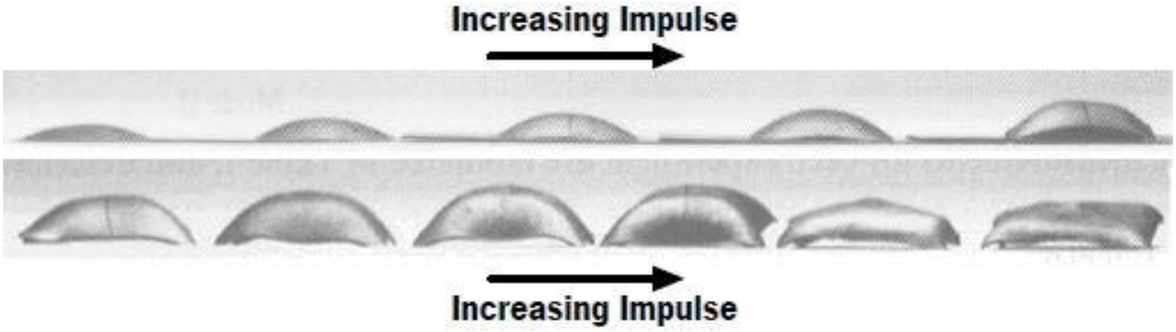

Figure 2.12: Photographs of test specimens by displaying failure modes of uniformly blasted plates.[79].

2.7.2 Response of circular thin plates to localised blast loading

The localised loading condition had a shorter stand-off distance in comparison to the uniform condition. The impact process occurred over a wider area of the plate and at a longer distance for the uniform condition. This was the conclusion of Wierzbicki *et al*. [86], who studied the response of thin circular plates subjected to localised blast loads. Their research created an opportunity to understand where the tearing was most likely to be on plates subjected to these loading conditions.

The failure modes were similar to those of repeated uniform blast loading, with the exception of having a capping failure mode in localised blast loading, as noted by Gharababaei and Darvizeh [87]. According to Nurick *et al*. [85], the capping failure mode was further subdivided into three sub-modes, namely:

- Mode Itc: Large inelastic deformation with thinning in the central area of the plate.
- Mode II*c: Partial tearing in the central area of the plate.
- Mode IIc: Complete tearing in the central area of the plate and removal of the cap.

For the Mode Itc, the large inelastic deformation had a larger dome-shaped area in the plate than the dome-shaped pulse of the uniformly-loaded plate. In addition, in this loading condition the load diameter was proportional to the cap diameter. Thinning of the plates occurred and the failure modes of these plates depended on the charge mass, the plate thickness and the number of blasts. Nurick and Radford [88] identified a variety of models that had been developed to demonstrate the response of circular plates to blast loads**.** Wen *et al*. [89] contributed further by developing a *quasi*-static procedure to predict the deformation and failure of clamped circular plates under impulsive loading. More recently, Gharababaei *et al*.[87] have studied the deformation of circular plates exposed to blast loading by performing experimental blast tests on a variety of materials to investigate the response of thin circular plates to localised blast loading.

2.8 Failure modes of thin plates subjected to blast loads

The failure modes of beams subjected to uniform loading during blast tests were first classified by Menkes and Opat [90]. These were classified as three types of failure modes:

- Large inelastic deformation of the entire beam (**Mode I**)
- Tensile tearing at the supports (**Mode II**)

- Transverse shear failure of the beam at the supports (**Mode III**)

These are shown in Figure 2.13 below.

Nurick and Shave *et al*. [91] defined similar modes of failure for fully-clamped circular and quadrangular plates. However, Nurick [88] further subdivided Mode II into three more failure modes, namely:

- Mode II* - Partial tearing
- Mode IIa - Complete tearing with increasing mid-point deformation
- Mode Iib - Complete tearing with decreasing mid-point deformation

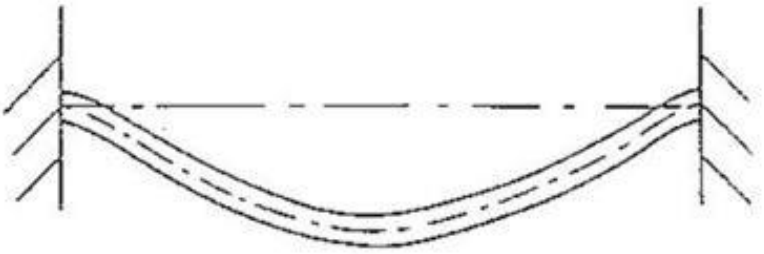

a) Mode I: Large inelastic deformation

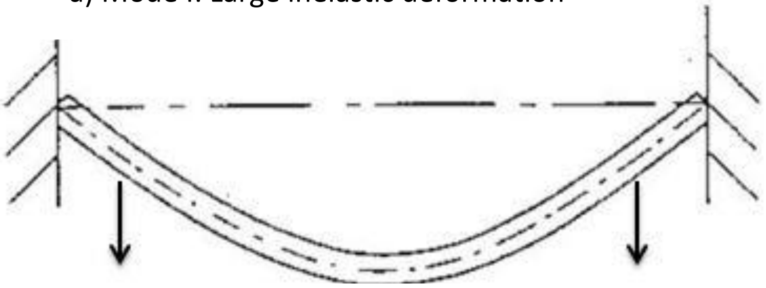

b) Mode II: Complete tearing at the boundary with an increasing mid-point deflection

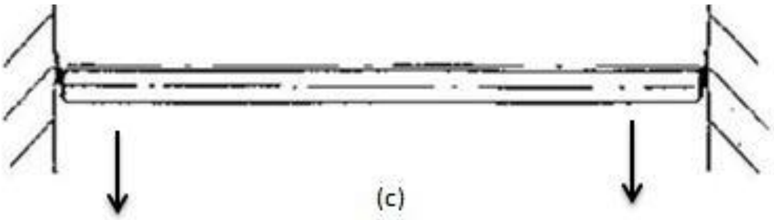

c) Mode III: Complete tearing at the boundary with minimum deflection (shear failure at the supports)

Figure 2.13: Modes of failure for a uniformly blast loaded beams [90]

Further characterisation of the modes of failure was performed for centrally-localised blast loads by Jacob *et al.*, [80] and these are grouped in Table 2.1 below:

Table 2.1: Summary of modes for both uniform and localised loading conditions [80]

Modes of failure	**Description**	**Uniform Loading**	**Localised loading**
Mode I	Large inelastic deformation	✓	✓
Mode Ia	Large inelastic deformation with necking around the boundary	✓	
Mode Ib	Large inelastic deformation with necking around the entire boundary	✓	✓
Mode Itc	Large inelastic deformation with thinning in the central area		✓
Mode II*	Large inelastic deformation with partial tearing around part of the boundary	✓	
Mode II*c	Partial tearing in the central area		✓
Mode II	Tensile tearing at the boundary	✓	✓
Mode IIa	Tearing with an increase in the midpoint deflection with increasing impulse with complete tearing at the boundary	✓	
Mode IIb	Tearing with a decrease in the midpoint deflection with increasing impulse with complete tearing at the boundary	✓	

Mode IIc	Complete tearing in the central area-capping		✓
Mode III	Transverse shear failure at the boundary	✓	
Petalling	Tearing at the centre with “petals” of material folded away from blast location		✓

2.9 Theoretical findings

2.9.1 Damage number for structures subjected to impulsive loading.

Damage numbers for structures subjected to impulsive loadings were formulated by Jones [92] and Nurick and Martin [93] for clamped rigid circular plates, as well as for quadrangular plates. However, this section will focus only on damage numbers for circular fully-clamped plates

2.9.2.1 Jones damage number for circular plates

Jones [92] introduced a damage number to predict the large inelastic deformation experienced by fully-clamped circular plates exposed to uniform impulsive loads. This damage number has been used in multiple studies for bending and membrane response of structures exposed to uniform loading. The damage number is a dimensionless energy number and can be calculated using Eq. 2.7 below.

$$\lambda = \frac{\mu V_O^2 R^2}{M_O H} \qquad \text{Eq. 2.7}$$

where V_0 is the Initial velocity, μ is the Mass per unit area $(\rho H), M_o$ is the moment at which the entire cross section has yielded. The equation for the plastic moment is given by $M_o – \frac{\sigma_y H_2}{4}$, R is the Plate radius and H is the Plate thickness.

Eq. 2.7 is also written in terms of impulse through substitution, where:
Substituting for equations M_0 and μ, λ becomes

$$\lambda = \frac{\mu V_O^2 R^2}{M_O H} = \frac{(\rho H) V_O^2 R^2}{\left(\frac{\sigma_O H^2}{4}\right) H} = \frac{\rho V_O^2 R^2}{\sigma_O H} \qquad \text{Eq. 2.8}$$

Impulse is therefore given as:

$$I = M V_O \qquad \text{Eq. 2.9}$$

where M is the mass of the plate calculated from the density of the plate and the volume.

Therefore if Eq. 2.10 can be re-written as:

$$V_O = \frac{I}{M} = \frac{I}{\pi R^2 H\rho} \qquad \text{Eq. 2.10}$$

substituting Eq. 2.10 into Eq. 2.11, the new equation for the Jones damage number for circular plates can be written as:

$$\lambda = \frac{\rho V_O^2 R^2}{\sigma_O H} = \frac{\rho(\frac{I}{\pi R^2 H\rho})^2 R^2}{\sigma_o H} = \frac{4I^2}{\sigma_o H^4 \pi^2 R^2} \qquad \text{Eq. 2.11}$$

2.9.2.2 Nurick and Martin damage number for circular plates

Nurick and Martin [93] proposed a modified damage number for impacted quadrangular and circular plates, based on the Johnson damage number, as indicated in Eq. 2.12.

$$\alpha = \frac{\rho v^2}{\sigma_d} \qquad \text{Eq. 2.12}$$

where ρ is the density of the material, v is the imparted velocity and σ_d is the damage stress.

The velocity in this damage number equation can be written as:

$$v = \frac{I}{m} \qquad \text{Eq. 2.13}$$

where m is the mass of the plate and I is the imparted impulse.

The mass is obtained from calculating it from the density of the material and the volume of the plate, written as:

$$m = \rho V = \rho A_o H \qquad \text{Eq. 2.14}$$

where ρ is the material density, A is the area of the plate and H is the plate thickness.

Substituting Eq. 2.13 into Eq. 2.14, the velocity of the material can be written as:

$$v = \frac{I}{A_O H \rho} \qquad \text{Eq. 2.15}$$

Substituting Eq. 2.15 into Eq. 2.14, the Johnson's damage number can be written as:

$$\alpha = \frac{\rho v^2}{\sigma_d} = \frac{I^2}{A_O^2 H^2 \rho \sigma_d} \qquad \text{Eq. 2.16}$$

If the Impulse is defined as the impulse per unit area, the new equation is represented by Eq.17:

$$I = I_O A \qquad \text{Eq. 2.17}$$

Therefore, the Johnson's damage number can be written as:

$$\alpha = \frac{I^2}{A_O^2 H^2 \rho \sigma_d} = \frac{(I_O A)^2}{A_O^2 H^2 \rho \sigma_d} = \frac{I_O^2}{H^2 \rho \sigma_d} \qquad \text{Eq. 2.18}$$

Johnson's damage number was effective in quantifying the amount of damage but it did not consider the boundary conditions, the target dimensions and the method of impact. This damage number was then deemed to be inaccurate. Therefore, Nurick and Martin [93] proposed a new damage number (ψ), based on Johnson's damage number, given as:

$$\psi = \frac{I}{AH(\rho \sigma_d)^{0.5}} \qquad \text{Eq. 2.19}$$

where A is the plate area and H is the plate thickness.

There was a relationship between the distance from the centre of the plate to the closest boundary and the plate thickness known as the macroscopic aspect ratio, λ. The importance of this aspect ratio is that it quantifies the amount of damage on the plate, because during impact the aspect ratio changes as a result of the damage to the plate.

Therefore, the macroscopic aspect ratio of circular plates is given by:

$$\lambda = \frac{R}{H} \qquad \text{Eq. 2.20}$$

where R is the plate radius and H is the plate thickness.

In addition, a loading parameter for loaded circular plates was established by Nurick and Martin [93], which took into account the loaded area of the plate with regard to its total area. This loading parameter was given as:

$$\zeta_c = 1 + ln\frac{R}{R_O} \qquad \text{Eq. 2.21}$$

where R was the total area of the plate and R_O was the loaded area. In the case where R_0=R then $\zeta_c = 1$, meaning a plate had been uniformly loaded.

In addition, Nurick and Martin combined Eq. 2.20 with Eq. 2.22 to form a modified damage number for circular plates that considered the boundary conditions, the target dimensions and the method of impact.

For uniformly-loaded circular plates:

$$\psi_c = \frac{I}{\pi RH(\rho\sigma_O)^{0.5}} \qquad \text{Eq. 2.22}$$

For locally-loaded circular plates

$$\psi_c = \frac{I(1+ln\frac{R}{R_O})}{\pi RH(\rho\sigma_O)^{0.5}} \qquad \text{Eq. 2.23}$$

The relationship of the mid-point defection of the uniformly blast loaded plate to the plate's thickness is represented by Eq. 2.24:

$$\frac{\delta}{H} = 0.45\phi_q \qquad \text{Eq. 2.24}$$

CHAPTER 3

3. Experimental details and procedures

The procedure for the repeated blast loading experiments performed on 2 mm thick plates are presented in this chapter. Furthermore, the details and specifications of the blast tests are also discussed.

3.1 Material selection

Extensive experimental blast research has been performed on structures made from Domex and mild steels [94]-[98]. However, these steel types are prone to oxidation and phase changes and do not exhibit good grain growth when heat-treated. Consequently, it is difficult to track changes in the microstructures of these steel types when they were exposed to impulsive loading. Callister [35] emphasised the importance of considering all the properties, advantages and uses of any material before any experimental investigation was made. This was to prevent unfavourable consequences. Previous studies by Matthews *et al.* [99] and Nyongesa *et al.* [100] had clearly highlighted that stainless steel AISI 430 had an advantage because of its good morphological features. Matthews *et al.* [99] further noted that AISI 430 ferritic stainless steel had good grain growth, caused by a higher affinity to quickly recover induced strain energy.

Stainless steel grade AISI 430 was chosen for this research because it had consistent material properties and was not prone to any phase changes when exposed to various loads. Because single phase was obtained through heat treatment, followed by slow cool, to ensure that it was in full ferritic form, the material was assumed not to have any phase changes when exposed to various blast loads. The combination of these properties made it a suitable material for the tracking of changes in its microstructure in order to characterise the effect of blast loading. This investigation was approached by comparing the initial microstructure of the material to its final microstructure, after it had been blast loaded.

The microstructure of AISI 430, in Figure 3.1, shows a fine grain size, with long, flat and heterogeneous grains when observed in the transverse direction plane. The fine grain structure is due to the micro alloying of manganese, phosphorus and nickel. This is indicated in Table 3.1.

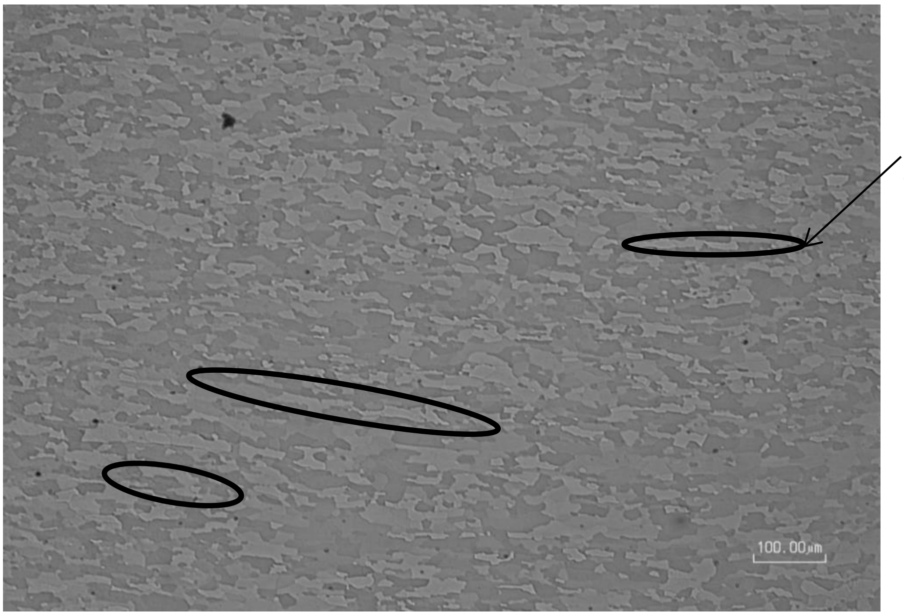

Long, flat
heterogeneous
grains.

Figure 3.1: Microstructure of AISI 430.

Table 3.1: Chemical Composition of AISI 430 steel [procured from *Eurosteel* (Pty)Ltd.].

Elements	**Wt. % age**
Carbon	0.045
Manganese	0.42
Silicon	0.44
Phosphorus	0.02
Sulphur	0.001
Chromium	16.2
Nickel	0.10
Aluminium	020

The microstructure is directly related to the mechanical properties and mechanical performance of the material. Therefore, changes in the microstructure always result in changes in the mechanical properties. Changes in the microstructure were determined by performing a grain morphology analysis (i.e., grain size, shape and orientation) and mechanical property changes were determined by mechanical testing (i.e., tensile testing and hardness testing).

Heat treatments were performed on the dog bone specimens to anneal the material, with the aim of attaining a relatively large-grained homogenous microstructure. Multiple uniaxial tensile tests and Vickers hardness tests were performed on heat-treated dog bone specimens in order to achieve a good microstructure and mechanical property starting-point for the investigation.

3.1.1 Heat treatment

Jha Jha *et al.* [101] developed the heat treatment technology for the continuous annealing of 17% Chromium ferritic stainless steel. This is represented in the phase diagram on Figure 3.2, which shows a strong correlation between the ferritic stainless steel microstructure, obtained when a heat treatment is performed. It also shows the two most important regions, namely:

- The single phase region (α) region beneath 860^{o}C.
- The double phase region (α+γ) above 860^{o}C.

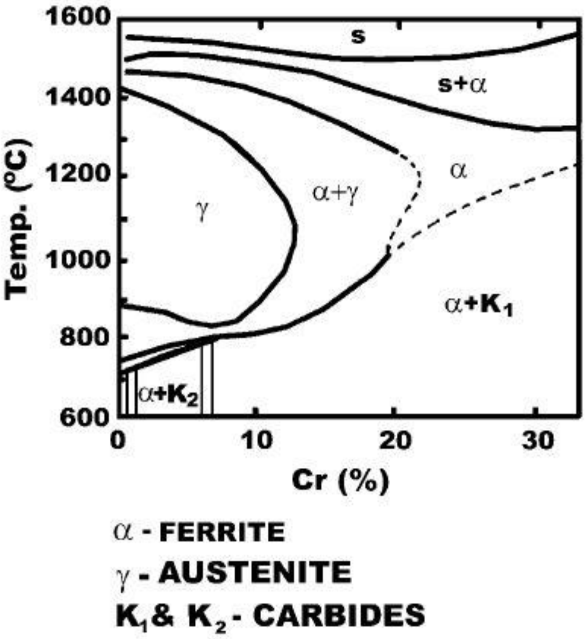

Figure 3.2: Phase diagram of Fe-0.05C-Cr alloy [101].

The main purpose of the heat treatments was to relieve internal stresses, to refine grain size and improve mechanical properties such as strength and hardness. The heat treatments performed were used as a basis to choose the most suitable heat treatment to anneal the plate specimens and allow a relatively large grain size, which would be utilised for repeated blast loading. Heat treatments were carried out in five different conditions. The first four involved heat-treating the material at four different temperatures ranging from 750°C to 900°C, at increments of 50°C, for the optimum distribution and size of grains (Table 3.2). In addition, a fifth heat treatment was performed. This was a two-step heat treatment and it resulted in the production of the most ideal microstructure, which contained large, homogeneous, equiaxed grains. The heat treatments (Table 3.2) were performed under vacuum conditions, followed by the slow cooling of the specimens in air.

Table 3.2: Heat treatments for the AISI 430 SS material under study.

Temperature(°C)	**Time(hours)**
750° C	1 hour
800° C	1 hour
850° C	1 hour
900° C	1 hour
2 Step Heat Treatment	
500° C and 800° C	1 hour and 2 hours

3.1.2 Specimen preparation

The as-received AISI 430 plate was in the as-rolled condition. The microstructure would have distinct features, depending on which plane the microstructure was viewed. A full chracterisation of the as-received material is shown in Figure 3.3. This figure reveals the microstructure variations in the rolling direction plane (RD-plane), the normal direction plane (ND-plane) and the tranverse direction plane (TD-plane). The most common plane to view a microstructure was the TD plane, where the grains were observed to be long and flat.

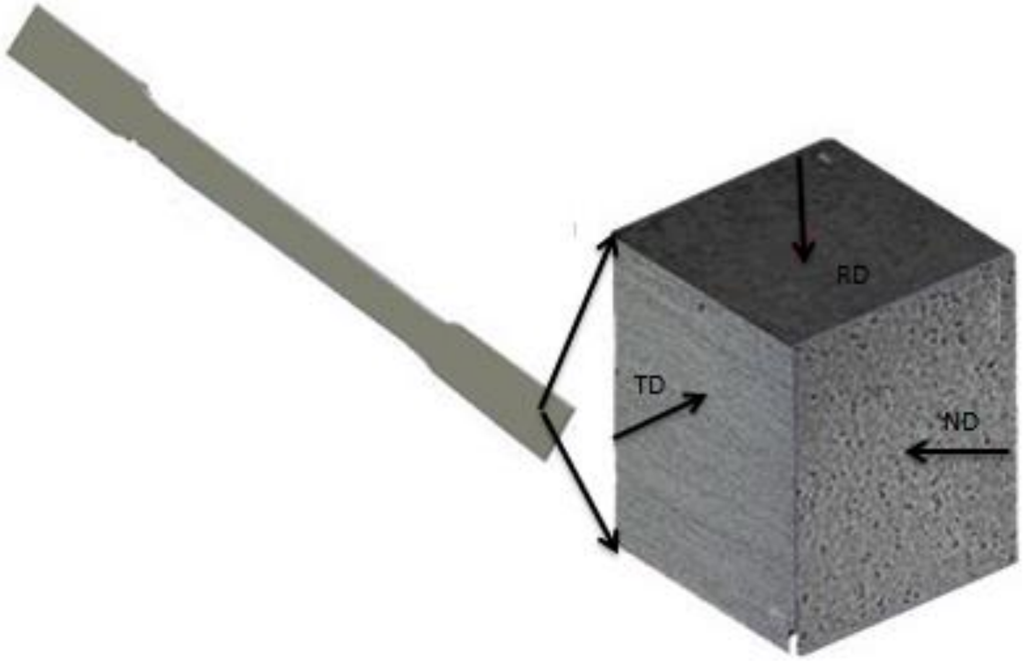

Figure 3.3: A schematic of the microstructures inside an as-received AISI 430 tensile sample.

A small piece of each heat-treated specimen was used for microstructural analysis. The piece was cut, using a cut-off wheel on an Imptech abrasive cutter, and set into an acrylic resin, using a Struers LaboPress 3 Hot Mounting apparatus. The sample was then ground, using a Struers knuth-Rotor-3 tabletop grinder, represented in Figure 3.4(a), and polished to a mirror finish with the use of a colloidal silica solution (OP-S) and the Struers Tetramin-25 automatic polisher, represented in Figure 3.4(b).

a) Struers knuth-Rotor-3 grinder b) Struers Tetramin-25 automatic polisher.

Figure 3.4: Photographs of the grinding and polishing equipment used for specimen preparation.

The polishing method used was based on Method C of the Struers Metalog Guide. The steps followed, including the details of the pads, lubricant, force and polishing times, are summarised in Table 3.4.

Table 3.3: A summary of the specimen preparation for the metallographic investigation.

Step	Pad(Grit)	Lubricant	Time(min)	Force(N)
Grinding	1200 SiC	Water	10-30 min	Moderate
Diamond Polishing	MD-Dac Pad	3µm	6 min	10N
Oxide Polishing(OP)	Chem Pad	OP solution(colloidal silica)	10 min	10N

Once the grinding and polishing process was complete, the samples were gently washed in water and degreasing liquid. Cleaning of the surface was necessary to remove any dirt that might have been left by the polishing and grinding of the sample. To further clean the sample, it was sonnicated in an ultrasonic bath for ten minutes in 70% lab ethanol. The final polished surface was then etched to reveal the grain boundaries of the microstructure. Etching was performed using a Stainless Steel Etchant, made up of 30 ml Nitric Acid (HNO_3), 10 ml water and 20 ml hydrochloric acid (HCL). The etchant was left on the surface for approximately 20 seconds at room temperature conditions (25°C).

3.1.3 Mechanical testing and heat treatment

The material properties of AISI 430 are presented in Table 3.5. This section presents the heat treatment results of the material by investigating the effect of each heat treatment on the microstructure evolution.

Table 3.4: Material properties of AISI 430 Stainless Steel.

Parameter	*Value*
Density	7.74 g/cm3
Specific heat(C)	0 - 100°C
E-young's modulus	200MPa
Rm	528MPa
A (% elongation)	29
Rp0,2 Proof stress	335MPa

3.1.3.1 Heat treatment results

The results of the heat treatments carried out at 750^{o}C, 800^{o}C and 850^{o}C revealed microstructures made up of small equaixed grains of variable sizes, as observed in Figure 3.5 (a - c). The varied grain sizes displayed in these microstructures were due to insufficient times for the restoration processes, such as recrystallisation, to occur. Furthermore, the 900^{o}C heat treatment produced a grain structure with carbide precipitates and heterogeneous grain sizes, as shown in Figure 3.5(d). The two-step heat treatment [*see* Figure 3.5(e)] revealed a good grain structure with large homogeneous, equiaxed grains. Austenite was not observed in the room temperature samples. This was in line with an AISI430 material that had undergone a heat treatment followed by a furnace cool, thus allowing long times for diffusion and the stable ferrite microstructure to form, as per the phase diagram.

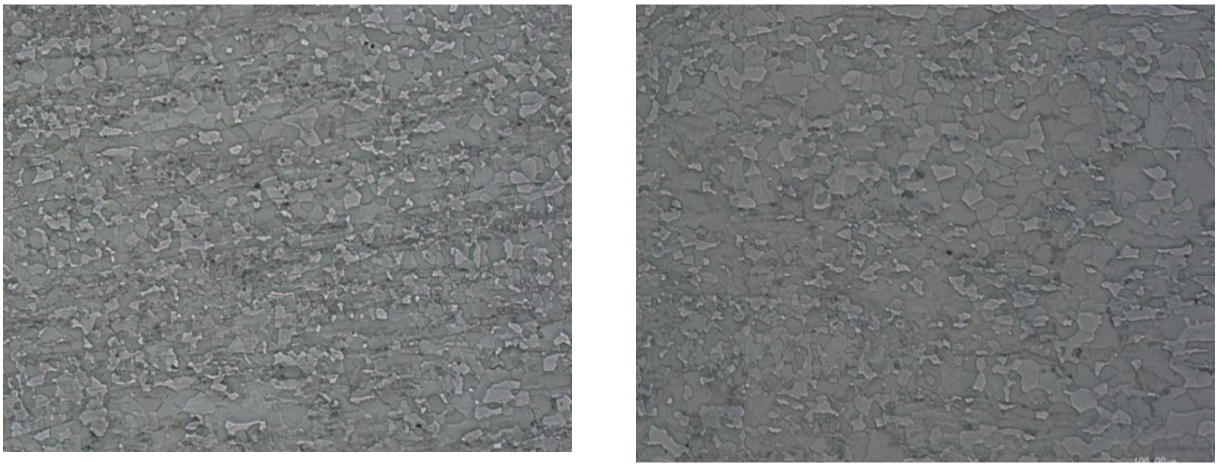

a)Heat treated @ 750 °C, 1 hr. 100µm

b) Heat treated @800 °C, 1 hr. 100µm

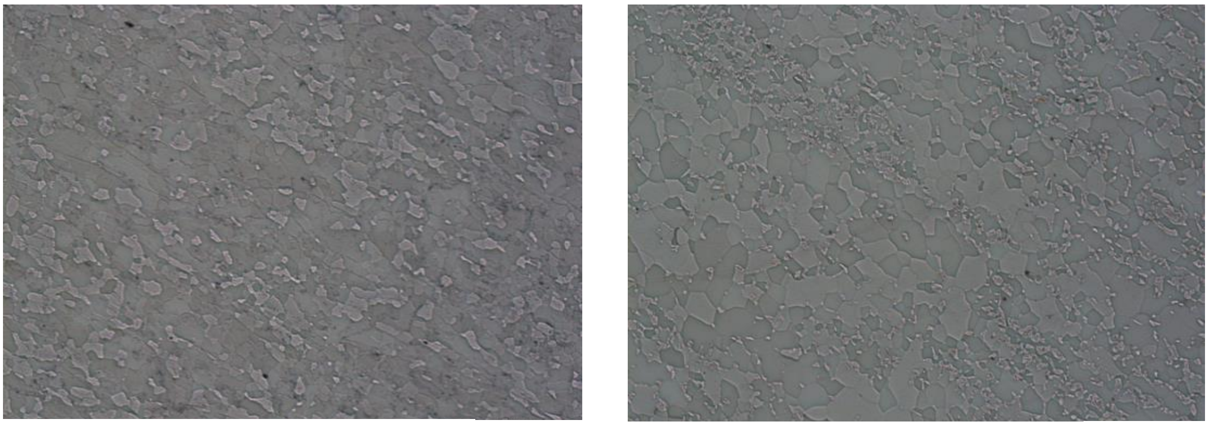

c) Heat treated @850 °C, 1 hr. 100µm

d) Heat treated @ 900 °C, 1 hr. 100µm

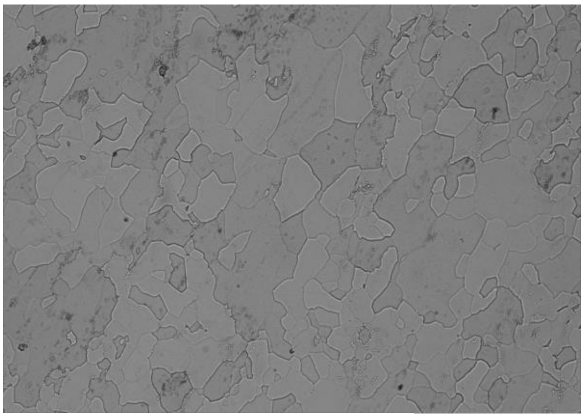

e) Heat treated by two-step (500 °C and 800 °C), 2 hr. 100µm

Figure 3.5: Microstructures achieved after different heat treatments.

Based on these findings, the two-step heat treatment was chosen as the most suitable heat treatment for heat-treating the plates. Further mechanical testing was performed on the heat-treated specimens in order to determine the mechanical properties. The specimens were tested for their tensile strength and Vickers hardness through tensile testing and macro-hardness testing. This served as a confirmation of the basis to choose the heat treatment procedure for heat-treating the plate samples before exposure to any form of blast loading experimentation.

3.1.3.2 Results from the tensile tests

The key properties of the mechanical tensile tests displayed a variation in the yield points and the percentage strain (ductility). The differences in the yield points occurred on all the heat-treated material, while the yield points ranged from 250-335MPa, and the ultimate tensile strength (UTS) values ranged from 438-586MPa. There was an occurrence of Luders bands from temperatures 800°C to 850°C. The two-step heat treatment produced a structure yield stress, UTS and ductility, which was desirable for blast loading conditions. The mechanical property data are presented in Table 3.5. Both yield strength (YS) and (UTS) increased with increasing temperature, with the exception of the two-step heat treatment. Furthermore, Figure 3.6 illustrates the engineering stress vs the strain results of the material. The raw results for these data are available In Appendix A.

Table 3.5: Mechanical properties for each heat treatment

Temperature(°C)	Yield Strength (MPa)	Tensile Strength(MPa)
750°C	246	438
800°C	249	447
850°C	327	586
900°C	335	545
500°C & 800°C (Two-Step)	297	454

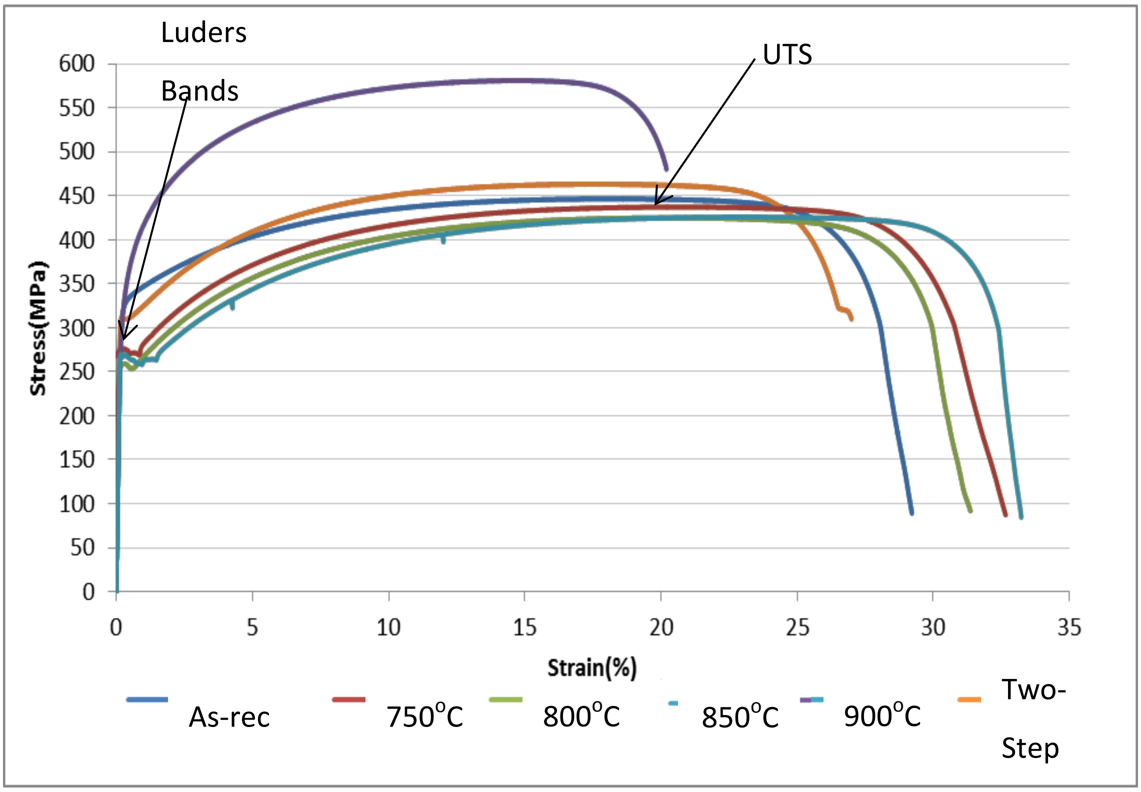

Figure 3.6: Engineering stress-strain curves for the different heat-treated samples.

3.1.3.3 Macro-Hardness tests

Vickers macro-hardness indentation tests, using the Zwick/Roell Hardness testing machine, were performed at seven different points in each of the heat-treated tensile specimens, as indicated in Figure 3.7.

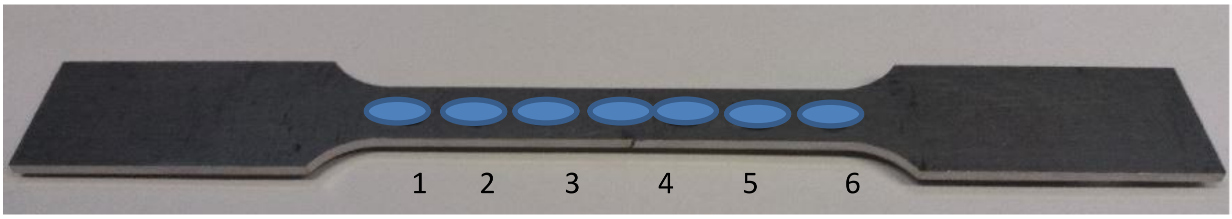

Figure 3.7: Dog bone Specimen Hardness points

The Vickers hardness tests were repeated at the same positions on seven specimens. The summary of the results is given in Table 3.6. Further representation of the property of hardness with temperature is presented in a bar graph.

Table 3.6: Results of Vickers Hardness (HV) Tests

			Heat Treatments			
	750°C	**800°C**	**850°C**	**900°C**	**2 STEP**	**As-Rec**
Mean	148.9	152	162.9	200.8	177.6	171.7
Median	149	151	162	199	173	172
ST. Dev	0.90	3.00	1.46	3.90	14.66	1.11
MAX	150	158	166	208	210	173
MIN	148	150	162	198	167	170

As the heat treatment temperature increased, the hardness increased with temperature, as represented in Figure 3.8. This was attributed to a faster diffusion at higher temperatures, which caused the increase in the hardness of the material.

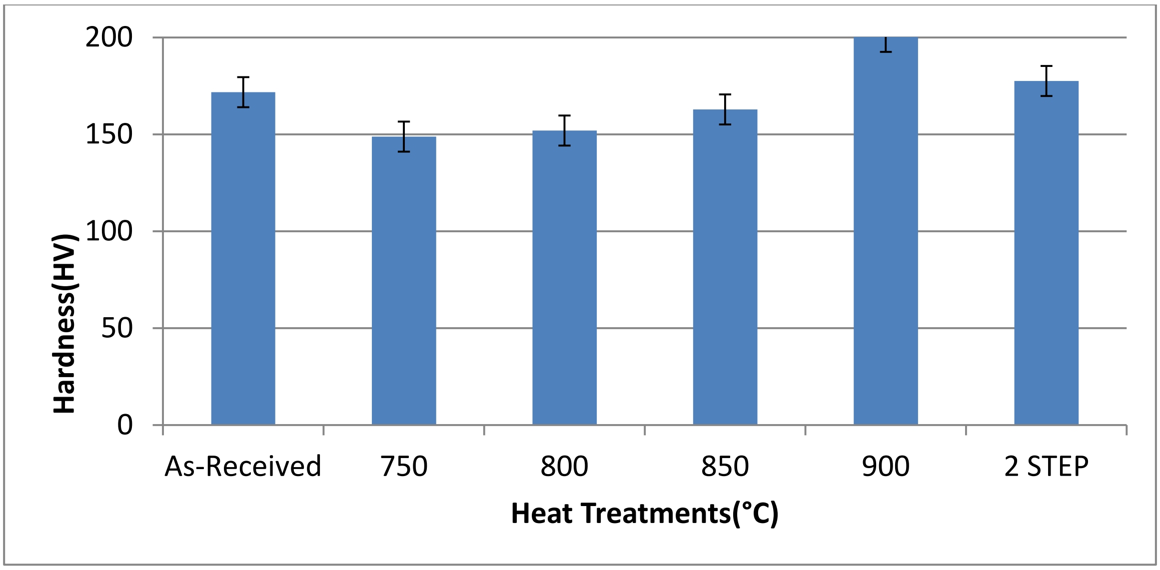

Figure 3.8: Hardness test bar graphs for the different heat-treated samples.

3.2 Blast loading experiments

3.2.1 Experimental details

The plate specimens were labelled according to the parameters used for the experiment. These parameters included the charge mass and diameter used, the number of blasts and plate number. The plate number was obtained by labelling the plates using integers from one to fifteen. The abbreviations of the parameters used for naming each plate are listed as:

- **D**-Charge diameter
- **M**-Charge mass
- **P**{1-15}-Plate number using an integer
- **B**-Number of blasts

For example, D34P1M10B5, where D was charge diameter 34 mm, M was charge mass 10 g, P was plate number 1 and B was the number of blasts, which were five blasts for this plate. The charge mass was varied for each test and the stand-off distance was kept constant for each of two loading conditions.

3.2.1 Specimen

The test plate specimens were made out of 2 mm thick AISI 430 stainless steel sheet metal. The surface area of the plate was 244 mm by 244 mm, leaving a circular plate with a 106 mm diameter exposed to the blast load. M12 bolts were used to secure the plate to the clamp frame of the pendulum. Therefore, the plate specimen had four holes near the corners of the plate. The size of the plate was similar to that of Henchie *et al.* [33].

3.2.3 Ballistic pendulum

All of the blast loading experiments in this project were performed on the ballistic horizontal pendulum. The period of oscillation was recorded in the form of lines that were traced on to tracing paper after the pendulum had swung upon detonation of the explosive. The initial velocity of the pendulum was calculated using the period and amplitude of the oscillation of the pendulum. Before the actual test, the pendulum was adjusted and levelled for balance and to ensure that it swung in one direction. The frontal components of the ballistic pendulum, as observed in the circled region of Figure 3.9, such as the clamp frames, the test plate and the connecters, were all weighed and the total mass was recorded. The back of the pendulum was balanced by using equivalent counter-masses of plates to balance the frontal weight of the pendulum. The I-beam was also weighed to obtain the total weight of the pendulum needed for forthcoming calculations.

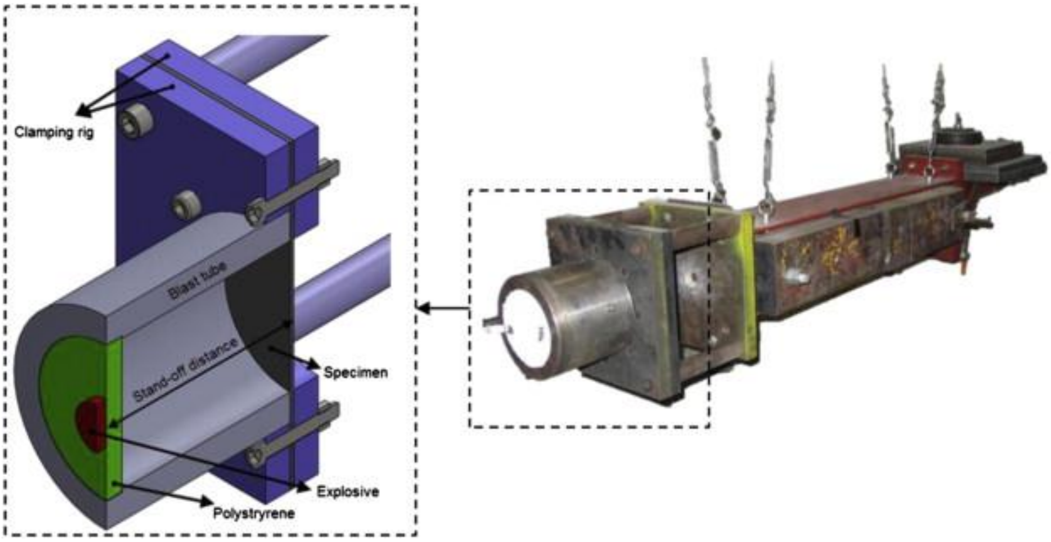

Figure 3.9: Photograph of the ballistic pendulum, highlighting a clamping rig for the uniform blast loading experiments [5].

3.2.4 Loading conditions

In total, 40 tests were performed for both the uniform and localised loading conditions. A total of thirteen blast tests were performed for the uniform loading condition and for the localised loading condition 27 blast tests were performed. For the uniform loading condition a stand-off distance of 150 mm was used and for the localised loading condition a stand-off distance of 13 mm was used. The clamping rigs for both these conditions, shown in Figure 3.10, were used to provide an exposed circular arc for blast loading.

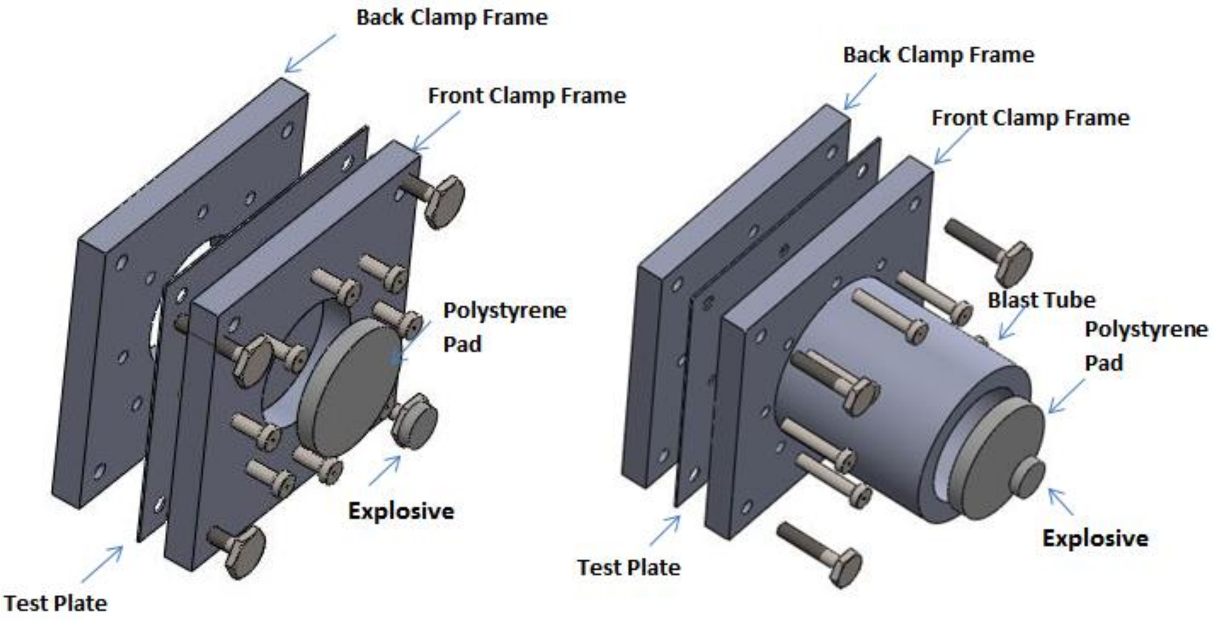

a) Localised loading condition b) Uniform loading condition

Figure 3.10: Schematic of the clamping rigs.

3.2.5 Explosive geometry

The explosive, in the form of a disk, was attached to a 13 mm thick polystyrene foam pad, using double-sided tape, and it was centrally positioned on to the frontal end of the pendulum. A wire for the detonator was attached to the central part of the explosive disc. The approximate burn speed of plastic explosive (PE-4) is 7500 m/s and it has a density of 7.74 g/cm3.

The explosive mass and the number of blasts per plate were constantly varied to result in a range of plate responses. The charge parameters for the explosive charges used are summarised in Table 3.7.

Table 3.7: Summary of Charge Parameters.

Loading	**Charge Diameter(mm)**	**Charge Mass(g)**	**Charge Height(mm)**
Uniform	34	10 and 30	6-9
Localised	40,25	4,5,6,7,9 and 11	5-7

3.3 Metallographic analysis

The blast loaded plates were cut along the deformed and undeformed regions into multiple smaller specimen sizes (listed from sample A to sample E). The samples cut were of similar sizes, 10 mm in breadth and 25 mm in length.

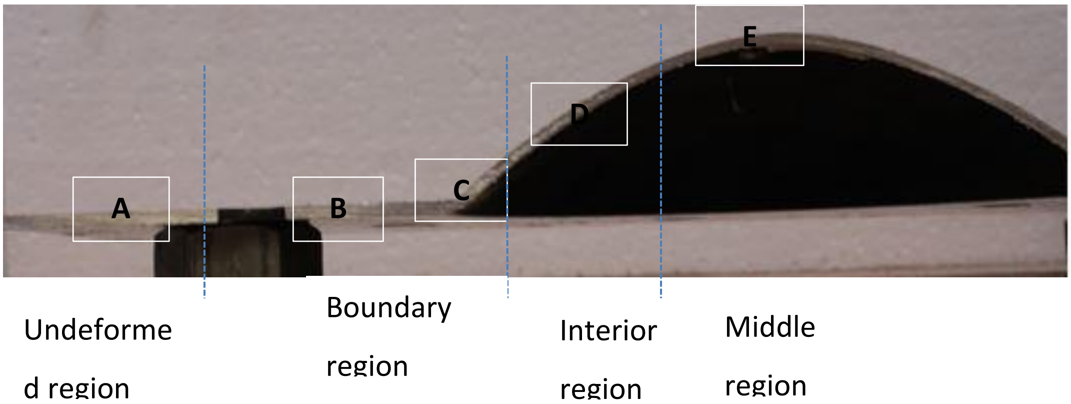

Figure 3.11: Photograph depicting regions of sampling of the specimens.

3.3.1 Preparation of samples for metallography

Sample preparation for the blast loaded samples was similar to the preparation of the heat-treated samples, as discussed in Section 3.1.2.

3.3.2 Optical microscopy

To assess the evolution of the microstructure, as well as the effect of blast loading on the AISI 430 stainless steel microstructure, sample parts of the blast loaded plates were optically observed under a conventional optical microscope. The microscope used was the Olympus BX51M microscope. The optical microscopy technique was used to track changes in features such as grain morphology, which included grain size, grain shape and orientation.

The technique for light microscopy works by having light from an incandescent source that is passed through a polariser so that all of the light getting through vibrates in a single plane. The beam is then passed through a prism, which separates it into components that are separated by a very small distance, equal to the resolution of the objective lens. The beams pass through the condenser, then the specimen. In any part of the specimen in which adjacent regions differ in refractive index the two beams are delayed or refracted differently. When they are recombined by a second prism in the objective lens, there are differences in brightness that correspond to differences in refractive index or thickness in the specimen.

3.3.3 Electron backscatter diffraction (EBSD) technique

Electron backscatter diffraction (EBSD) in a Scanning Electron Microscopy (SEM) is a technique that provides quantitative microstructural information about the crystallographic orientation and grain boundary statistics of materials. The nominal angular resolution limit is said to be 0.5µm and the spatial resolution is related to the resolution of the Scanning Electron microscope (SEM)[102]. EBSD is a technique that operates by arranging a flat, highly-polished specimen at an angle of 70^{o}. Electron diffraction occurs from the incident beam interaction point on the sample surface. With the beam stationary, an Electron Backscatter Diffraction Pattern (EBSDP) emanates spherically from this point.

The major reason for tilting the sample is to reduce the path length of electrons that have been backscattered by lattice planes as they enter the sample. This allows a far greater percentage of these electrons to undergo diffraction and escape from the sample, without losing any of their energy before being absorbed.

Maitland and Seizmann [102] stated that when the primary beam interacted with the crystal lattice in the sample (*see* Figure 3.12), low energy loss backscattered electrons were channeled and were subject to path differences that led to constructive and destructive interference. If a phosphor screen was placed a short distance from the tilted sample, in the path of the diffracted electrons, a diffraction pattern could be observed. Wright [103] stated that EBSD constructed image quality maps from electron backscatter diffraction data to provide useful visualisations and strain maps of the microstructure. The contrast in these maps arose from a variety of sources, which included phase, grain orientation, strain and grain boundaries.

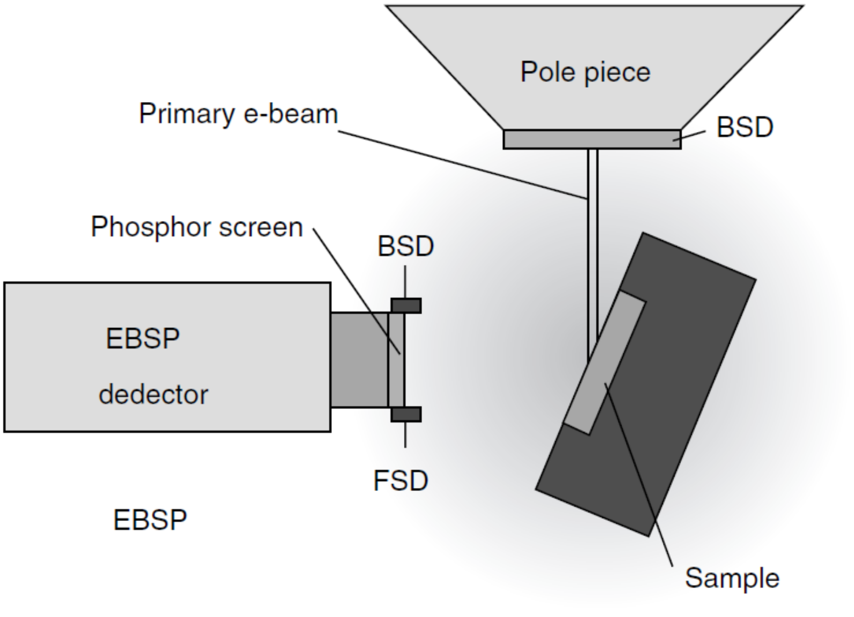

Figure 3.12: Schematic diagram for EBSD [102].

Metals usually have polycrystalline grain structures that are formed from a combination of crystal lattice orientations. Every crystal lattice has atomic planes that define the type of crystal system. EBSD contains an angular relationship between the planes, the symmetry of the crystal and orientation information. The EBSD technique uses EBSPs, which are electron backsacatter patterns, that use a map of the angular relationships between the atomic planes. Therefore, crystal orientation is determined by indexing the EBSPs produced by Kikuchi bands that correspond to planes in the crystal lattice. The term used by Venables [102], EBSP, has been universally adopted today to refer to the Kikuchi pattern used in an EBSD system (Figure 3.13). According to Session [104], the shadows of the spheres projected on to the camera were elliptical and their major axes could be extrapolated. The intersection of these lines defined the pattern centre.

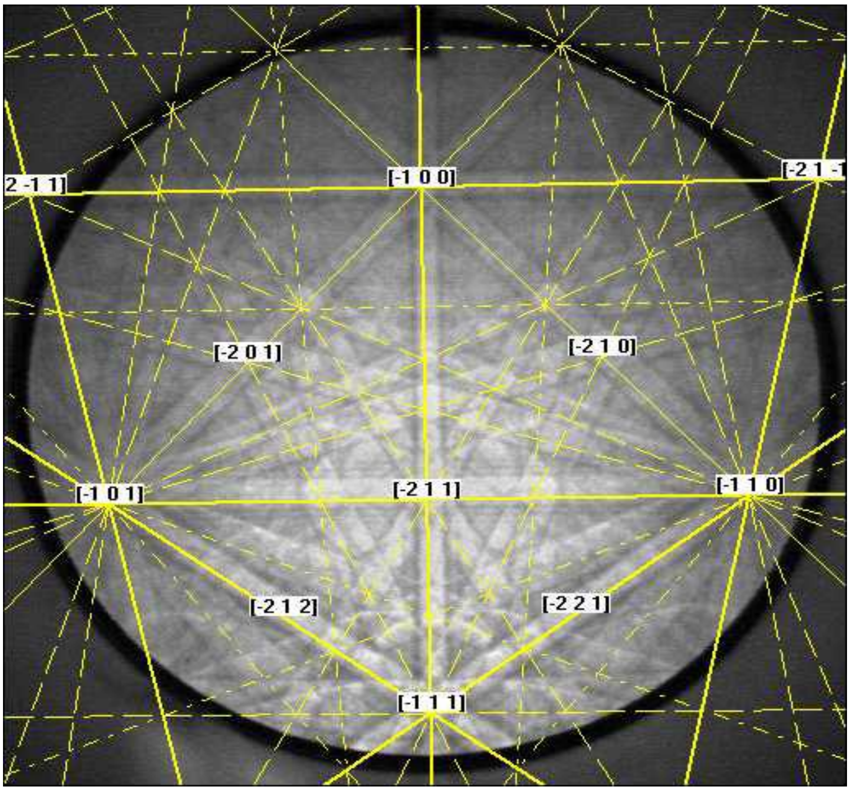

Figure 3.13: Venables' early EBSP indexed by modern software showing cryallographic planes[102].

The wave of these bands depended upon the the elctron beam wavelength and the lattice plane spacing. This type of relationship is further emphasized by Bragg's law, given by the Bragg's equation:

$$2\,d\sin\theta = n\,\lambda$$

This states that a plane wave is diffracted by a family of lattice planes, where θ is the incident angle of the wave and d is is the lattice spacing, λ is the wavelength and n is an integer in the order of reflection. The EBSD system uses high-energy electrons that are elastically scattered by atomic planes in a crystallographic sample. Lattice parameter and space group determine the inter-planar angles measured by distance on the pattern. The microscope produces an electron beam that scans across the sample, producing a number of EBSPs, connected to a computer, which instantaneously indexes each point and records orientation data for every beam position.

The FEI NovaNano SEM was used to perform EBSD analysis with the Oxford instruments EBSD system. An accelerating voltage of 20kV was used, with a working distance of 10 mm from the pole piece. HKL software was used for EBSD data acquisition and post-processing. During the acquisition process, HKL-EBSD software would automatically index the diffraction pattern; a set of Euler angles was assigned to the indexed point and the data were saved to a file. As the beam crossed into a different orientated lattice plane, the image would alter and a new diffraction pattern would be indexed and saved, which formed a map of the material's microstructure, known as an orientation map. The EBSD imaging software assigned a colour to each set of Euler angles to enable clear visual distinction between adjacent grains. Figure 3.14 presents an inverse pole figure (IPF) map and the effective use of colour produces a clear representation of the material's microstructure.

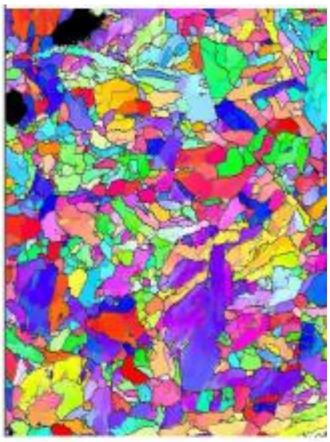

Figure 3.14: IPF orientation map of P91 steel after creep [105].

3.3.4 VMap Software

VMap software allows the manipulation and determination of microstructural features and the percentage of material in recrystallised form in the sampled area. The ability of VMap software to provide clear microstructural features is an essential component of this study, enabling a comparison of grain size and morphology between the samples. After blast loading, the VMap software performs a "grain-cleaning" routine, enabling the programme to clean the studied area for clear grain boundaries and grain sizes. After the cleaning, it was essential to set what values the grain boundaries should be and, for this study, the Low Angle Boundaries (LABDs) were set at 2° and the High Angle Boundaries (HAGBs) at 15°. Furthermore, the “Reconstruct” option was used to obtain the boundary statistics for the grains.

A grain is constructed by identifying a reference pixel and then classifying whether adjacent pixels belong to the same grain or sub-grain, based on the misorientation. If the misorientation of adjacent pixels is equal or greater than the high angle grain boundary (HAGB) setting, the pixels are then deemed to belong to a different grain. The "new grain" pixel is then classified as the reference pixel and the process continues until the complete map is constructed. VMAP allows two methods to reconstruct the acquired EBSD map, depending on user preference [116].

CHAPTER 4

4.1 Blast loading results and discussion

4.1.1 Uniform blast loading results

This section gives the effect of each parameter on plate failure by an extensive representation of quantitative methods as a way to depict the experimental data and results. It also provides detailed results pertaining to the plates exposed to uniform blast loading conditions.

a) General plate deformation

The deformation feature was characterised by a large general dome shape, as demonstrated in Figure 4.1. This type of deformation feature was similar to the global plastic dome reported in previous studies by Ranwaha *et al*. [32] and Jacob *et al*. [34] for plates subjected to uniform blast loads.

Figure 4.1: Photograph of cross sectional profile test plate (D34P3M10B3 - Charge Diameter=34 mm, Plate Number=3, Charge Mass=10 g and Number of blasts=3 blasts).

b) Thinning

Thinning was observed at the clamped boundary of the blast loaded plates. The amount of thinning varied with both the localised and uniform loading conditions, thus it was difficult to quantify. This thinning was similar to the necking of sspecimens during a tensile test. Figure 4.2 presents a photograph of a section that thinned as a result of repeated blast loading. The results were similar to the experimental work performed by Ranwaha *et al*. [32] and Henchie *et al*. [33], where it was shown that, in the case of integral plates, thinning occurred at the clamped boundary region. Thinning sections of the blast loaded plates eventually led to tearing at higher impulses.

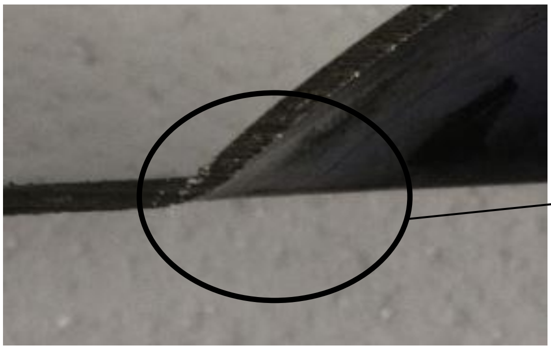

Figure 4.2: Photograph showing the thinned section at the boundary of plate (D34P3M10B3 - (Charge Diameter=34 mm, Plate Number=3, Charge Mass=10 g and Number of blasts=3 blasts).

c) Tearing

According to Jacob *et al*. [34], as the impulse was increased beyond thinning, tearing started to occur. Complete tearing (Mode II) at the boundary was observed for the plate exposed to a 30 g charge mass at an impulse value of 40Ns. Observations of boundary tearing indicated that the number of blasts needed to cause boundary tearing failure decreased as the charge mass was increased. Complete tearing failure at the boundary (Mode II) is presented in Figure 4.3.

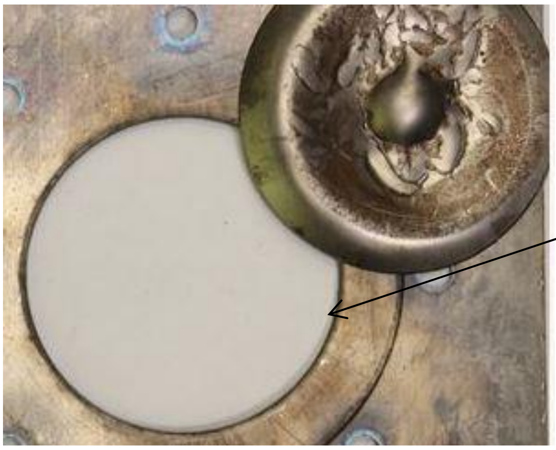

Figure 4.3: Photograph showing complete tensile tearing at the boundary (Mode II) (D34P4M30B1 - Charge Diameter=34 mm, Plate Number=4, Charge Mass=30 g and Number of blasts=1 blast.)

d) Observations of midpoint deflection and Impulse of the blast loaded plates

The experimental results shown in Table 4.1 display the effect of the parameters of the experiment: load diameter, charge mass and number of blasts on the midpoint deflection and impulse of the plates. Plates subjected to uniform repeated blast loading, using a charge mass of 10 g and with a load diameter of 34 mm, induced an increase in the impulse and midpoint deflection of the plates. In addition, the plate deformed differently, depending on the number of blasts. Therefore, the results suggested that the range of tests carried out showed an increase in the impulse with an increase in the number of blasts. A similar trend was observed in the relationship between the number of blasts and the midpoint deflection of the plates.

Table 4.1: Summary of uniform loading results.

	Load Diameter(mm)	**Charge Mass(g)**	**No of blasts**	**Impulse (N.s)**	**(δ)Midpoint deflection (mm)**	**Failure Mode**
D34P2M10B1	34	10	1	16.79	18.56	Mode Ib
D34P3M10B3	34	10	1	16.16		Mode I
			2	19.96		
			3	24.50	28.56	
D34P1M10B5	34	10	1	19.24		Mode I
			2	14.13		
			3	19.33		
			4	21.03		
			5	29.50	30.21	
D34P4M30B1	34	30	1	40.01	-	Mode II

The results displayed variations of inelastic deformation failure (Mode I) as the blast loads were gradually increased for the plates exposed to the 10 g charge mass. These variations are displayed in the photographs of Figure 4.4. The five blasts of 10 g showed the highest midpoint deflection, owing to the greater number of blasts.

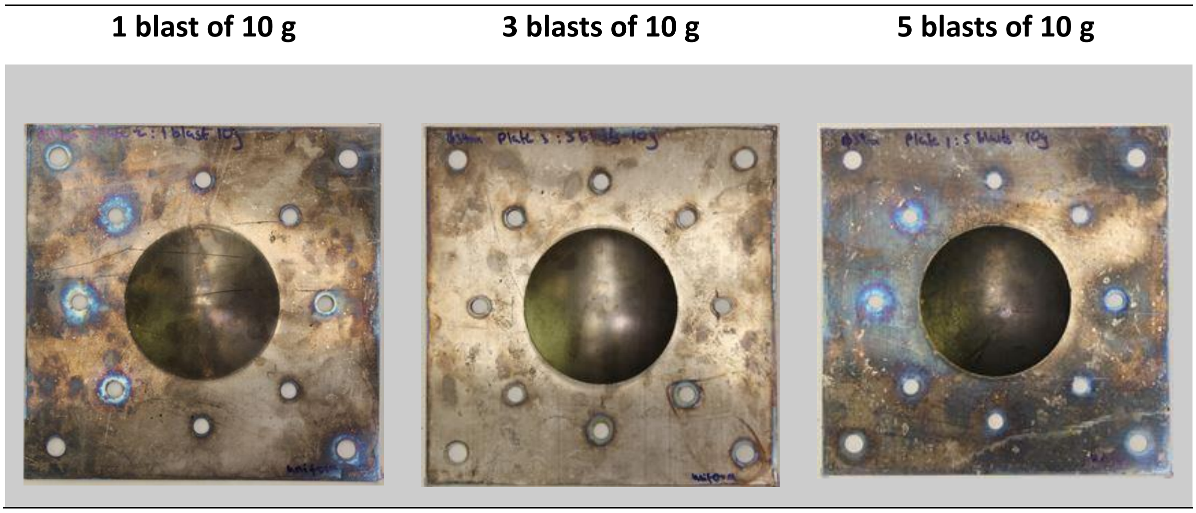

a) Photographs of plates subjected to an increasing number of blasts, using a charge mass of 10 g.

b) Photograph of deformed test plate profiles from one, three and five blast loads, using a 10 g charge mass.

Figure 4.4: Photographs of plates subjected to one, three and five blast loads, using a charge mass of 10 g

To summarise, it was observed that repeatedly loading the plate, using the same charge mass, increased the midpoint deflection and impulse of the plates. The plate that was subjected to the highest number of blast loads produced the highest impulse and midpoint deflection and the plate subjected to the lowest number of blast loads produced the lowest impulse and midpoint deflection.

4.1.2 Effects of charge mass on plate failure

The explosive charge played a critical role during the blast loading of structures. A change in the charge parameters, i.e. the mass and diameter, changed the conditions of the experiment. This led to a change in the response of the specimen. The results of one plate blast loaded three times using a charge mass of 10 g and another plate subjected to one blast using a charge mass of 30 g were compared, as is shown in Figure 4.5.

It can be observed from Figure 4.5 that, if a plate is subjected to three blasts of 10 g charge mass, the plate response is an inelastic deformation failure. However, by subjecting the plate to one blast of 30 g charge mass, there will be immediate capping of the plate.

In summary, changing the charge mass changed the type of failure experienced by the plate.

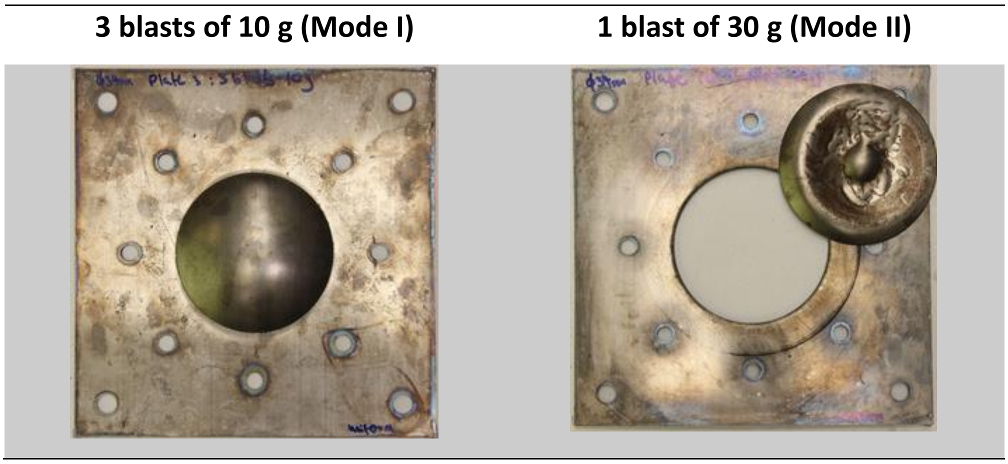

a) Photographs of plates three blasts of 10 g and one blast of 30 g.

b) Photograph highlighting the differences in failure modes.

Figure 4.5: Photograph of test plates subjected to repeated blast loading (Comparison between 3 blasts of 10 g plate and 1 blast of 30 g plate).

4.2 Localised blast loading results

This section presents results for the localised blast loading condition where the stand-off distance used was 13 mm for 2 mm thick AISI 430 stainless steel plates. Comparisons to previous studies were made in terms of midpoint displacement, deformation profiles, failure modes and impulse to failure mechanisms. Table 4.2 summarises the results of blast tests performed for this blast loading condition.

Table 4.2: Summary of localised blast loading tests

Plate Name	**Charge Mass(g)**	**Number of blasts**	**Midpoint Deflection**	**Failure Mode**
D40P5M6B1	6	1	22.80	Mode I
D40P6M6B2	6	2	23.57	Petalling
D40P9M4B1	4	1	17.90	Mode II
D40P8M4B2	4	2	21.93	Mode II
D40P7M4B1	4	3	25.02	Mode II*c
D40P10M5B1	5	1	18.30	Mode II
D40P11M5B2	5	2	24.05	Mode II
D40P12M5B3	5	3	21.45	Mode II*c
D25P15M7B1	7	1	26.15	Mode I
D25P14M9B1	9	1	33.53	Mode Itc
D25P13M11B1	11	1	26.52	Mode IIc

a) General plate deformation

The general shape observed was a minor dome, superimposed by a global dome. The plate bent from the point of inflection and changed towards the plate centre (*see* Figure 4.6), where the displacement was maximum at the fixed boundary. Additionally, it was observed that the diameter of the inner dome superimposed by the global dome at the centre of a plate increased with an increase in charge size (mass and diameter). A similar resultant shape was observed by Radford *et al*. [88].

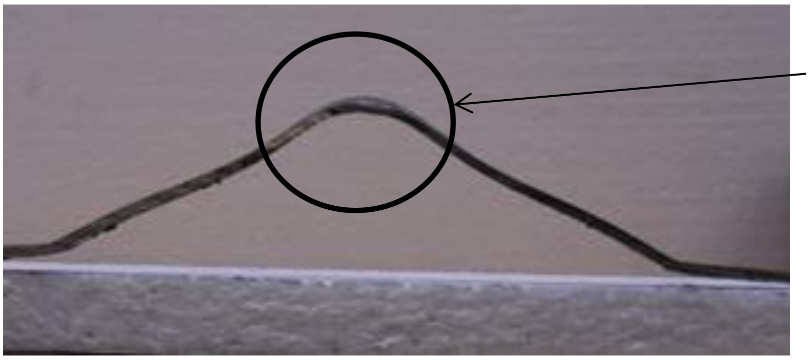

Figure 4.6: Photograph representing the shape obtained when a plate was blast loaded in localised conditions.

b) Thinning

Thinning was observed in two parts of the specimen, the point of inflection, where there was change in the curvature near the inner dome, and at the boundary, near where the plate was clamped, as circled in Figure 4.7. The results of thinning observed in the central area between the inner dome and global dome were similar to those obtained by Radford and Nurick [88], Wierzbicki and Nurick [86], Chung Kim Yuen and Nurick [107] and Nurick and Thomas [108]. The amount of thinning varies with both the localised and uniform loading conditions, thus it is difficult to quantify.

Figure 4.7: Photograph of the thinning of a plate subjected to localised loading conditions.

c) Tearing

Plate tearing occurred beyond the point of thinning. At the different charge diameters (25 mm, 34 mm and 40 mm) and as the mass of PE4 was increased, observations changed from partial tearing to tearing of a large section of the area around the point of impact. In a series of blast tests performed on a plate subjected to two blasts, using a charge mass of 5 g, there was partial tearing beyond the point of thinning, as is shown in Figure 4.9. The tearing failure was in the inner dome and started at the point of inflection of the plate where the change in curvature of the plate began.

Partial tearing-
Mode II*c

Figure 4.9: Photograph of tearing at the inner dome of the plate (D40P12M5B3-charge diameter=40 mm, charge mass=5 g and no. of blasts=3).

d) Observations of midpoint deflection of the blast loaded plates

The midpoint deflection increased with the number of blast loads. This was due to the fact that, with each blast, the material expanded plastically and came ever-closer to tearing. These results corroborated the results of Henchie *et al*. [33], who showed a linear relationship with a positive gradient between the number of blasts and the midpoint deflection of the plates.

The increase in the midpoint deflection was attributed to the increase in the stand-off distance of the plate as it was deformed. Figure 4.12 displays these linear trends for the various charge masses of the blast loaded plates. As the plate was repeatedly blast loaded it plastically deformed until it reached its ultimate tensile strength, beyond which point it necked closer to the point of failure. (Ferritic stainless steel has a high yield strength of about 335MPa and can be plastically deformed to points greater than 400MPa, thus a high midpoint deflection is expected for these types of steels.)

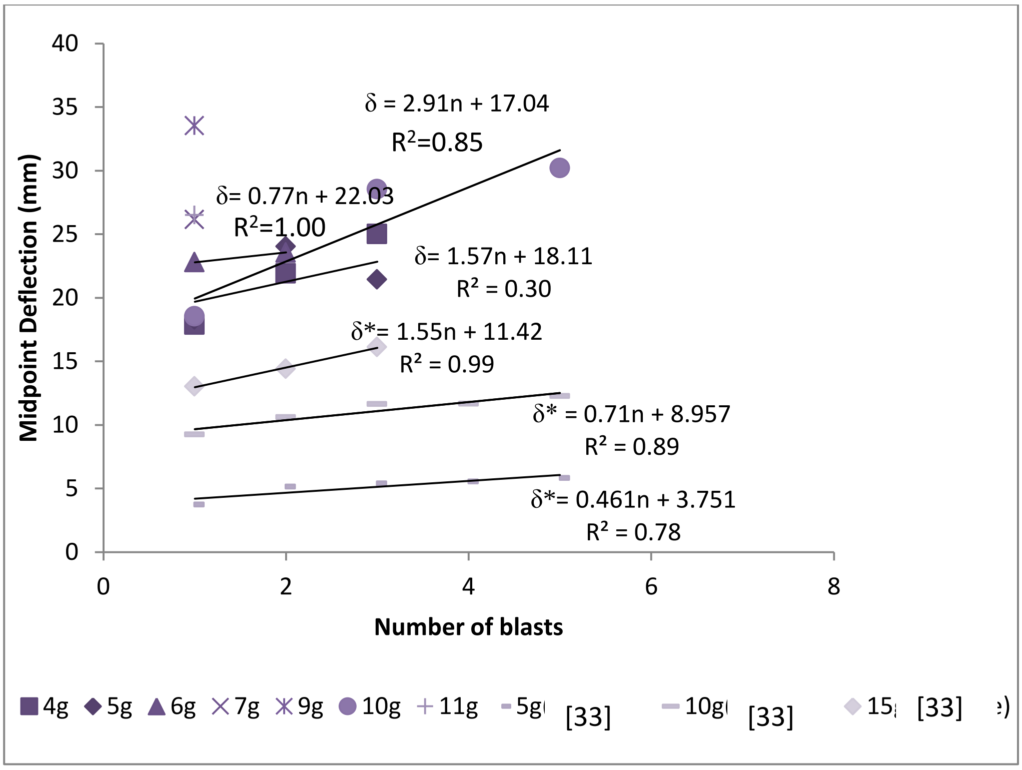

Figure 4.12: Graphs of midpoint deflection vs number of blasts.

4.2.2 Effects of charge mass on plate failure.

Increasing the charge mass resulted in a variety of failure modes. To emphasise the importance of charge mass on plate failure, plates subjected to two blasts were compared. One plate was blast loaded, using a charge mass of 5 g, and another plate was blast loaded, using a charge mass of 6 g. The latter plate failed by petalling. However, the former inelastically deformed. This is shown in Figure 4.10. Therefore, It was concluded that even one incremental increase in the charge mass could produce an enormous difference in plate response.

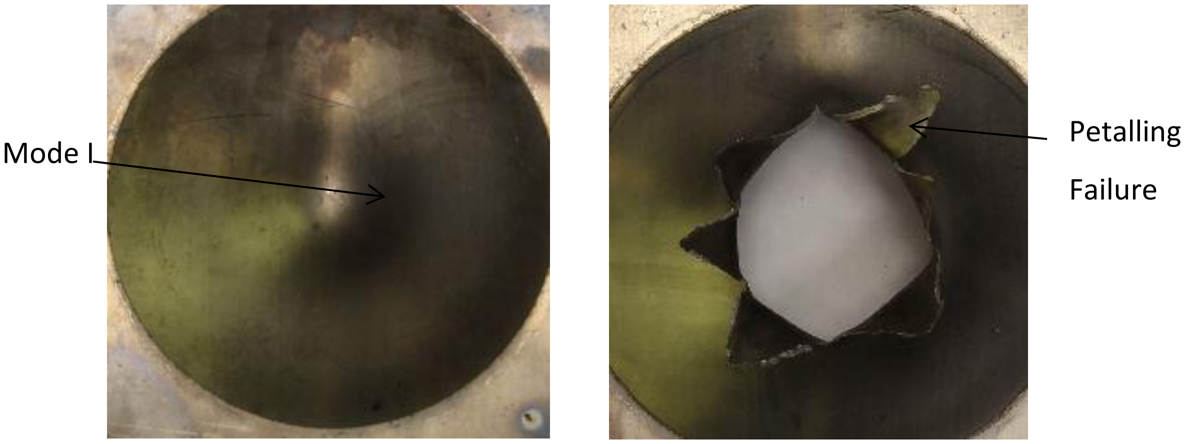

a) Inelastic Deformation of plate with a charge mass=5 g, no of blasts=two.

b) Petalling failure of a plate with charge mass=6 g, no of blasts=two.

Figure 4.10: Photographs showing the comparison of failure modes of plates exposed to 6 g charge mass vs 5 g charge mass.

Plates exposed to different charge masses are displayed in Figure 4.11. The deformation failure profiles indicated an increase of localisation of the blast load towards the midpoint. The plates were all exposed to a charge mass that ranged from 7 g to 11 g. The response of the plate exposed to a 7 g charge was an inelastic deformation failure (*see* Figure 4.11).

The plate blast loaded using a charge mass of 9g displayed thinning at the point of inflection and this was indicated by a line (*see* circled in Figure 4.11(b)) around the central area of the plate. This plate displayed the failure Mode Itc*. In addition, the plate exposed to a charge mass of 11 g showed capping (Mode IIc) in the central area of the inner dome, as is shown in Figure 4.11(c). This was due to the 25 mm load diameter used to blast load the plate.

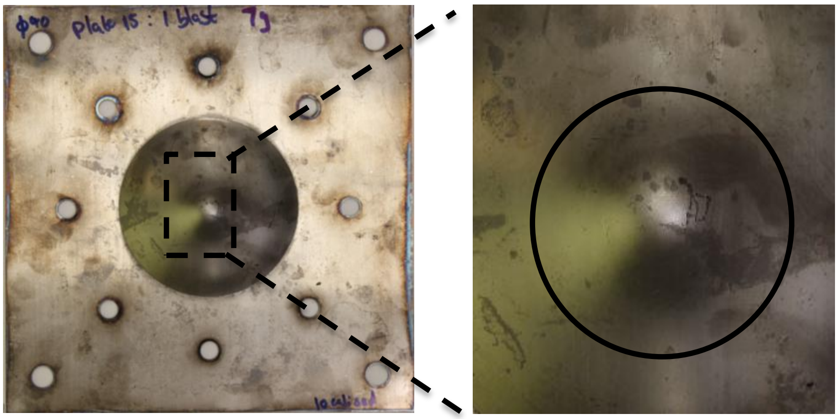

a)Plate subjected to 7 g of PE4, exhibiting Mode I

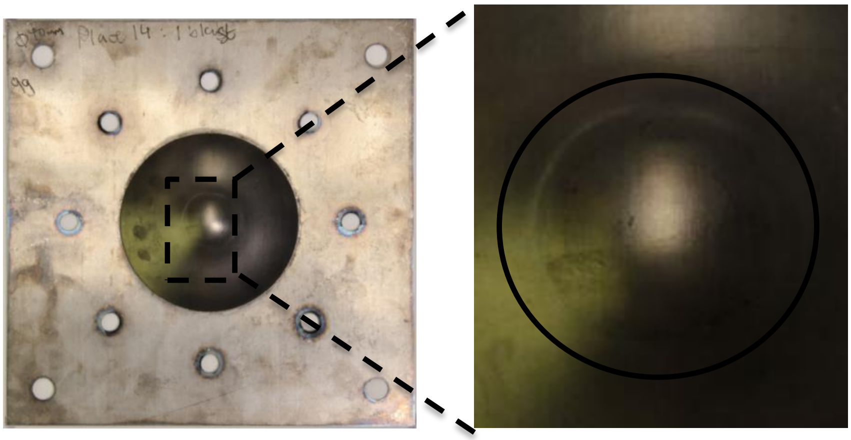

b) Plate subjected to 9 g of PE4, exhibiting Mode Itc*.

-

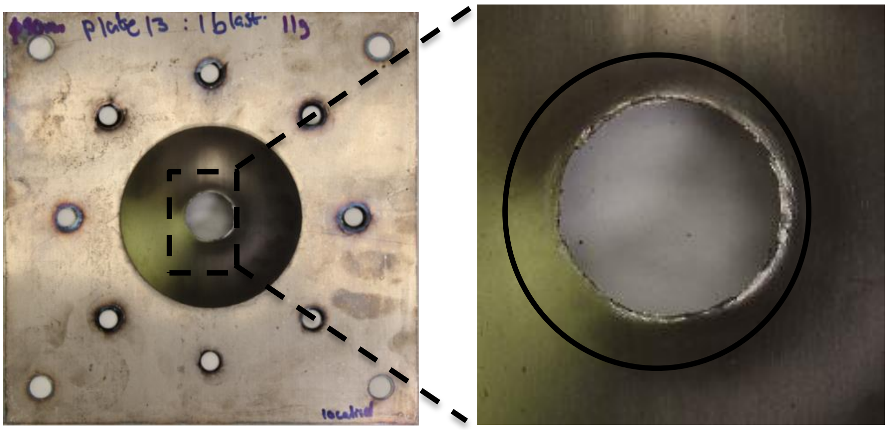

c) Plate subjected to 11 g of PE4, exhibiting Mode IIc.

Figure 4.11: Photographs of plates exposed to different charge masses.

4.2.3 Relationship between midpoint deflection and impulse

The relationship between midpoint deflection and impulse is given in Figure 4.13. The impulse is represented by the slope of the straight line equation. The experimental tests for repeated blast loading displayed a direct relationship between the midpoint deflection of the plates and the impulse. The midpoint deflection of the blast loaded plate increased with increasing impulse, as displayed by the linear trend.

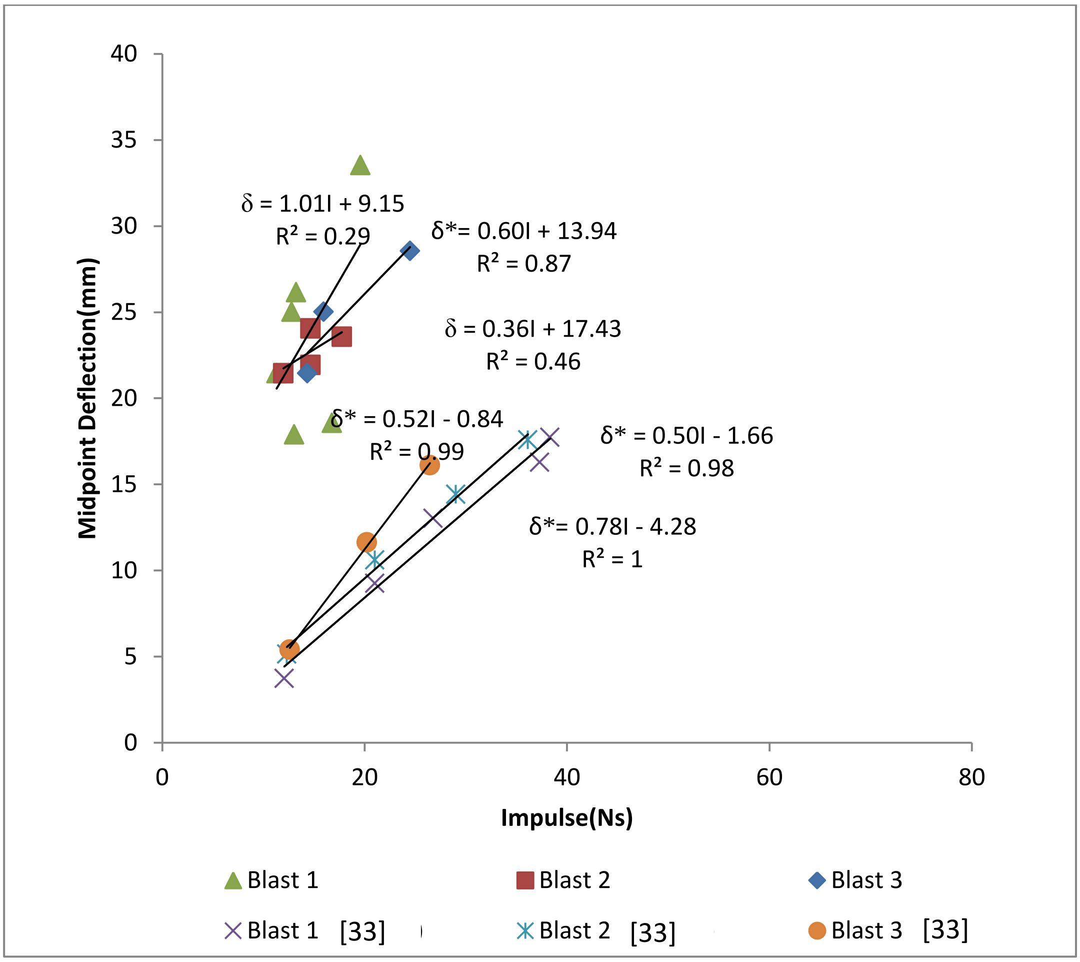

Figure 4.13: Impulse (N.s) vs Midpoint deflection (mm) plots for a 2 mm plate.

4.3 Dimensional analysis

4.3.1 Relationship between Jones number vs deflection plate thickness ratio

Jones [92] introduced a damage number to predict the large inelastic deformations obtained in fully-clamped uniformly blast loaded plates. This damage number is represented by the following equations:

$$\lambda = \frac{\mu V_O^2 L^2}{M_O H} \qquad \text{Eq. 4.1}$$

$$\lambda = \frac{4I^2}{\pi^2 R^2 \sigma_O \rho H^4} \qquad \text{Eq. 4.2}$$

Modification of this Jones damage number included the incorporation of the loading parameter γ, and the new modified Jones number became:

$$\lambda_s = \lambda_{\gamma^2} = \frac{4I^2\gamma^2}{\pi^2 R^2 \sigma_O \rho H^4} \qquad \text{Eq. 4.3}$$

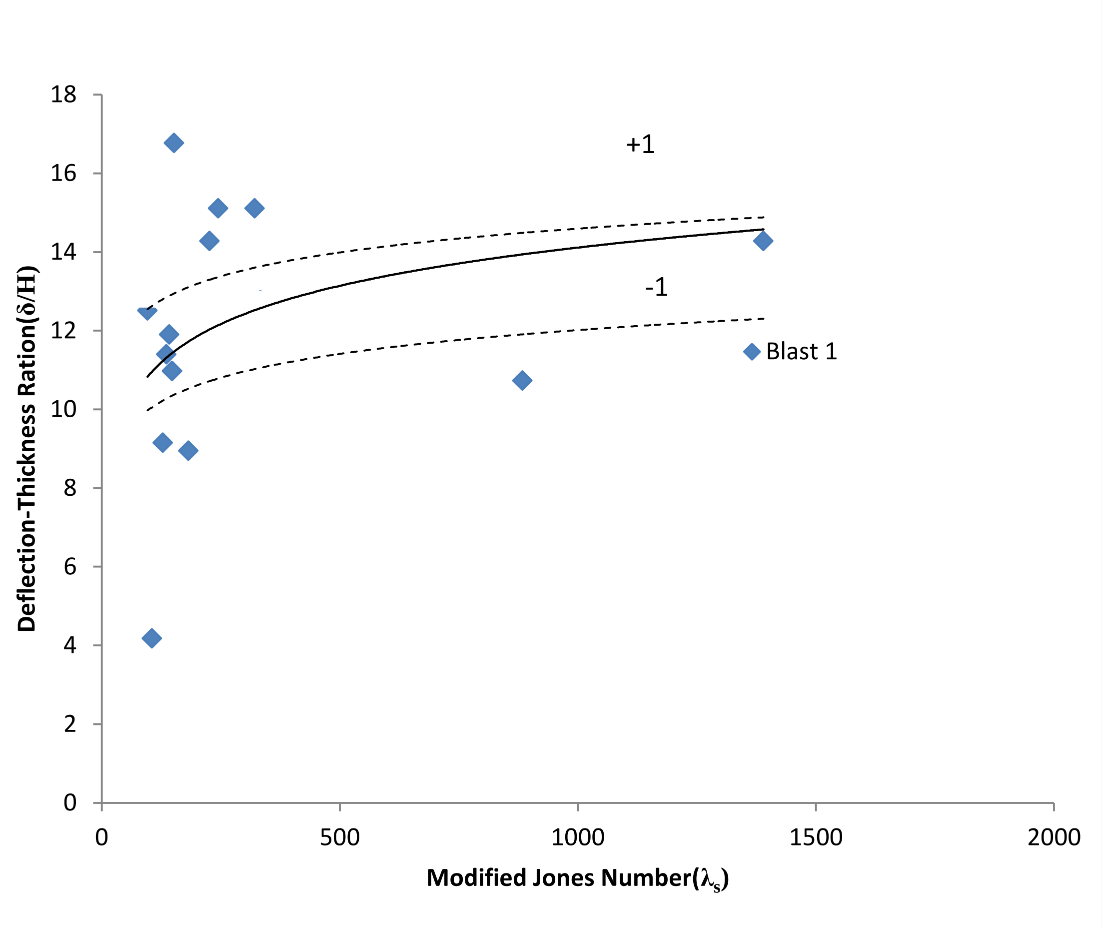

Figure 4.14: Modified Jones Number vs Deflection-Thickness ratio.

Figure 4.14 displays the relationship between the midpoint deflection-thickness ratio and the modified Jones number for single blast loads. The results were compared to those obtained by Henchie *et al*.[109] (see Figure D3 in Appendix D) in similar experiments carried out at a stand-off distance of 150 mm. The results obtained fell within the 90% confidence intervals. However, four data points were outside the confidence intervals, owing to thinning observed after the blast loading experiments in the deformed plates. Jones [92] reported on this type of relationship for deformed plates and it did not hold for completely failed plates. Therefore, the points outside the confidence intervals were for those plates that had either completely failed or thinned extensively.

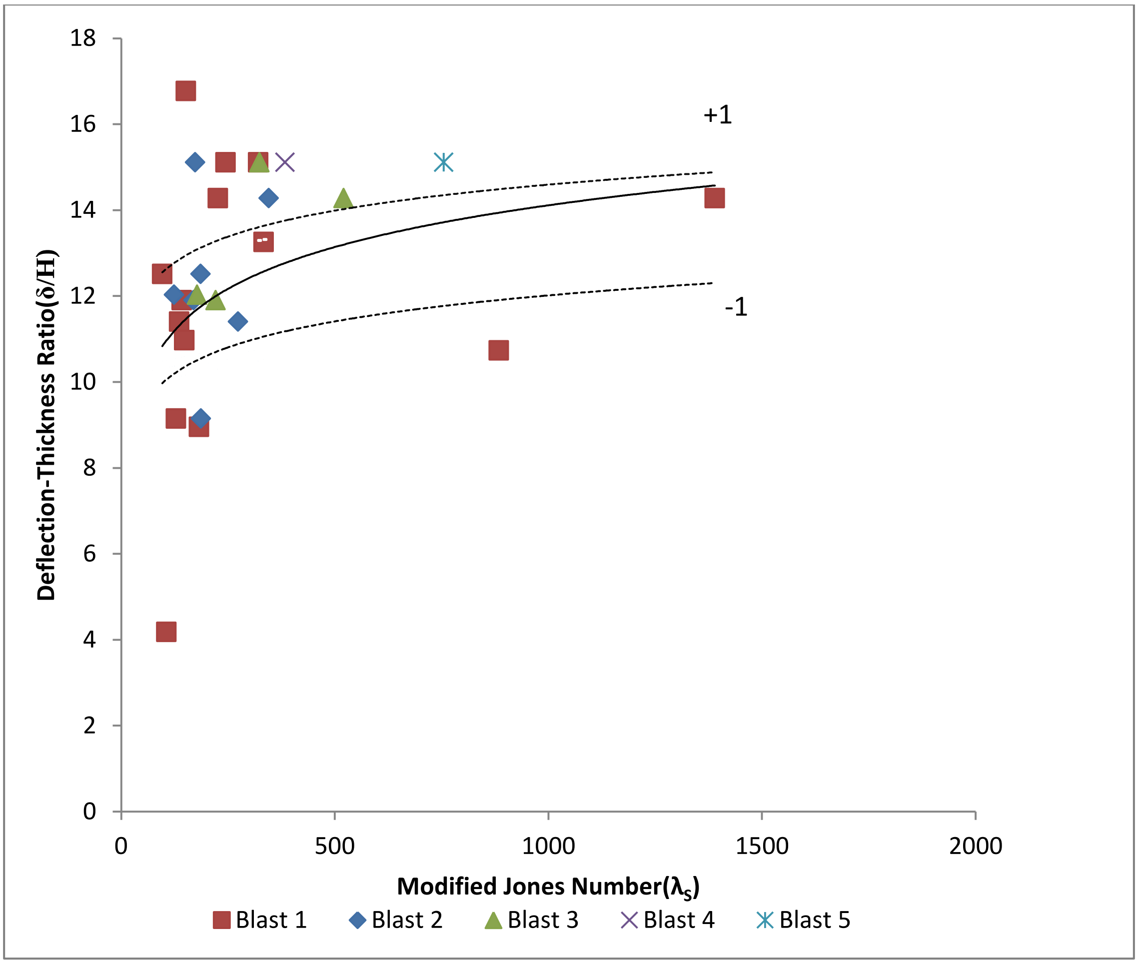

Figure 4.15: Modified Jones Number vs Deflection-Thickness ratio.

In addition, Jones [92] reported that the relationship between the midpoint deflection-thickness ratio and the Jones number only held for single blast loads. This relationship was not observed for repeated blast loading conditions. However, Figure 4.15 displays the relationship between the Jones number and midpoint deflection-thickness ratio for all the repeatedly blast loaded plates. It was observed that a majority of the plates blast loaded twice fell within the confidence range of the Jones damage number with only three points falling outside this interval. In addition, the same was observed for plates loaded three times with only two points falling outside the confidence intervals. Plates that were blast loaded more than three times were observed to fail or thin more easily, thus immediately falling out of the confidence range of the Jones damage number.

4.3.2 Relationship between Nurick and Martin damage number vs the deflection-plate thickness ratio

4.3.2.1 Nurick and Martin damage number for uniform blast loading

Nurick and Martin [93] used a damage number (*see* Eq. 2.24) to evaluate some of the experiments by comparing the damage number and the displacement-thickness ratio. Figure 4.16 compares data for repeated uniform blast loading. There was a significant deviation between the results and the theoretical prediction as a threshold value. In addition, an increase in the number of blasts caused a larger deviation from the dimensionless impulse as the number of blast loads increased.

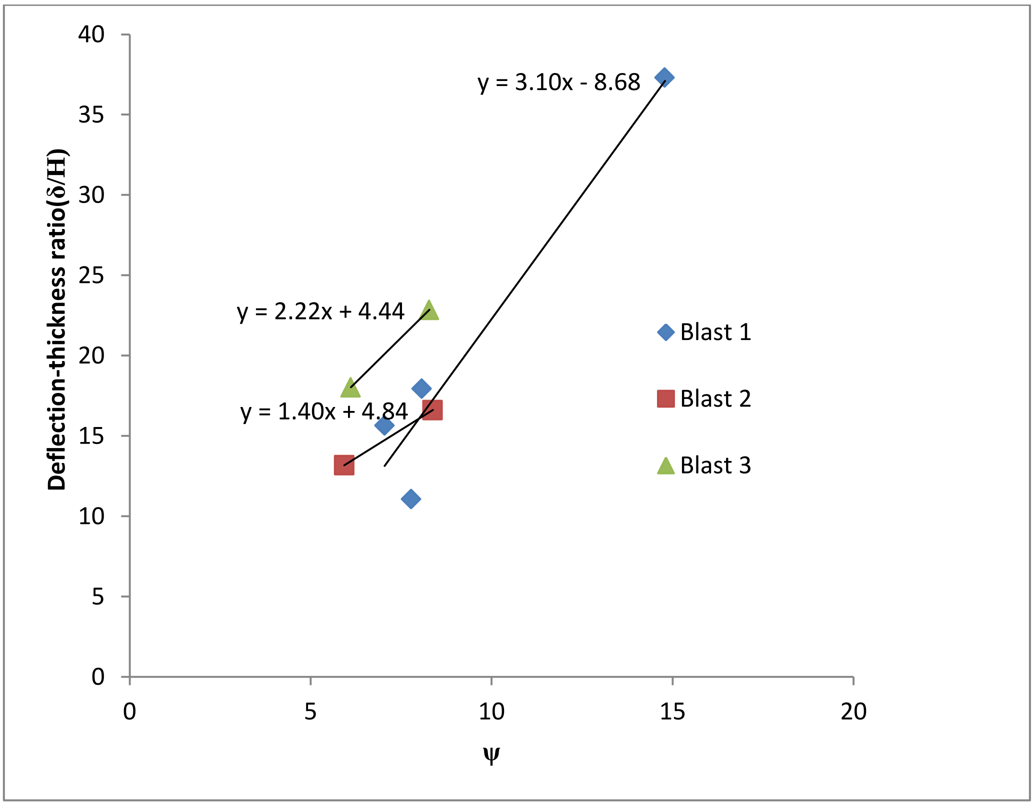

Figure 4.16: Nurick and Martin's damage number (ψ) vs deflection-thickness ratio (δ/H) for repeated blast loading of uniformly blast loaded plates.

4.3.2.2 Nurick and Martin damage number for localised blast loading

A similar relationship was observed in plates that had been blast loaded. The plates exposed to a higher number of blasts displayed a higher damage number and this is represented by the deflection-thickness ratio. Delta is the measured maximum deflection. The deflection is normalised with the plate thickness by dividing delta by the plate thickness. Therefore, the amount of thinning increased, indicating the proximity of a tear in the plate. Depending on the charge mass the plates had been exposed to, some plates did indeed tear and those torn plates all had a high Nurick and Martin damage number, as indicated in Figure 4.17.

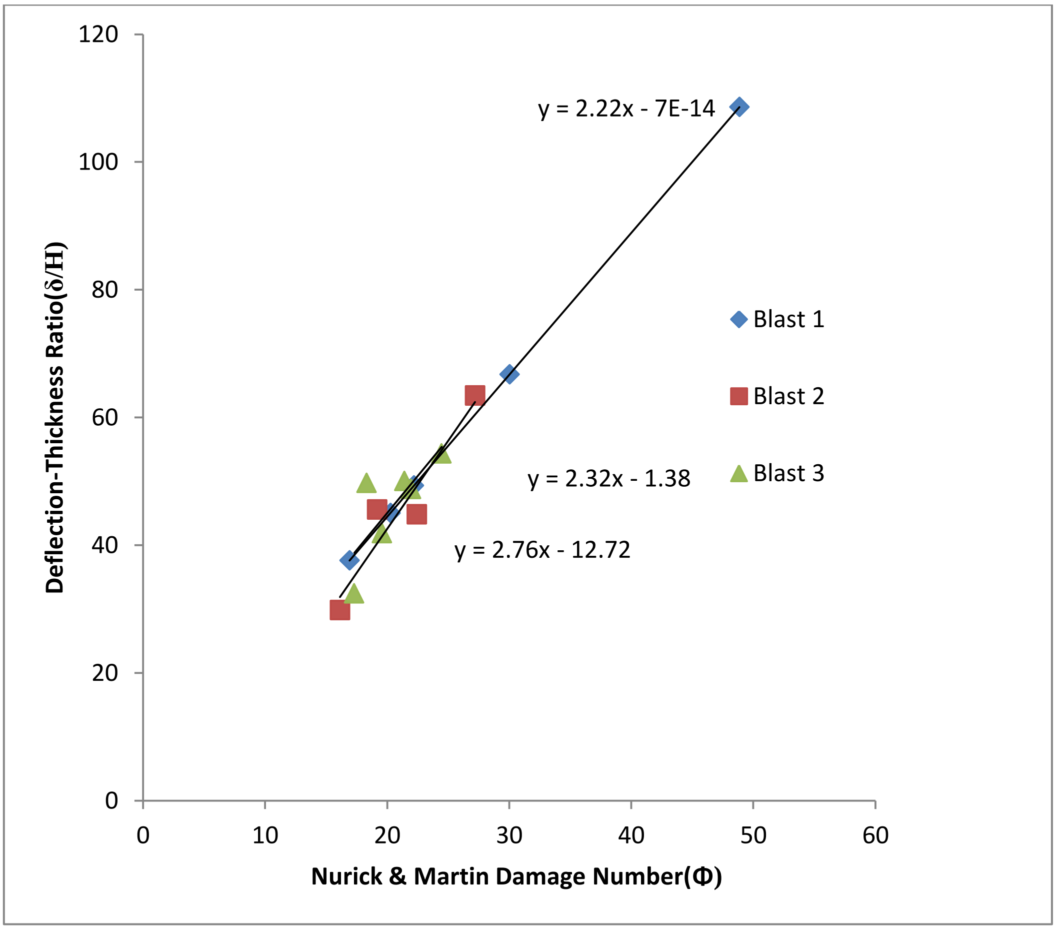

Figure 4.17: Nurick and Martin damage number (Φ) vs Deflection-thickness ratio (δ/H) for repeated blast loading of localised blast loaded plates.

CHAPTER 5

5 Material Characterisation Results and Discussion

This section evaluates the microstructural evidence of the deformed material after blast loading. It presents plates that have undergone uniform loading with a maximum charge of 30 g, with two different loading paths. In addition, plates that underwent localised loading, with different charge masses, were also investigated.

5.1 Microstructural characterisation for the uniformly blast loaded deformed material

An optical microscopy technique was used to track the microstructural changes that occurred as a result of uniform blast loading. All the specimens for microstructure analysis were prepared using the same method, as described in the experimental procedure (Chapter 3). The plate that was subjected to one blast of 30 g, referred to as D34P4M30B1, was compared to the plate that was subjected to three blasts of 10 g, referred to as D34P3M10B3. This is depicted in Figure 5.1. The former plate experienced a higher strain rate of deformation, while the latter plate experienced the same overall charge mass, with a lower strain path. The difference in the failure modes can be observed in Figures 4.1 - 4.3 (Chapter 4), where the macroscopic differences are described.

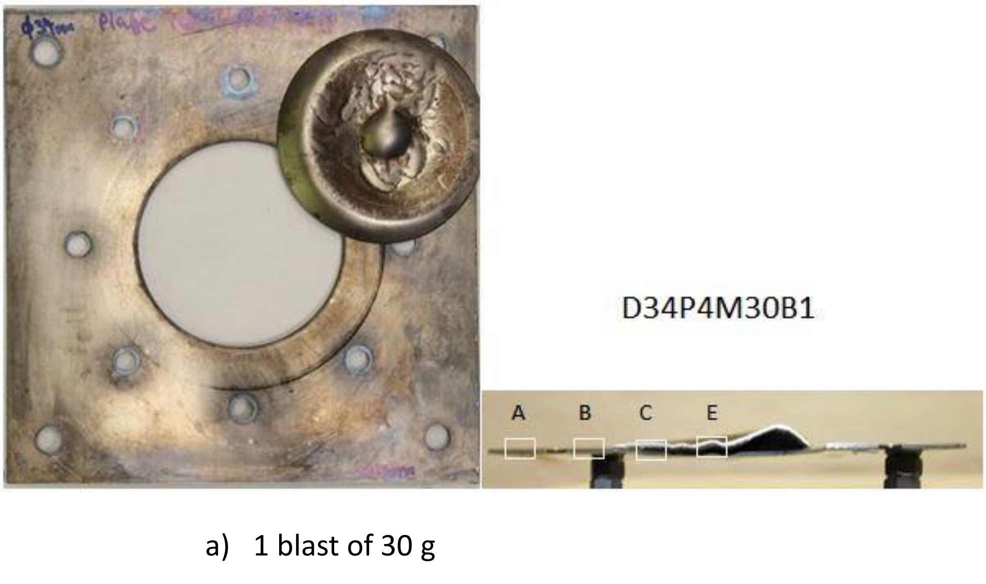

a) 1 blast of 30 g

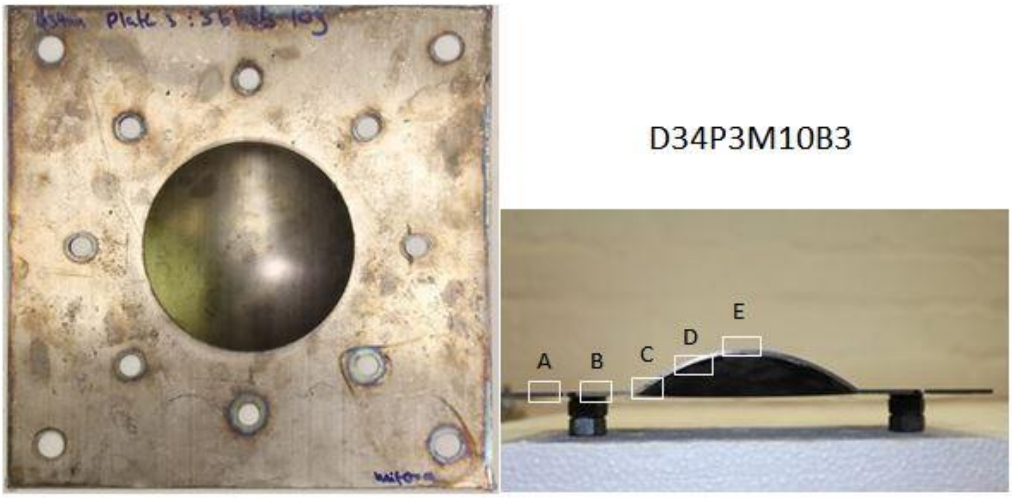

b) 3 blasts of 10 g.

Figure 5.1: Photographs of plates uniformly loaded

5.1.1 Microstructures of Clamped regions of plate D34P4M30B1 (one blast of 30 g)

Positions A and B

Positions A and B were typically undeformed, as this was within the clamped area of the plate. In positions A and B of the D34P3M30B1 (1 blast of 30 g) plate (*See* Figure 5.2) there was no expectation of intense microstructural changes. Figure 5.2 presents the light microscopy results for the Plate D34P4M30B1 (1 blast of 30 g), with the microstructures of position A and B consisting of a long, flat and homogenous grain network, similar to that of the microstructure of the as-received plate (*see* Figure 3.1).

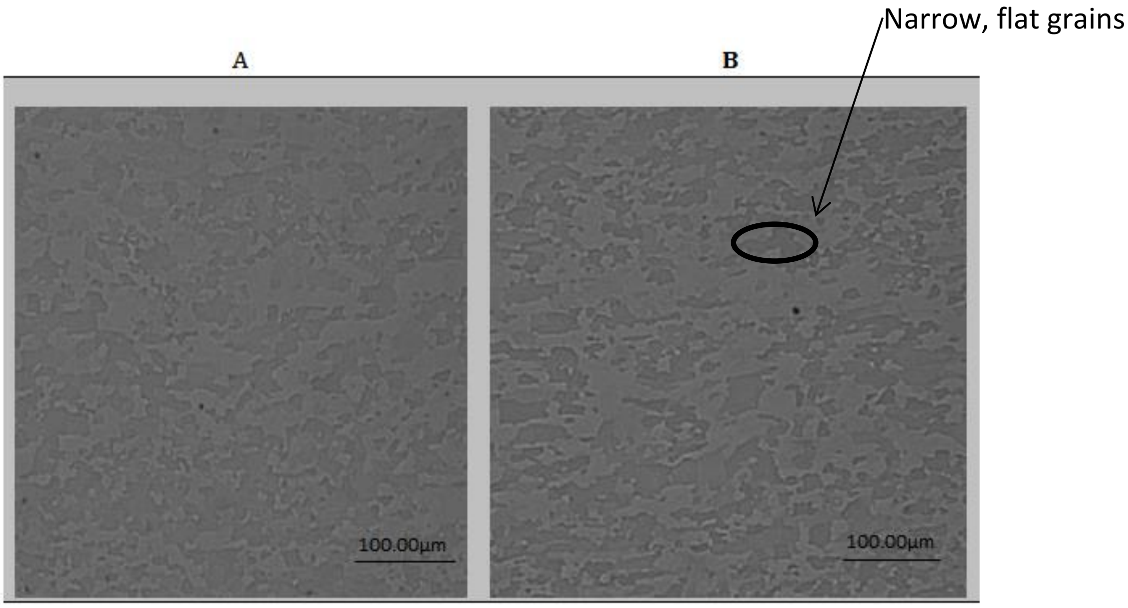

Figure 5.2: Micrographs of sections of clamped section of plates (30 g and 1 blast).

It was observed that there was no distinct difference between the optical microstructures of point A and B in the plate. Heat treatment, followed by a slow cool, was performed to ensure full transformation into a fully ferritic phase. Therefore, the material had no evidence of any other metastable phases after the heat treatment. Only BCC structure was observed in the specimen when examined using the EBSD analysis. Furthermore, the electron backscatter diffraction (EBSD) technique was used to emphasise the microstructural features, such as the observed grain morphology and the amounts of strain. However, because positions A and B were similar in grain structure and presentation, only one undeformed position was presented. Figure 5.3 includes an IPF map and strain map of position A. Position A for all the specimens, both in the uniform and localised loading conditions, had grains in different colours, meaning that these were in different orientations. Strain maps for position A represented low amounts of strain in this position, the green colour representing low strain, and only green was observed in position A.

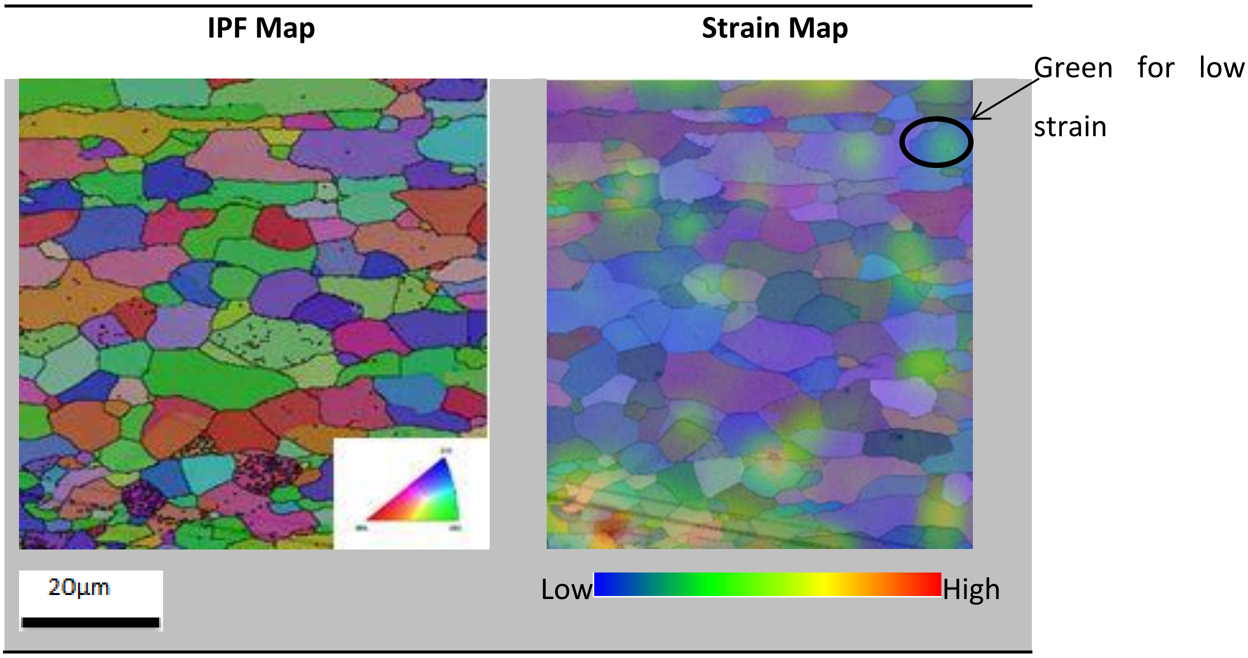

Figure 5.3: EBSD maps (IPF and Strain) for clamped section of plates (position A).

To provide further evidence of low strain in this position, the Vmap programme was used to analyse the data and generate microstructural information in the form of average grain sizes, calculated by measuring the Equivalent Circle Diameters (ECD) from each EBSD map. An average ECD from ten representative EBSD maps was generated by a random spread of grains for each sample. . The aspect ratio of the grains that were undeformed at position A (*see* Figure 5.4) started off with a grain aspect ratio of approximately 1 and those that had a higher aspect ratio were assumed to be grains that had undergone grain growth during heat treatment, but that still retained some of the nature of the rolled structure of the parent grains in the TD plane.

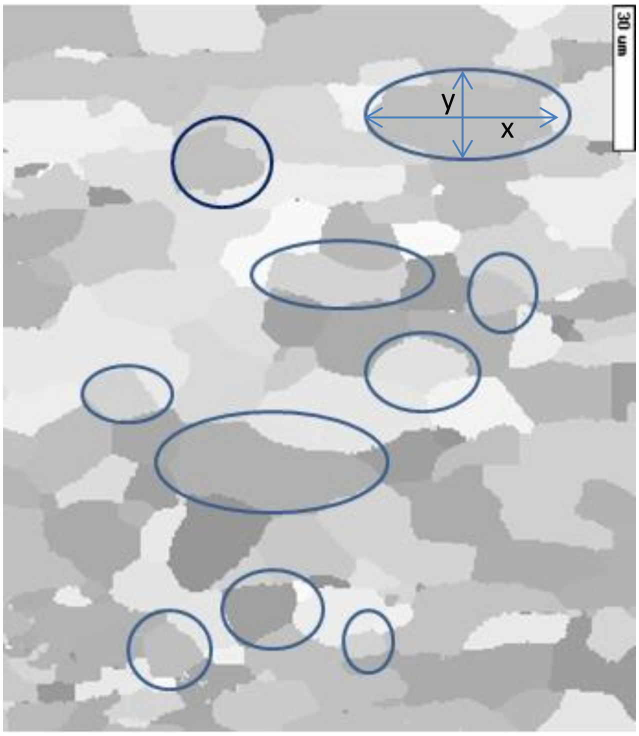

Position A Parameter	Aspect Ratio (x:y)
	1.94
	1.29
	1.89
	1.33
	2.67
	1
	0.89
	1
	1
	1.07
Mean	1.408
SD	0.548

Figure 5.4: ECDs and calculated aspect ratios for clamped section of plate (position A).

In summary, the microstructures in positions A and B had similar microstructural features, grain morphology and orientation. There was no effect of exposure to direct blast loading in these areas, owing to these positions being in the clamped areas. The microstructures had a grain structure similar to the starting material and represented the undeformed state of the material (*see* Figure 3.1).

5.1.2 Microstructural results of the boundary and central regions of the plate D34P3M30B1 (one blast of 30 g)

Positions C and E

Position C of the blast loaded plate, where one blast of 30 g had been used, was cut from the cap that was ruptured from the plate. This plate had no position D because of the immediate capping mode that occurred in this plate. However, the central part of the torn cap was regarded as position E of the plate.

In this plate, the microstructures in positions C exhibited long, flat grains. There were areas observed that had localised clusters of recrystallised grains, as displayed in Figure 5.5 and 5.6. These recrystallised grains were the result of high strain effects in a short amount of time, owing to repeated blast loading, and demonstrated adiabatic shear banding. Furthermore, position C displayed a large number of recrystallised regions, owing to adiabatic heating and the temperature effects experienced by the part of the plate (Smith and Nurick [110] and Ahmad [111]). Position E displayed a deformation microstructure of long flat grains. The number of recrystallised grains in E was smaller than in C, indicating a lower degree of adiabatic heating. There was a large amount of deformation, which was evidenced by the cap formation (Mode II).

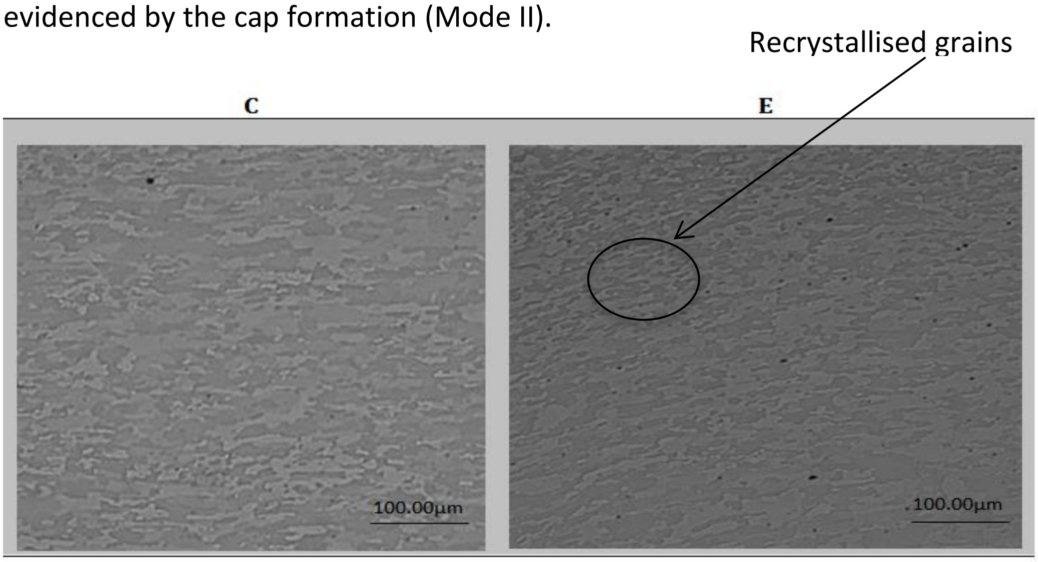

Figure 5.5: Optical micrographs for positions C and E for the plate subjected to one blast of 30 g.

Figure 5.6 indicates an increasing amount of deformation from positions C to E of the plate. As the grains became more deformed, the 111 direction plane became the preferred orientation (seen by the dominant colour, blue, relating to the key in the IPF maps). It was evident that the 111 direction, parallel to the blast direction, was favoured, owing to an increase in the amounts of deformation. Furthermore, the amounts of strain increased from position C to position E. This is indicated by the colour red in the strain maps, which represents high strain intensity, as is seen in Figure 5.6.

The distribution of the strain did not follow the typical dome formation, as the blast front would have been disrupted the moment the cap fractured from the plate. High strain rate deformation and associated localised adiabatic heating appeared to have caused the nucleation of a number of recrystallised grains, as is indicated by the arrows in positions C and E in Figure 5.5. The dotted line for position C in Figure 5.6 shows what could be described as a shear band. However, the high strain rates associated with the plate that underwent one blast of 30 g might not have allowed sufficient time for a more distinctly-formed shear band. In emphasis only one phase was observed. Consequently, the grain morphology was explained according to what was observed.

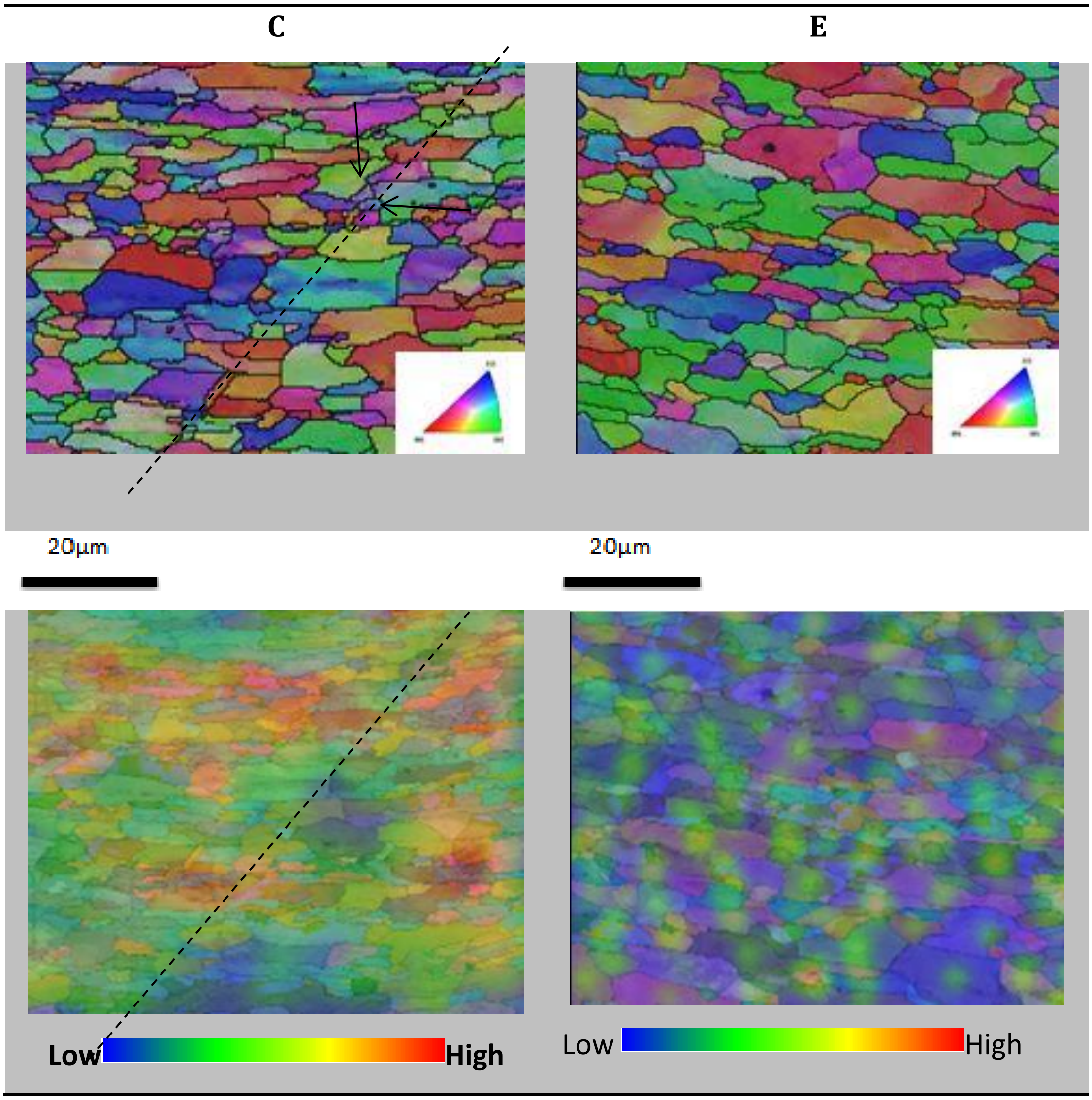

Figure 5.6: EBSD maps (IPF and Strain) for boundary and central regions (position C and E).

The Vmap results in Figure 5.7 show that, at these deformed positions C and E of the plate, the aspect ratio increased to more than 1 and the deformation was in the X direction, which was the direction perpendicular to the blast direction. This result was as expected. Only one phase, namely ferrite, was observed using microstructural and EBSD phase analysis.

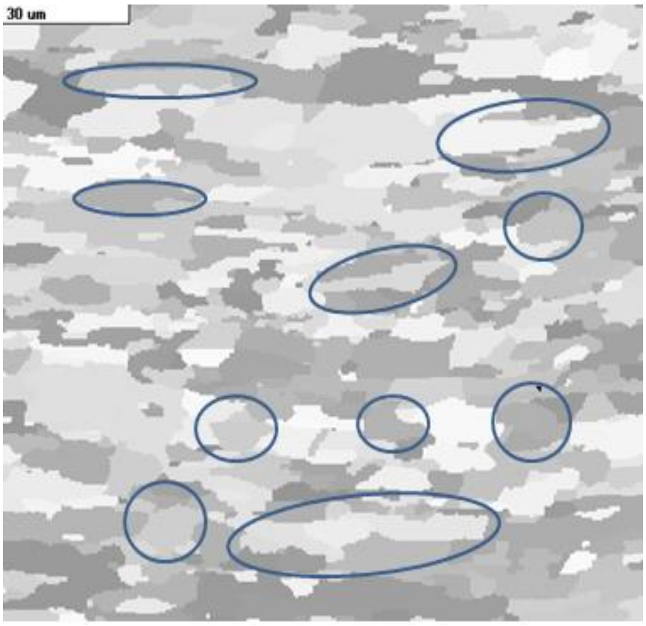

Position C Parameter	Aspect Ratio (x:y) 4C
	4
	4.5
	6.16
	3
	7.5
	10.6
	3
	0.67
	1.75
	1.67
Mean	4.285
SD	2.88

a)Position C

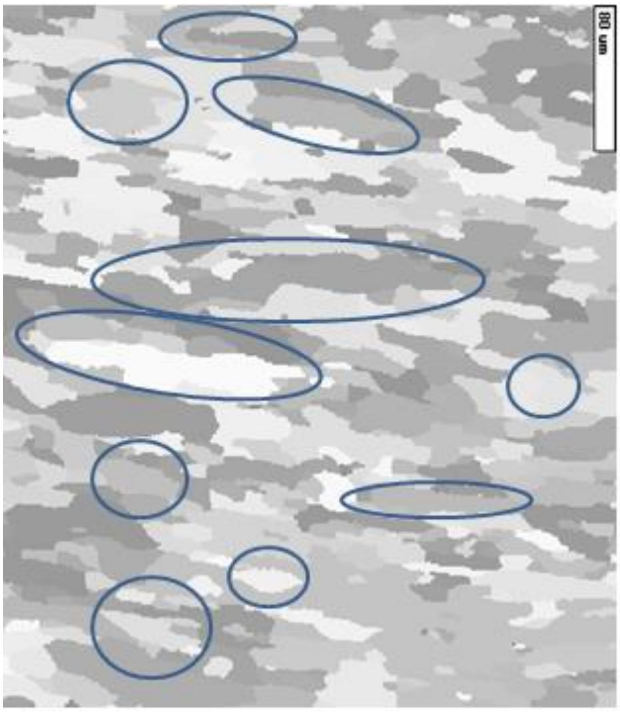

Position E Parameter	Aspect Ratio(x:y) 4E
	5
	4
	9
	11.17
	5
	1.3
	2.6
	7
	3.4
	2.2
Mean	5.067

b) Position E

Figure 5.7: ECDs for boundary and central regions of plate (Positions C and E).

In addition, evidence of brittle fracture was determined by a fractographic analysis of the surfaces of the sample in the SEM. The fractured plate had a rough surface with no obvious dimples, which was typical of the brittle failure mode being dominant because of high strain rates. Figure 5.9 displays the fractographs of the brittle surface.

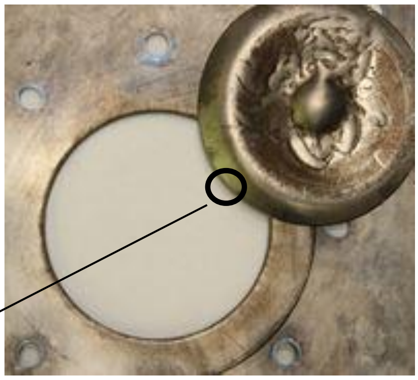

a)Plate with ruptured cap

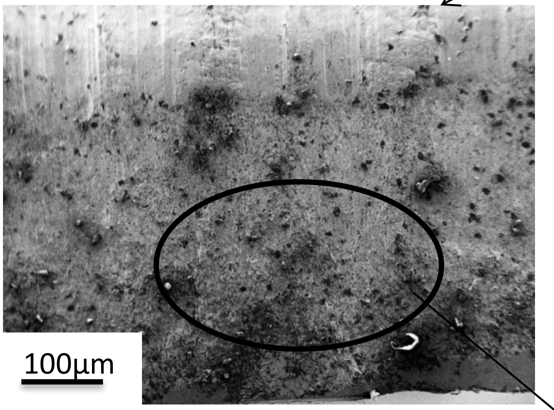

b) Fractograph of fracture surface of ruptured cap

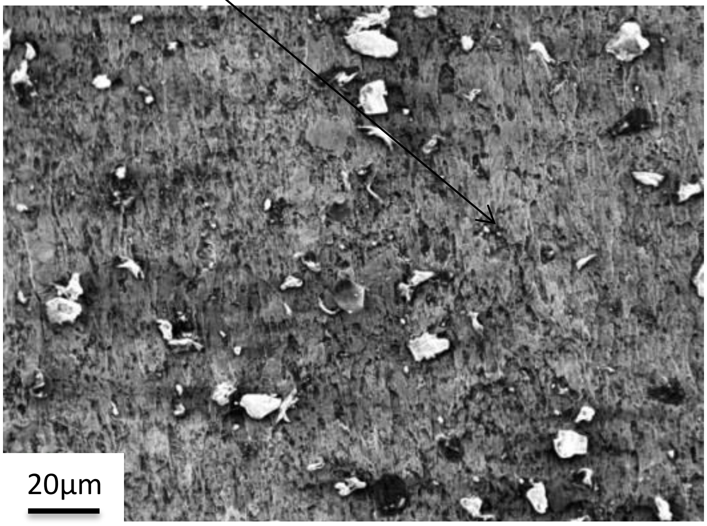

c)High magnification image with no dimples

Figure 5.8: Fractograph of failure at the boundary of plate subjected to 1 blast of 30 g.

Summary

Using a charge mass of 30 g and a single blast load, the plate was immediately ruptured. The optical microscopy results displayed grains that were long and flat and very deformed in the cap positions of the plate (Positions C and E). This deformation was further emphasised by the strain maps, which displayed the amount of strain experienced by the positions. Maps created using the Vmap programme were used for grain size and aspect ratio calculation, using the ECD method. These results emphasised the changes in grain morphology through increased aspect ratios. The fractographic analysis revealed that the rupture had occurred as a result of the brittle failure modes that had been induced by the high strain rates associated with the single blast of the large 30 g charge mass.

5.1.3 Microstructural results of the boundary and central region of the plate D34P4M10B3 (three blasts of 10 g)

Positions C, D and E

In the plate subjected to three blasts of 10 g, the microstructures in positions C, D and E all exhibited deformed long and flat, yet similar-sized, grains throughout the region of exposure to the blast. Positions C, D and E were situated along the typical dome shape of the deformed plate, which had experienced more strain because of its direct exposure to the blast load. The microstructures of these sections of the plate were expected to have a variation in grain size, orientation and structure because of the large-scale plastic deformation that they had experienced. In particular, position E showed a proliferation of long, flat grains of different sizes, the result of the very high strains experienced in this region. The above grain morphology can be observed in Figure 5.9.

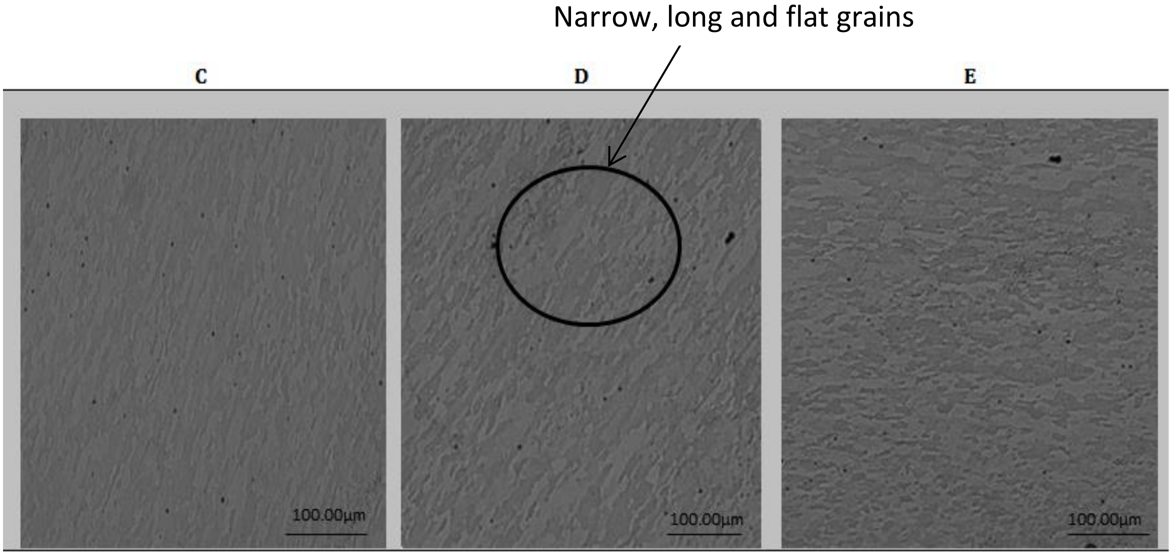

Figure 5.9: Optical Microscopy Results for Positions C, D and E.

Evidence of this observation was further emphasised by the EBSD maps. It was clearly observed in the IPF maps of Figure 5.10 that the colours that were favoured were blue and red, both representing orientation change. The 001 or 111 planes were parallel to the blast direction and the grain colour became red for the 001 plane and blue for the 111 plane. The grain shape was elongated and flat, representative of deformation. The strain maps showed evidence of increasing strain. The red became intensified in the deformed positions D and E, where larger strains had been experienced.

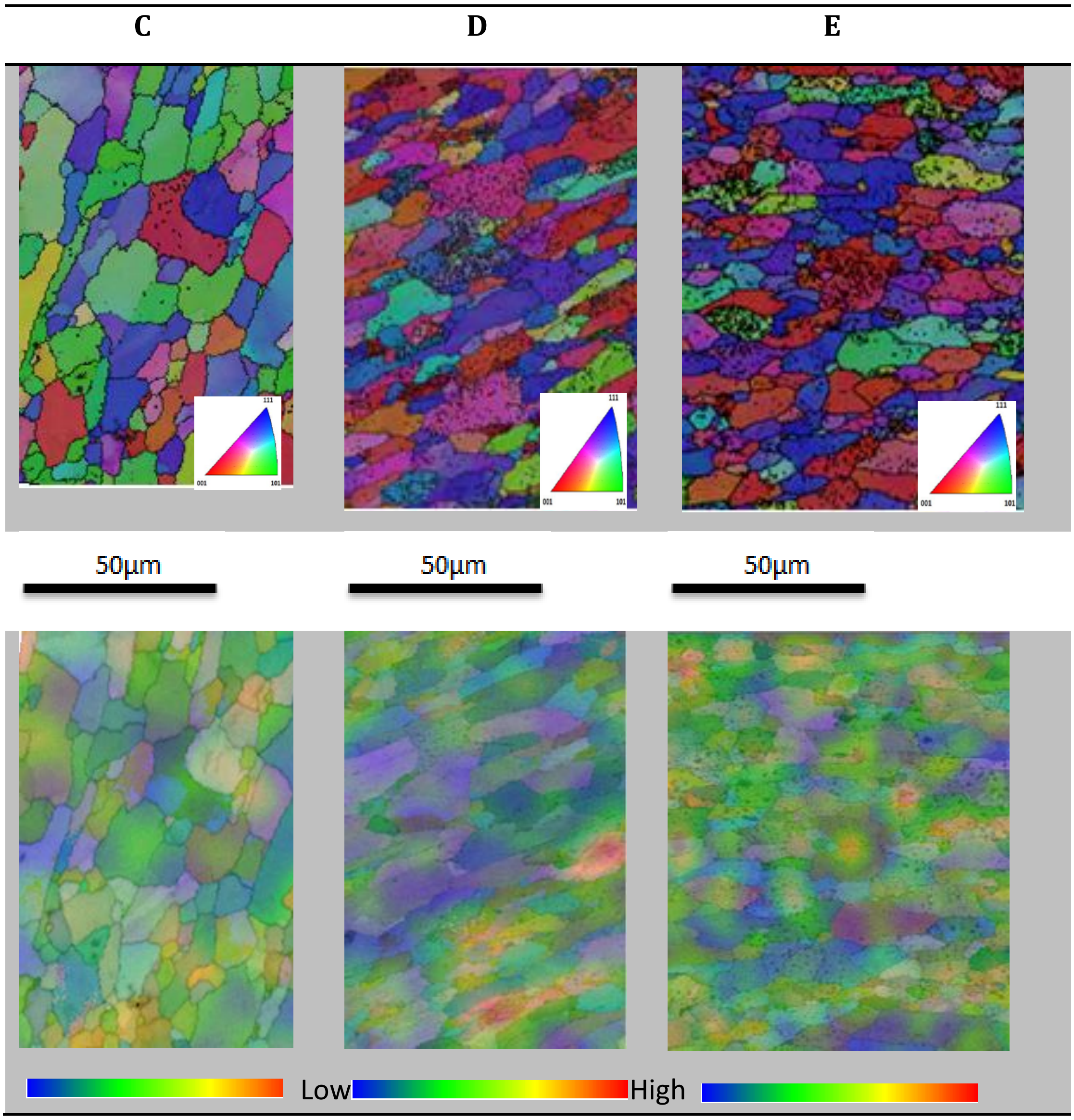

Figure 5.10: EBSD maps (IPF and Strain Maps) for boundary and central regions (Positions C, D and E).

Finally, the Vmap results displayed that, at these deformed positions (*see* Figure 5.11), the grain aspect ratio started to increase to more than 1 and the deformation was in the X direction, which was the direction perpendicular to the blast direction. Figure 5.11 provides a clear representation of these changes in aspect ratio.

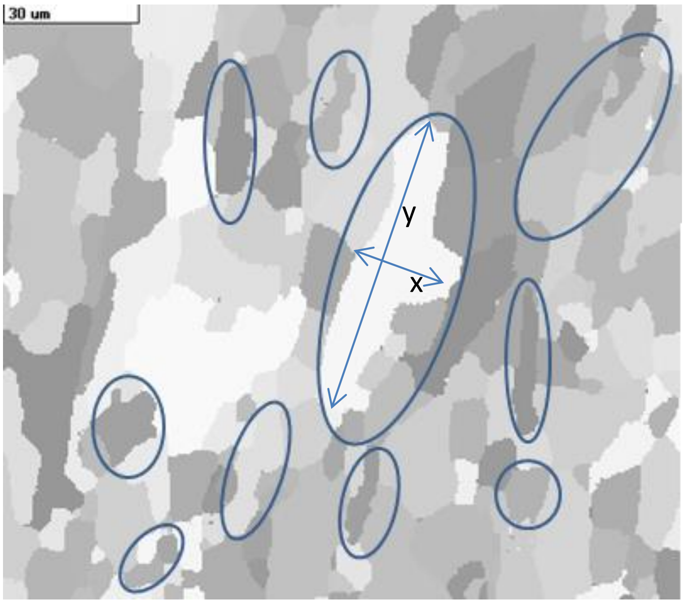

Position C

Position C Parameter	Aspect Ratio(x:y) 3C
	2.4
	3.5
	2.67
	1.88
	2
	5.63
	16
	6.75
	3.66
	3.71
Mean	4.82
SD	4.003

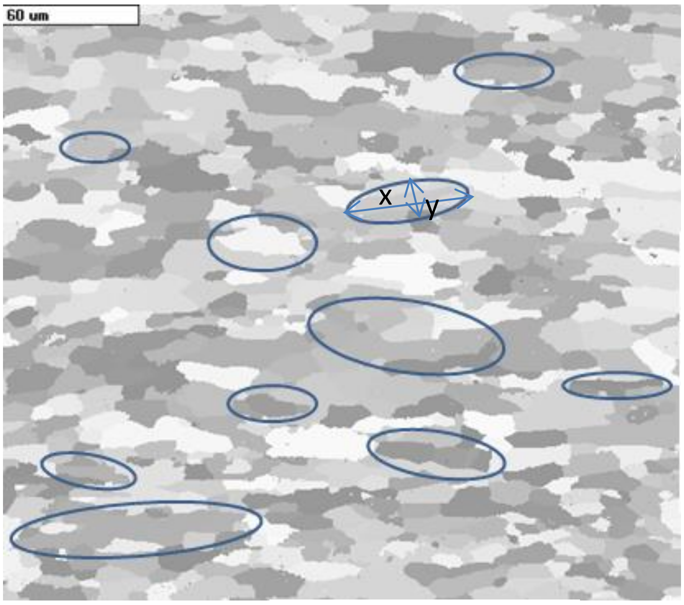

Position E

Position C Parameter	Aspect Ratio(x:y) 3E
	2.83
	5.25
	3
	7.4
	5.5
	6.5
	5.5
	10
	2.83
	2.83
Mean	5.164
SD	2.26

Figure 5.11: ECDs and calculated aspect ratios of Position C and E.

Summary

When a plate was exposed to repeated blast loads, using a 10 g charge mass, the macroscopic effects were in the form of a Mode II failure (*see* Chapter 4). The microstructural changes that occurred were typical of large-scale plastic deformation of the dome. There was an increase in the aspect ratio and the plastic deformation of the grains at the different positions, C to D and D to E. The grains became longer in size and flatter and the orientation also changed, as a result of the deformation caused by the blast load. In addition, the strain maps displayed increasing amounts of strain in areas that were in direct contact with the blast. The strain rates of multiple blasts of a smaller charge mass were obviously not sufficiently strong to result in brittle failure modes and, as a result, ductile deformation was dominant.

5.1.4 Comparisons of microstructural changes between the plate subjected to one blast of 30 g and the plate subjected to three blasts of 10 g

When the microstructures of the plate subjected to three blasts of 10 g were compared to the microstructures of the plate subjected to one blast of 30 g, both samples exhibited some evidence of plastic deformation in the dome area. Parts C and E of both of these plates had increased aspect ratios. However, in both cases, position A, regardless of the number of blasts or the size of the charge mass, exhibited no major microstructural changes, because the clamped sections of the plates did not experience plastic deformation.

The ECD calculation method was used to relate the strain and the aspect ratio of the grains. This relationship between the change in aspect ratio and the strain was verified by performing hardness tests that were related to the amount of plastic deformation and strain experienced in the key locations (positions C, D and E). The assumption followed was similar to that made by Smith *et al*. [11], whereby a theoretical method was required to relate the aspect ratio to the strain. The theoretical method assumed plane strain conditions. This assumption was valid for the plates in motion, where the motion was assumed to be in the transverse direction. As a result, the lateral motion would cause circumferential strains.

The microstructural study was performed by assuming that deformation was in the transverse direction only. The original heat-treated starting grain structure was considered to be equiaxed and homogenous. The shape of the average grains in the undeformed condition was observed to be square on all four sides, with an equal length of a_n. This is displayed in Figure 5.12 (Smith *et al.*, [112]).

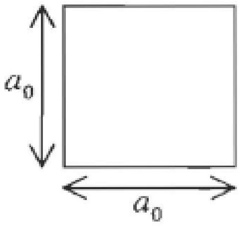

Figure 5.12: An illustration of an undeformed grain [112].

Exposing the material to blast loading caused the grains of the material to deform in order to accommodate the macroscopic shape change associated with plastic deformation. The grains elongated in the X direction (b_1) and decreased in height in the Y direction (a_1). This resulted in a change in the overall aspect ratio, which was calculated by a ratio of b_1: a_1. This is displayed below, in Figure 5.13.

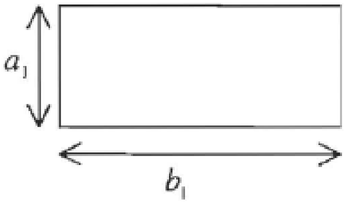

Figure 5.13: An illustration of the deformed grain [112].

In the torn plate that had been subjected to uniform loading (one blast of 30 g), the grains were longer in the X direction but, because of high strain rates, there was little plastic deformation. The cap rapture provided evidence of brittle fracture. The typical dome shape with its associated plastic deformation did not occur, because of the immediate rupturing of the cap, resulting in a disruption of the blast wave. There was evidence of plastic deformation at position E but less deformation was observed when this was compared to position C, which displayed long flat grains. (*See* Figure 5.5 and 5.7) In addition, the aspect ratios were calculated using the ECDs on the Vmap micrographs and it was observed that the aspect ratio difference decreased at position E, which meant that, overall, there had been limited plastic deformation, which corresponded with the brittle failure and lack of doming displayed by the macroscopic structure.

5.2 Microstructural characterisation of the localised blast loaded material

The metallographic study entailed a detailed investigation into the microstructural changes in a plate that had been subjected to two blasts of 6 g, referred to as D40P6MPB2, and in a plate subjected to two blasts of 5 g, referred to as D40P11M5B2. These two plates were subjected to the same number of blasts and are shown in Figure 5.14. The plate that had been exposed to two blasts of 6 g showed a petalling failure mode, while the plate that had been exposed to two blasts of 5 g showed an inelastic deformation failure (Mode II). The differences in the amount of plastic deformation were significant, given the small incremental increase in the charge mass.

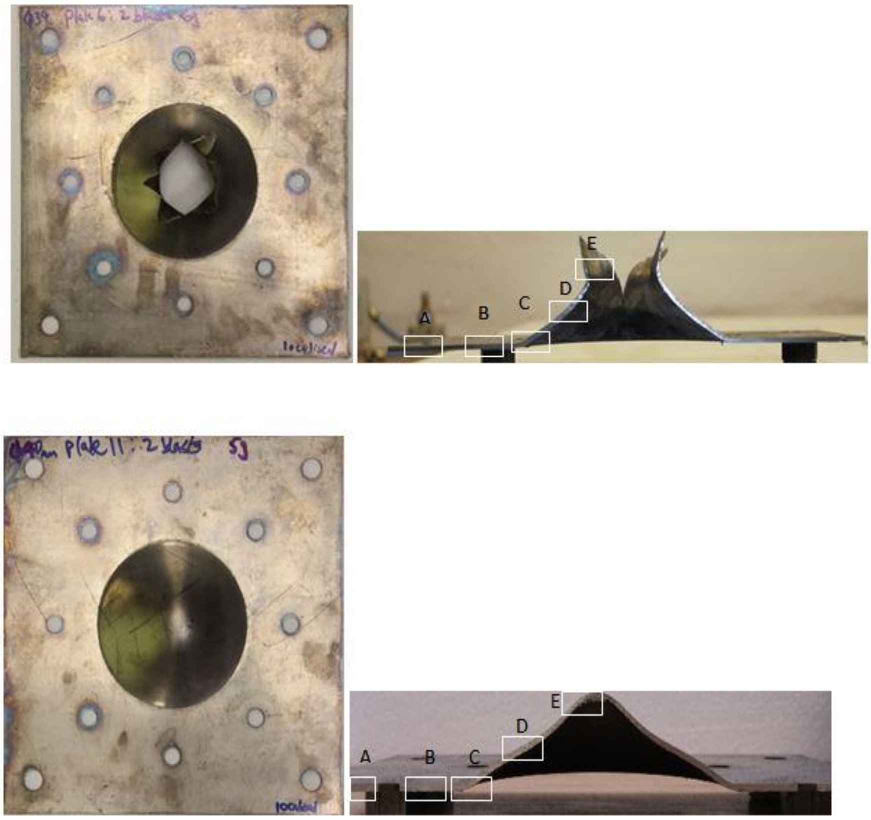

a)

b)

Figure 5.14: A comparison of the two plates: (a) two blasts of 6 g, and (b) two blasts of 5 g.

5.2.1 Microstructural results of boundary and central regions of plate D40P6M6B2 (two blasts of 6 g)

Positions C, D and E

Positions C, D and E all exhibited deformed grains of ferrite, which were elongated and, in low magnification, appeared homogenous [*see circle in* Figure 5.15(d)]. The elongation of the grains and the flat deformed shape, as observed in Figure 5.15, was due to plastic deformation during blast loading, which was the result of blast impulses. These positions experienced high strains through direct exposure to the blast loading effect. Repeated blast loading affected the grain size and grain morphology in the microstructure, producing elongated grains with a change in aspect ratio, when compared to the grains at the starting position (position A).

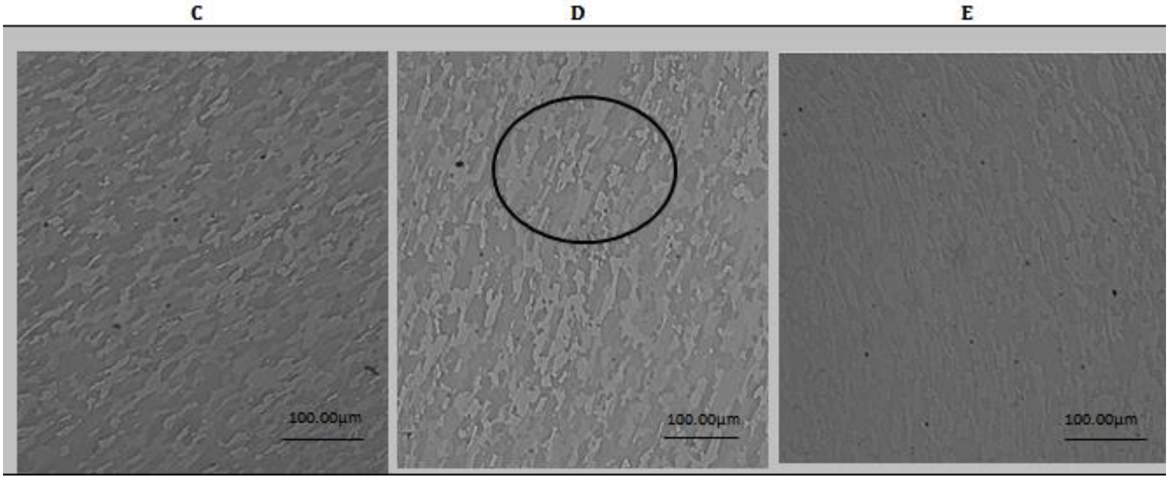

Figure 5.15: Optical Micrographs of C to E for plate subjected to two blasts of 6 g.

IPF maps in Figure 5.16 show that the grains became significantly more deformed, and the 111 direction plane became the preferred orientation. It was evident that the 111 direction, parallel to the blast direction, was favoured, with an increase in the amounts of deformation, as is seen when comparing C, D and E (*see* Figure 5.16). With an increase in the amount of deformation at position D, there was a corresponding increase in strain, with the strain maps showing an intensification of the red colour, indicating increasing strain. At position E, the strain had dissipated, owing to the petalling of the plate.

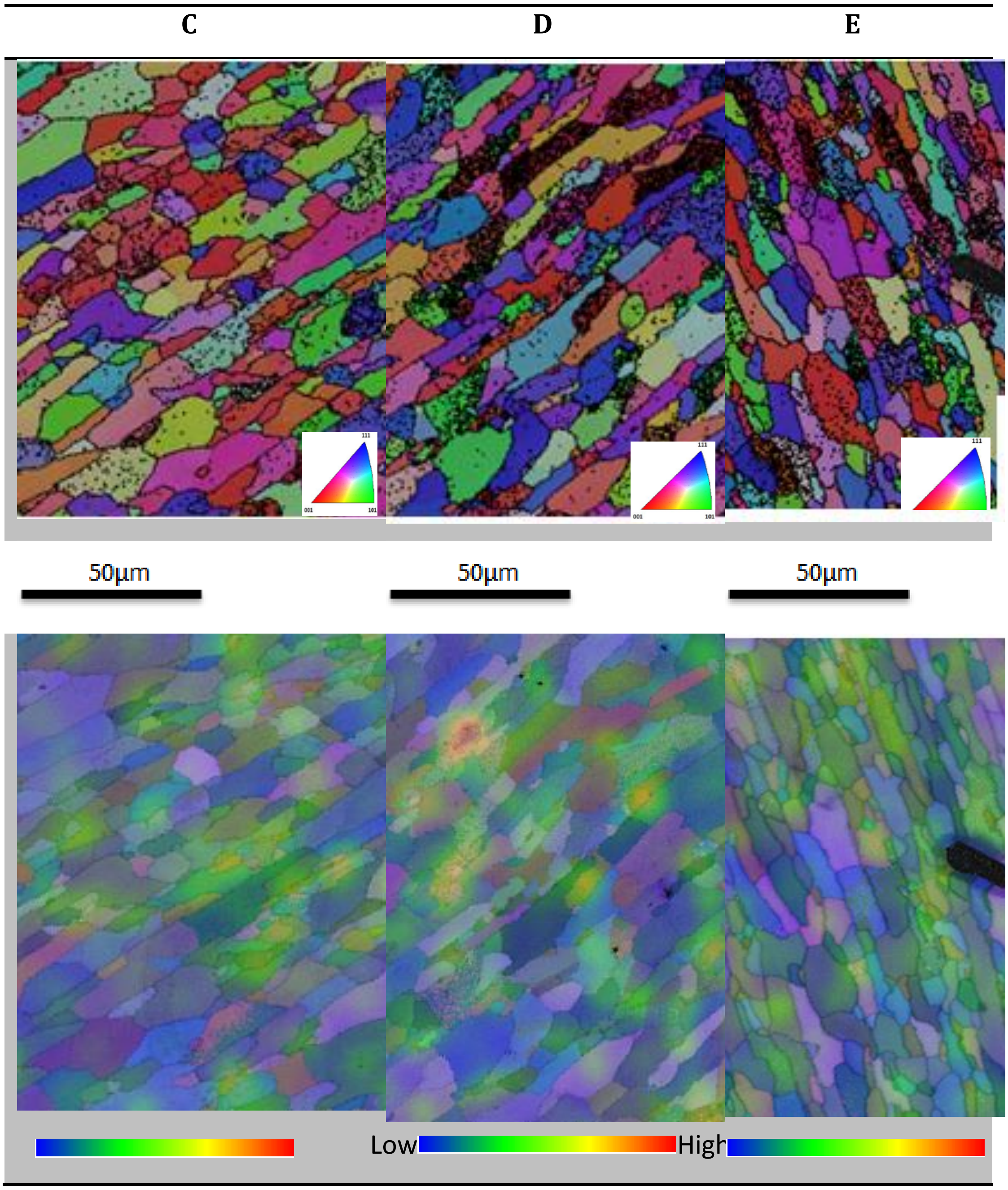

Figure 5.16: EBSD Maps (IPF and Strain) of C, D and E D40P6M6B2

(two blasts of 6 g)

The fracture surface of the petalling of this plate was analysed in the SEM in order to confirm whether the fracture surface exhibited ductile features. Ductile dimples were found on the fracture surface, confirming ductile failure mode. The plate had plastically deformed to a great extent before fracture. Figure 5.17

displays the fractographic investigation of the fracture surface. Figure 5.17 (c) shows distinct dimples, which are characteristic of a ductile failure mode.

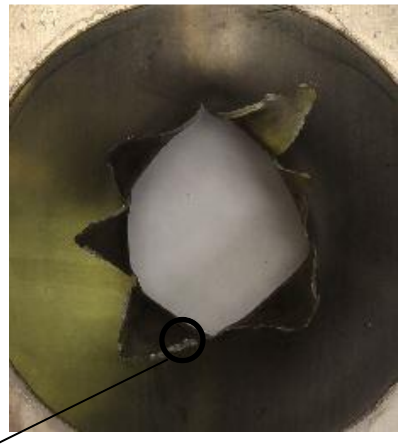

a) Plate showing petalling failure

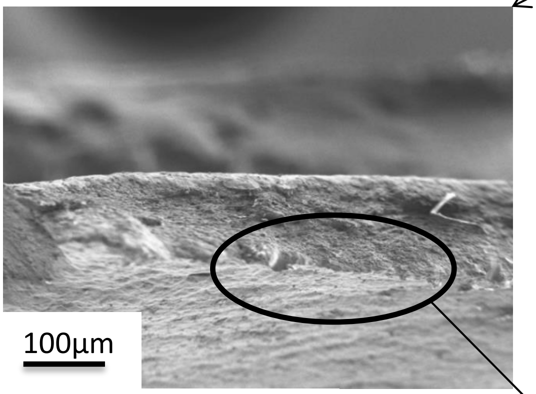

b) Low magnification SEM image of

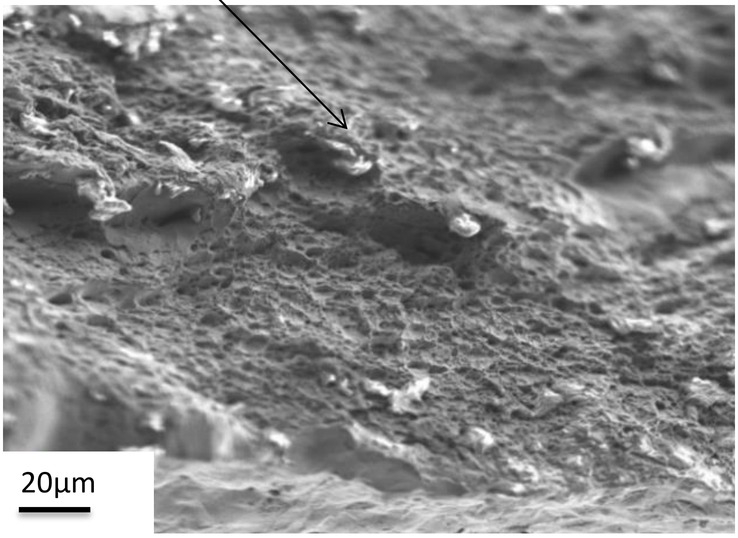

c) Dimpled fracture surface at a higher magnification

Figure 5.17: Fractograph of failure at the boundary of plate subjected to two blasts of 6 g

5.2.2 Microstructural results of boundary and central regions of plate D40P11M5B2 (two blasts of 5 g)

Positions C, D and E

The grain structure exhibited elongated grains (*see circle in* Figure 5.18) in the direction of the macroscopic plastic deformation of the dome. Position C, D and E were as displayed.

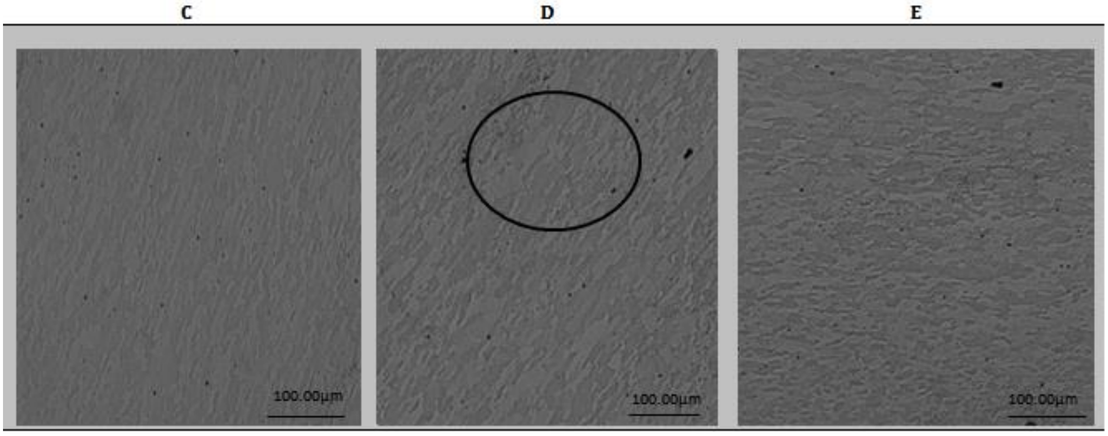

Figure 5.18: Optical Micrographs (C to E) of D40P11M5B2 (two blasts of 5 g).

The IPF orientation maps in Figure 5.19 show a proliferation of blue and red grains, which demonstrate that the 111 direction was favoured. The amount of deformation was observed to have increased from positions D to E.

The strain maps (*see* Figure 5.19) of positions C to E also show increasing amounts of strain, with significant strain intensity in positions D and E, both of which were directly exposed to the blast load. Evidence of grain morphology change was presented by increasing aspect ratios, calculated using the ECD approach. These values are displayed in the table of Vmap results (*see* Table 5.1).

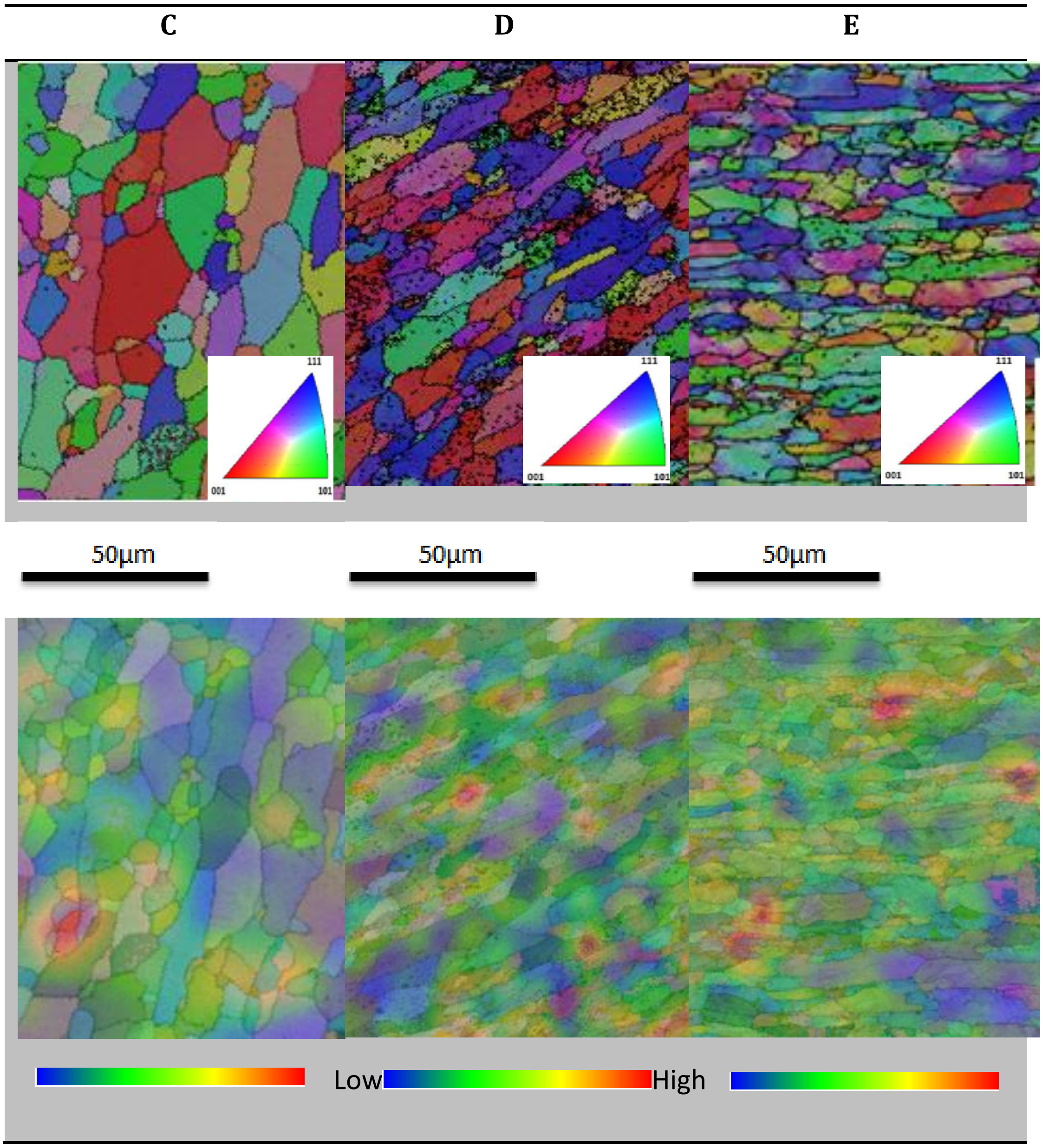

Figure 5.19: EBSD Maps (IPF and Strain) of D40P11M5B2 from C to E (two blasts of 5 g).

	Aspect ratio(x: y)			
	2 blasts of 6 g		2 blasts of 5 g	
Position Parameter	C	E	C	E
	2.07	4.67	5.75	6.25
	3	4.33	4.33	3
	3.5	3.14	3.57	6.33
	3.2	1.85	4.67	6.5
	3.4	4.4	3.6	4
	1.38	5	5.33	3.33
	1.82	3.33	3.67	3
	4.17	4.33	2	8
	3.5	4	2.57	2.67
	3	22	1.57	3.33
Mean	2.904	5.705	3.706	4.641
SD	0.82	5.50	1.301	1.82

Table 5.1: Aspect Ratio Changes for the ECDs of localised blast loaded plates

Summary

The optical microscopy results displayed grains that were long, flat and deformed in two positions of the plate (Positions C and E). The presence of this deformation was further established by the utilisation of IPF, strain and Vmaps. The calculation of the ECDs in the Vmap results confirmed a high amount of plastic deformation, as indicated by the increase in the aspect ratio.

5.2.3 Comparisons of Microstructural changes between Plate D40P6M6B2 (two blasts of 6 g) and Plate D40P11M5B2 (two blasts of 5 g)

Comparison of the grain structure of these plates showed an increase in the elongation of deformed grains, corresponding to the increase in charge mass. This was further verified by the Vmaps and EBSD maps, which provided information on the aspect ratio changes in the grain structure of each of the microstructures.

5.3 Evidence of Shear Banding

Evidence of adiabatic shear bands, caused by high localised temperature effects and strain rates, was found on the target plates. According to Hartley *et al.* [113], adiabatic shear bands were formed by a thermo-mechanical instability process and frequently accompanied the dynamic deformation of materials. Shear band formation generally required high strain rate deformation. Blast loading conditions had high strain rates, so it was to be expected that the sections of the plates that had experienced the most strain would exhibit shear banding.

Evidence of shear banding was identified in the uniformly blast loaded plate that had been subjected to a single blast load of 30 g, as seen in Chapter 5, Figure 5.6. Another plate that had been exposed to the localised loading condition was chosen to investigate the formation and existence of shear bands. Plate D40P6M6B2 (two blasts of 6 g), as observed in Figure 5.20, was investigated. Positions C and E were points of high strain. Therefore, the SEM analysis was performed for both the chosen areas. Clear evidence of adiabatic shear bands and material damage, the result of void growth, was found on position C of the target plate.

Figure 5.20: Parts(C and E) for a plate exposed to two blasts of 6 g

The areas identified as adiabatic shear bands are characterised by the presence of small recrystallised grains, as shown in Figures 5.21 and 5.22.

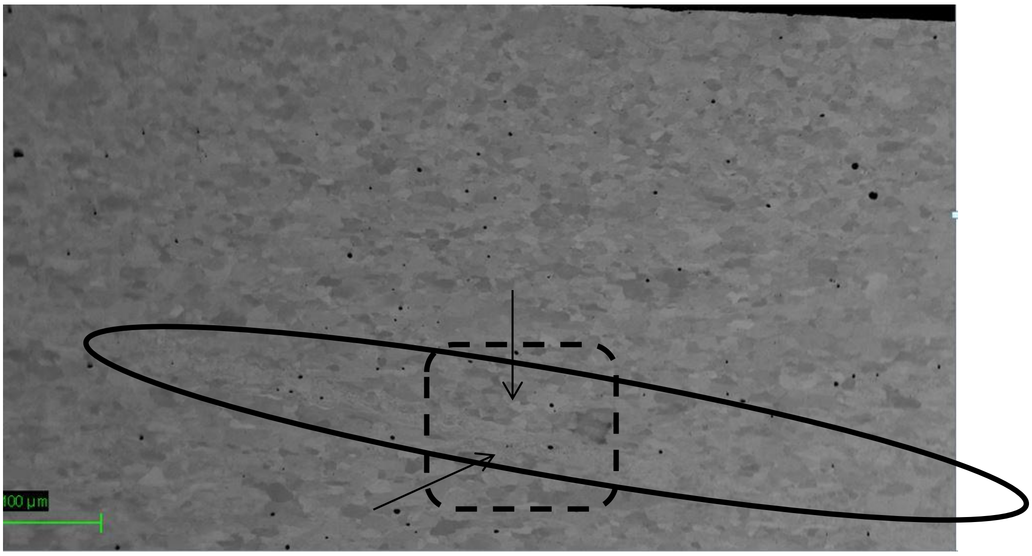

Figure 5.21: Shear banding in part C

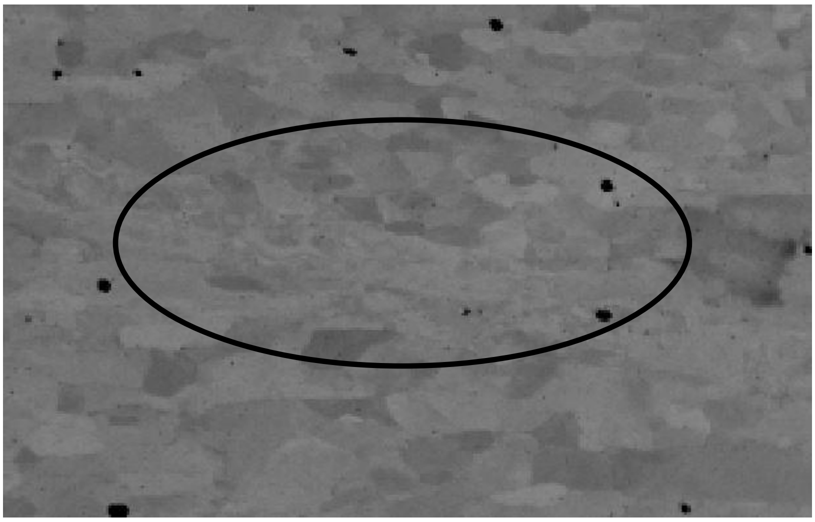

Figure 5.22: Higher magnification image of a Transformed Adiabatic Shear Band

Position E did not show any evidence of shear banding. This was because it had reached the stage of rupture. However, there was shear banding at position C, owing to high strain rates and high temperatures caused by a localised enhanced plastic deformation. When a shear band formed, the material strain increased and it became an average over both the highly strained shear band region and the area outside the shear band. The type of shear band that occurred in position C was a transformed shear band. A transformed shear band was formed as a result of the increased temperature effects on position C, which demonstrated a high zone of deformation. The change in the microstructure along the mid-thickness plane of the 2 mm-thick plate towards the shear zone is displayed in Figure 5.21. Inside the shear band zone (*see* circled part of Figure 5.22), a large amount of plastic deformation had occurred, leading to the onset of the recrystallisation process as a result of the localised increase in temperature in the shear band region. The recrystallised grains were new-strain free grains of small diameters, surrounded by distinct HAGBs. The transformed shear band inclined in the impact direction, similar to the theoretical slip-line field. According to Borvik *et al.* [117] a shear band propagating perpendicular to the impact direction can lead to fragmentation of the target plate. The stitched micrograph of the shear band is attached in Appendix D.

5.4 Relationship between Repeated Blast load and Strain Hardening

Martinez *et al*. [114] reported that strain hardening, strain rate sensitivity and temperature played very significant roles in the behaviour of a material when metals were subjected to impulsive blast loads. Strain hardening is defined as the resistance of a metal to plastic deformation. The higher the dislocation density of the material, the greater the resistance to plastic deformation. Callister and Rethwisch [35] noted that each strain increment strengthened and hardened the material, so that a larger stress was needed to further strain the metal. According to Askeland and Phulé [60], strain hardening enhanced strength and decreased the ductility of the metal as it was plastically deformed.

The ultimate tensile strength (UTS) of a metal was closely related to its hardness (HB), which was defined as a measure of the material's resistance to localised deformation (e.g., a small indent). Both of these mechanical properties were indicators of a metal's resistance to plastic deformation. Thus, the two mechanical properties were directly proportional to each other (Callister and Rethswich [35]). Eq. 5.1 relates tensile strength to hardness.

$$TS(MPA) = 3.45 \times HB \qquad \text{Eq. 5.1.}$$

In this section, the Vickers macro-hardness test results of the deformed plates are presented and discussed. The macro-hardness tests were performed at incremental distances of 10 mm apart on multiple plate profiles, depending on the number of blasts.

Hardness measurements were carried out on the Zwick Vickers hardness tester by applying a load of 10 kg for 10 seconds on the multiple plate profiles. The Vickers hardness measurements were taken on two consecutive positions with an average of two indents per location. Hardness A was the indentation point number one and Hardness B was indentation point number two. These indentation points were 10 mm away from each other. Tables 5.2 and 5.3 show the average hardness of each position of the plate and relate this hardness to the tensile strength of the material.

5.4.1 Vickers macro-hardness tests for the uniform loading condition

The images in Table 5.2 illustrate the HV value at each location, which describes the intensity of the deformation owing to a variety of charge masses and number of blasts in the uniform and localised loading conditions. Vickers hardness measurements along the profiles in the cross-sectional area of the plates are displayed in Table 5.2. From the summary of the results displayed in Table 5.2, it can be seen that there was a significant increase in hardness in the plate that had been subjected to one blast of 30 g, as compared to the plate that had been subjected to one blast of 10 g. The increase in the hardness in the former plate was due to the deformation in the grain structure and the intense dislocation multiplication, which was the result of the higher strain rates of the impulse of the blast load. The original hardness values of the undeformed as-received plate ranged from 170 - 172HV, which was much lower than the hardness values of the deformed plates across the deformed profile of the plates.

The positions of the plate that displayed a large increase in hardness were those that experienced high strain localised adiabatic heating because of exposure to the blast load. Therefore, for both plates there was an increase in hardness at positions C and E. For the plate that had been exposed to three blasts of 10 g there was a significant increase in hardness at position D. Position D of this plate showed high strain and deformed grains and this finding was reinforced by high aspect ratio values, calculated using the ECD approach. Therefore, from the observation of the microstructure in position D, it was noted that a high degree of deformation, indicated by high aspect ratios, caused the material to have high hardness values.

5.4.2 Vickers macro-hardness tests for the localised loading condition

The macroscopic images in Table 5.3 illustrate the comparison of the intensity of the deformation that resulted from a 1 g increase of charge mass with the same number of blasts in the localised loading condition. Vickers hardness measurements along the cross-sectional profiles of the plate showed deformed microstructures at positions C, D and E. These positions also showed an increase in the hardness values, with an increase in the amount of deformation. The plate exposed to two blasts of 6 g (as opposed to the plate exposed to two blasts of 5 g) displayed higher hardness values (*see* Table 5.3) on the deformed positions (positions C, D and E). The higher hardness was due to the effect of a 1 g incremental increase of charge, which gave higher impulses and which led to a more deformed microstructure with finer grains, as observed in Figure 5.18. A refined grain structure gave hardness values that were high, because of the grain boundary strengthening mechanism.

Photographs	Position	Aspect ratio values for C and E	Qualitative Strain value	HV approx.
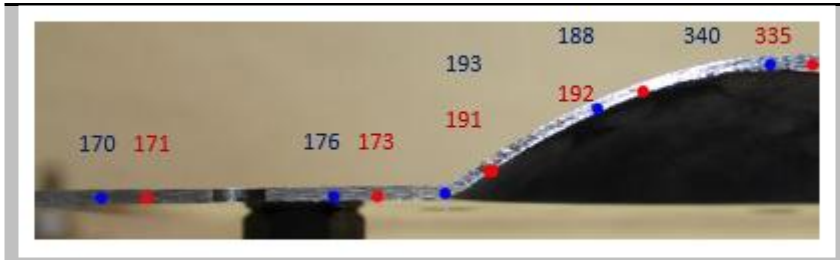	A		Low	170.5
	B		Low	174.5
	C	4.82	High	192
	D		Med	190
	E	5.164	High	337.5
	A		Low	172
	B		Low	171
	C	4.285	High	215.5
	E	5.067	High	269

Table 5.2: Summary of microstructural characteristics of mechanical properties for uniform loading.

Photographs	Position	Aspect ratio values for C and E	Qualitative Strain value	HV approx.
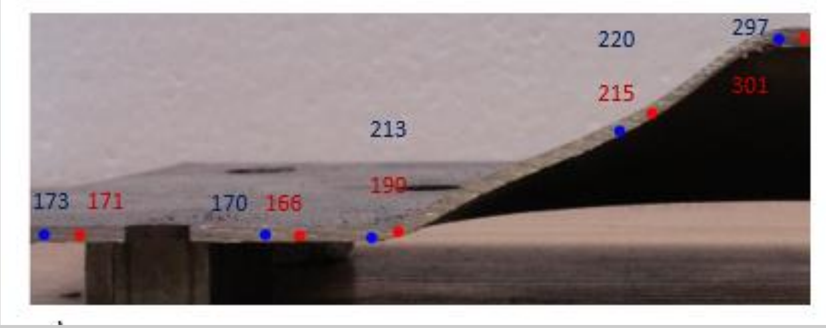	A		Low	172
	B		Low	168
	C	2.904	High	201.5
	D		High	217.5
	E	5.705	High	299
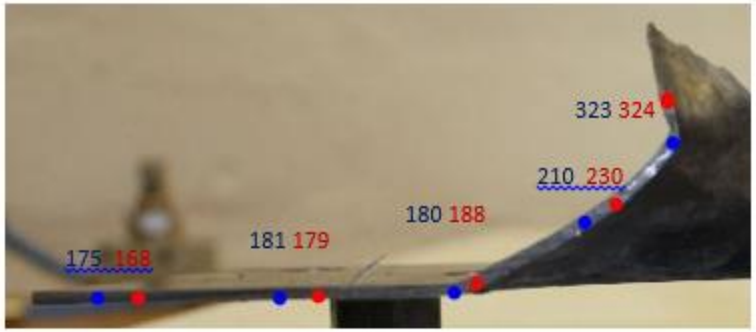	A		Low	178
	B		Low	173.5
	C	3.706	High	184
	D		High	220
	E	4.641	High	323.5

Table 5.3: Summary of microstructural characteristics of mechanical properties for localised loading

CHAPTER 6

6 Conclusions

The aim of this dissertation was to study the microstructural evolution that occurred in this material during plastic deformation as a result of blast loading. The 430 stainless steel was only one phase, owing to the prior heat treatment parameters. The experimental investigation included using uniform and blast loading conditions to create a deformation of the material and relating the macro response of the AISI 430 stainless steel plates to the microstructural changes that occurred. Therefore, the results were displayed and discussed using evidence of deformation in both the macrostructure and the microstructure. Based on those results the following conclusions were drawn:

6.1 Repeated blast loading of Annealed AISI 430 plates.

The impulse obtained from the repeated blast loading increased linearly, with an increase in charge mass for all plates, regardless of the loading condition. A similar linear trend was displayed by the midpoint deflection, which increased with an increase in impulse for all the plates. However, repeated blast loading was not suitable in situations where large, high strain rate impulses were experienced. But repeated blast loading did perform well where lower charge masses were used, both in uniform and localised loading conditions.

There was a correlation between the Jones damage number and the plates that were exposed to single blasts loads. But, when the number of blasts increased, there was a slight deviation. Nurick's damage number showed a similar relationship. The plates subjected to single blast loads displayed a good correlation to Nurick and Martin's modified dimensionless impulse. However, an increase in the number of blasts caused a larger deviation from the dimensionless impulse as the number of blast loads increased.

6.2 Microstructural changes in repeatedly uniformly loaded Plates

Uniformly loaded plates were exposed to the same overall charge mass with two different strain paths. The single blast of 30 g resulted in higher strain rate deformation in both microstructural and macroscopic features. The full separation of the cap in Position C confirmed that the failure was brittle in nature. The complete tearing failure result was due to the strain hardening exponent and the strain rate sensitivity of AISI 430 stainless steel. In addition, the plate exposed to one blast of 30 g demonstrated adiabatic heating and the occurrence of partial recrystrallisation in the microstructure of the plate. A number of early-stage shear bands could be identified in the IPF EBSD maps.

However, the plate exposed to the lower strain path when subjected to three blasts of 10 g resulted in large plastic deformation where there was a typical dome formation as a result of the repeated blasts. The extent of the deformation was greatest at position E and this was confirmed by the aspect ratio changes to the grains, measured using the ECD approach.

6.3 Microstructural changes in repeatedly localised loaded plates

The plate exposed to two blasts of 5 g resulted in the formation of a typical inner dome, superimposed by a global dome shape, associated with localised loading. In contrast, the plate exposed to two blasts of 6 g resulted in a petalling failure. The increase of 1 g per blast resulted in the localised plastic deformation and subsequent petalling of the 6 g plate. The fractography revealed that the petalling process was the result of ductile failure mechanisms and dimples were clearly visible on the fracture surface. The positions C and D for microstructures in both plates exhibited the same microstructural characteristics, both showing increases in the grain aspect ratio values.

CHAPTER 7

7 Recommendations

As a result of the findings and conclusions of this research work, the following recommendations were made:

- This study used only AISI 430 stainless steel, which is a single-phase metal. The material was heat treated and slowly cooled to ensure a fully ferritic single-phase structure. Going forward, the microstructural behaviour of two-phase materials when exposed to repeated blast loads should be investigated, using a combination of EBSD techniques and optical microscopy.

- Furthermore, there should be a study focussing on an investigation into the point of inflection and curvature of the deformed AISI 430 stainless steel plates.

- This study has shown that the strain rate sensitivity is an important property to consider when selecting a material for blast resistance. Therefore, future studies should include materials with a range of strain rate sensitivities.

- The changes observed, such as grain size change and shear band formations, follow the loading process that the structure was subjected to. In the present work, there was focus on the breakdown of deformation by metallurgical and imaging analysis. Fluctuations, such as pressure effects, and the type of explosive used in the vicinity loading were ignored. The study of those fluctuations should be the subject of a future work

- EBSD analysis on observed shear bands should be included in extended forthcoming studies.

8 References

[1] R. Sierakowski, "Strain rate behavior of metals and composites," in *Convegno IGF XIII Cassino 1997,* 2008, .

[2] N. NagarajaRao, M. Lohrmann and L. Tall, "Effect of strain rate on the yield stress of structural steel, ASTM Journal of Materials, Vol. 1, No. 1, March 1966, Publication No. 293," 1966.

[3] D. Roylance, "Stress-strain curves," *Massachusetts Institute of Technology Study, Cambridge,* 2001.

[4] J. M. Gere and B. J. Goodno, *Mechanics of Materials.* Nelson Education, 2012.

[5] S. Hecker, MG. Stout, KP. Staudhammer, JL Smith "Effects of strain state and strain rate on deformation-induced transformation in 304 stainless steel: Part I. Magnetic measurements and mechanical behavior," *Metallurgical Transactions A,* vol. 13, pp. 619-626, 1982.

[6] M. Hadianfard, R. Smerd, S. Winkler "Effects of strain rate on mechanical properties and failure mechanism of structural Al–Mg alloys," *Materials Science and Engineering: A,* vol. 492, pp. 283-292, 2008.

[7] E. Krempl and F. Khan, "Rate (time)-dependent deformation behavior: an overview of some properties of metals and solid polymers," *Int. J. Plast.,* vol. 19, pp. 1069-1095, 2003.

[8] H. Holzapfel, V. Schulze, V. Vohringer, O. Macherauch "Residual stress relaxation in an AISI 4140 steel due to quasistatic and cyclic loading at higher temperatures," *Materials Science and Engineering: A,* vol. 248, pp. 9-18, 1998.

[9] A. Tiamiyu *et al*, "Mechanical behavior and high-resolution EBSD investigation of the microstructural evolution in AISI 321 stainless steel under dynamic loading condition," *Materials Science and Engineering: A,* vol. 673, pp. 400-416, 2016.

[10] A. K. Singh, *Mechanics of Solids.* PHI Learning Pvt. Ltd., 2007.

[11] M. P. Smith, *Microstructural Analysis of Plates with Large Strains as a Result of Central Localised Blast loading,* 1999.

[12] D. Chichili, K. Ramesh and K. Hemker, "The high-strain rate response of alpha-titanium: experiments, deformation mechanisms and modeling," *Acta Materialia,* vol. 46, pp. 1025-1043, 1998.

[13] G. R. Johnson and W. H. Cook, "A constitutive model and data for metals subjected to large strains, high strain rates and high temperatures," in *Proceedings of the 7th International Symposium on Ballistics,* 1983, pp. 541-547.

[14] A. Odeshi, MN. Bassim, S. Al-Ameeri "Dynamic shear band propagation and failure in AISI 4340 steel," *J. Mater. Process. Technol.,* vol. 169, pp. 150-155, 2005.

[15] M. N. Bassim, "Study of the formation of adiabatic shear bands in steels," *J. Mater. Process. Technol.,* vol. 119, pp. 234-236, 2001.

[16] J. A. Zukas, T. Theodore, H.F Swift "Impact dynamics," *Journal of Applied Mechanics,* vol. 50, pp. 702, 1983.

[17] R. J. Clifton, "Response of materials under dynamic loading," *Int. J. Solids Structures,* vol. 37, pp. 105-113, 2000.

[18] H. Zhao and G. Gary, "A new method for the separation of waves. Application to the SHPB technique for an unlimited duration of measurement," *J. Mech. Phys. Solids,* vol. 45, pp. 1185-1202, 1997.

[19] National Research Council, *Blast Mitigation for Structures: 1999 Status Report on the DTRA/TSWG Program.* National Academies Press, 2000.

[20] J. Harris, "Dynamic testing under nonsinusoidal conditions and the consequences of nonlinearity for service performance," *Rubber Chemistry and Technology,* vol. 60, pp. 870-887, 1987.

[21] R. Clamroth, "Determination of viscoelastic properties by dynamic testing," *Polym. Test.,* vol. 2, pp. 263-286, 1981.

[22] M. Brünig and S. Gerke, "Simulation of damage evolution in ductile metals undergoing dynamic loading conditions," *Int. J. Plast.,* vol. 27, pp. 1598-1617, 2011.

[23] R. Harsoor and L. Ramachandra, "Influence of notch on the elastic–plastic response of clamped beams subjected to low velocity impact," *Int. J. Impact Eng.,* vol. 36, pp. 1058-1069, 2009.

[24] J. Liu and N. Jones, "Experimental investigation of clamped beams struck transversely by a mass," *Int. J. Impact Eng.,* vol. 6, pp. 303-335, 1987.

[25] K. Xia and W. Yao, "Dynamic rock tests using split Hopkinson (Kolsky) bar system–A review," *Journal of Rock Mechanics and Geotechnical Engineering,* vol. 7, pp. 27-59, 2015.

[26] Z. Zhang, F. Zhou and E. Lavernia, "On the analysis of grain size in bulk nanocrystalline materials via X-ray diffraction," *Metallurgical and Materials Transactions A,* vol. 34, pp. 1349-1355, 2003.

[27] Y. Shui-Sheng, L. Yu-Bin and C. Yong, "The strain rate effect of engineering materials and its unified model," *Latin American Journal of Solids and Structures,* vol. 10, pp. 833-844, 2013.

[28] V. Rojansky and W. Bleakney, *Double Ballistic Pendulum,* 1961.

[29] W. De Morais, S. Monteiro and J. d'Almeida, "Evaluation of repeated low energy impact damage in carbon–epoxy composite materials," *Composite Structures,* vol. 67, pp. 307-315, 2005.

[30] S. Rajasekaran, *Structural Dynamics of Earthquake Engineering: Theory and Application using MATHEMATICA and MATLAB.* Elsevier, 2009.

[31] M. Ramulu, A. Chakraborty and T. Sitharam, "Damage assessment of basaltic rock mass due to repeated blasting in a railway tunnelling project–A case study," *Tunnel. Underground Space Technol.,* vol. 24, pp. 208-221, 2009.

[32] N. Ranwaha and S. C. K. Yuen, "The effects of blast-induced fragments on cellular materials," *Int. J. Impact Eng.,* vol. 92, pp. 50-65, 2016.

[33] T. F. Henchie, S. Chung Kim Yuen, G.N. Ranwaha "The response of circular plates to repeated uniform blast loads: An experimental and numerical study," *Int. J. Impact Eng.,* vol. 74, pp. 36-45, 2014.

[34] N. Jacob, G. Nurick and G. Langdon, "The effect of stand-off distance on the failure of fully clamped circular mild steel plates subjected to blast loads," *Eng. Struct.,* vol. 29, pp. 2723-2736, 2007.

[35] W. D. Callister and D. G. Rethwisch, *Materials Science and Engineering: An Introduction.* Wiley New York, 2007.

[36] M. F. Ashby, H. Shercliff and D. Cebon, *Materials: Engineering, Science, Processing and Design.* Butterworth-Heinemann, 2013.

[37] H. Chandler, *Hardness Testing.* ASM international, 1999.

[38] X. Peng, J. Zhou, Y.F Wang "Effect of grain refinement on the resistance of 304 stainless steel to breakaway oxidation in wet air," *Acta Materialia,* vol. 53, pp. 5079-5088, 2005.

[39] Z. Peng, J. Gong and H. Miao, "On the description of indentation size effect in hardness testing for ceramics: Analysis of the nanoindentation data," *Journal of the European Ceramic Society,* vol. 24, pp. 2193-2201, 2004.

[40] M. Bassim and A. Odeshi, "Shear strain localisation and fracture in high strength structural materials," *Archives of Materials Science,* vol. 70, pp. 70, 2008.

[41] S. Boakye-Yiadom and M. N. Bassim, "Effect of prior heat treatment on the dynamic impact behavior of 4340 steel and formation of adiabatic shear bands," *Materials Science and Engineering: A,* vol. 528, pp. 8700-8708, 2011.

[42] Y. Xu, W.L Zhong , Y.J. Chen, L.T. Shen, Q. Liu, Y.L Bai and M.A Meyers "Shear localization and recrystallization in dynamic deformation of 8090 Al–Li alloy," *Materials Science and Engineering: A,* vol. 299, pp. 287-295, 2001.

[43] S. Timothy, "The structure of adiabatic shear bands in metals: a critical review," *Acta Metallurgica,* vol. 35, pp. 301-306, 1987.

[44] G. Pouget and A. P. Reynolds, "Residual stress and microstructure effects on fatigue crack growth in AA2050 friction stir welds," *Int. J. Fatigue,* vol. 30, pp. 463-472, 2008.

[45] L. Murr, E.A Trillo, S. Pappu and C. Kennedy "Adiabatic shear bands and examples of their role in severe plastic deformation," *J. Mater. Sci.,* vol. 37, pp. 3337-3360, 2002.

[46] Q. Xue, E. Cerreta and G. Gray, "Microstructural characteristics of post-shear localization in cold-rolled 316L stainless steel," *Acta Materialia,* vol. 55, pp. 691-704, 2007.

[47] M. Perez-Prado, J. Hines and K. Vecchio, "Microstructural evolution in adiabatic shear bands in Ta and Ta–W alloys," *Acta Materialia,* vol. 49, pp. 2905-2917, 2001.

[48] F. Humphreys, "Characterisation of fine-scale microstructures by electron backscatter diffraction (EBSD)," *Scr. Mater.,* vol. 51, pp. 771-776, 2004.

[49] K. Ushioda, S. Nakanishi, T. Morikawa ,K. Higashida, Y. Suwa and M. Kenichi"Evolution of heterogeneous deformation structure and recrystallization texture of steel," in *Materials Science Forum,* 2013, pp. 58-65.

[50] A. Rollett, F.J Humphreys, G.S Rohrer and M. Hatherly *Recrystallization and Related Annealing Phenomena.* Elsevier, 2004.

[51] N. Hansen and D. J. Jensen, "Development of microstructure in FCC metals during cold work," *Philosophical Transactions of the Royal Society of London A: Mathematical, Physical and Engineering Sciences,* vol. 357, pp. 1447-1469, 1999.

[52] I. Dillamore and H. Katoh, "The mechanisms of recrystallization in cubic metals with particular reference to their orientation-dependence," *Metal Science,* vol. 8, pp. 73-83, 1974.

[53] Y. Chao and S. Varma, "Effect of strain rate on dislocation cell size and Hall-Petch type relationship at various strain levels during a uniaxial tensile test in VP nickel," *Scripta Metallurgica Et Materialia,* vol. 24, pp. 1665-1668, 1990.

[54] H. G. Wilsdorf and D. Kuhlmann-Wilsdorf, "Work softening and Hall-Petch hardening in extruded mechanically alloyed alloys," *Materials Science and Engineering: A,* vol. 164, pp. 1-14, 1993.

[55] S. Firstov, T. Rogul and O. Shut, "Critical grain sizes and generalized flow stress-grain size dependence," *ArXiv Preprint arXiv:1304.7865,* 2013.

[56] S. Firstov, T. Rogul and S. Dub, "Grain boundary engineering of nanostructured chromium films," in *Innovative Superhard Materials and Sustainable Coatings for Advanced Manufacturing*Anonymous Springer, 2005, pp. 225-232.

[57] R. Masumura, P. Hazzledine and C. Pande, "Yield stress of fine grained materials," *Acta Materialia,* vol. 46, pp. 4527-4534, 1998.

[58] V. Cain, *High Temperature Creep Behaviour Niobium Bearing Ferritic Stainless Steels,* 2005.

[59] N. E. Dowling, *Mechanical Behavior of Materials: Engineering Methods for Deformation, Fracture, and Fatigue.* Prentice hall, 1993.

[60] D. R. Askeland and P. P. Phulé, "The science and engineering of materials," 2003.

[61] R. N. Anderson, *Materials Science.* Wiley Online Library, 1974.

[62] W. Hall, "Introduction to Materials Science & Engineering," 1976.

[63] H. Shin, J. An, S.H Park and D.N Lee "The effect of texture on ridging of ferritic stainless steel," *Acta Materialia,* vol. 51, pp. 4693-4706, 2003.

[64] D. N. Lee, "Asymmetric rolling as means of texture and ridging control and grain refinement of aluminum alloy and steel sheets," in *Materials Science Forum,* 2004, pp. 1-6.

[65] G. F. Kinney and K. J. Graham, *Explosive Shocks in Air.* Springer Science & Business Media, 2013.

[66] W. Davis, J. Zukas and W. Walters, "Explosive effects and applications," *Introduction to Explosives,* 1998.

[67] W. Baker, "Explosions in Air University of Texas Press," *Austin and London,* 1973.

[68] T. Ngo, P. Mendis, A. Gupta and J. Ramsay "Blast loading and blast effects on structures–an overview," *Electronic Journal of Structural Engineering,* vol. 7, pp. 76-91, 2007.

[69] Federal Emergency Management Agency, *Risk Management Series: Reference Manual-to Mitigate Potential Terrorist Attacks Against Buildings.* Government Printing Office, 2003.

[70] R. Rajendran and J. Lee, "Blast loaded plates," *Mar. Struct.,* vol. 22, pp. 99-127, 2009.

[71] A. Kadid, "Stiffened plates subjected to uniform blast loading," *Journal of Civil Engineering and Management,* vol. 14, pp. 155-161, 2008.

[72] B. Lewis and G. Von Elbe, *Combustion, Flames and Explosions of Gases.* Elsevier, 2012.

[73] I. I. Glass, "Shock waves and man." *Shock Waves and Man., by Glass, II.Toronto (Canada): University of Toronto Press, 12 169 p.,* vol. 1, 1974.

[74] P. Sachdev, *Shock Waves & Explosions.* CRC Press, 2016.

[75] K. Spranghers ,K. Vasilakos, D. Lecompte and J. Vantomme "Full-field deformation measurements of aluminum plates under free air blast loading," *Exp. Mech.,* vol. 52, pp. 1371-1384, 2012.

[76] M. Wiehahn, G. Nurick and H. Bowles, "Some insights into the mechanism of the deformation and tearing of thin plates at high strain rates incorporating temperature dependent material properties," *WIT Transactions on the Built Environment,* vol. 48, 2000.

[77] A. Neuberger, S. Peles and D. Rittel, "Scaling the response of circular plates subjected to large and close-range spherical explosions. Part I: Air-blast loading," *Int. J. Impact Eng.,* vol. 34, pp. 859-873, 2007.

[78] N. Rudrapatna, R. Vaziri and M. Olson, "Deformation and failure of blast loaded stiffened plates," *Int. J. Impact Eng.,* vol. 24, pp. 457-474, 2000.

[79] G. Nurick and J. Martin, "Deformation of thin plates subjected to impulsive loading—a review: Part i: theoretical considerations," *Int. J. Impact Eng.,* vol. 8, pp. 159-170, 1989.

[80] N. Jacob *et al*, "Scaling aspects of quadrangular plates subjected to localised blast loads—experiments and predictions," *Int. J. Impact Eng.,* vol. 30, pp. 1179-1208, 2004.

[81] R. Teeling-Smith and G. Nurick, "The deformation and tearing of thin circular plates subjected to impulsive loads," *Int. J. Impact Eng.,* vol. 11, pp. 77-91, 1991.

[82] N. N. Kleinschmit, "A shock tube technique for blast wave simulation and studies of flow structure interactions in shock tube blast experiments," 2011.

[83] S. C. K. Yuen, *Deformation and Tearing of Uniformly Blast loaded Quadrangular Stiffened Plates,* 2000.

[84] G. Nurick, H. Pearce and J. Martin, "The deformation of thin plates subjected to impulsive loading," in *Inelastic Behaviour of Plates and Shells*Anonymous Springer, 1986, pp. 597-616.

[85] G. Nurick and J. Martin, "Deformation of thin plates subjected to impulsive loading—a review part II: experimental studies," *Int. J. Impact Eng.,* vol. 8, pp. 171-186, 1989.

[86] T. Wierzbicki and G. Nurick, "Large deformation of thin plates under localised impulsive loading," *Int. J. Impact Eng.,* vol. 18, pp. 899-918, 1996.

[87] H. Gharababaei and A. Darvizeh, "Experimental and Analytical Investigation of Large Deformation of Thin Circular Plates Subjected to Localized and Uniform Impulsive Loading#," *Mechanics Based Design of Structures and Machines,* vol. 38, pp. 171-189, 2010.

[88] G. Nurick and A. Radford, "Deformation and tearing of clamped circular plates subjected to localised central blast loads," *Recent Developments in Computational and Applied Mechanics: A Volume in Honour of John B.Martin,* pp. 276-301, 1997.

[89] H. Wen, T. Yu and T. Reddy, "A Note on Clamped Circular Plates under Impulsive Loading∗," *Journal of Structural Mechanics,* vol. 23, pp. 331-342, 1995.

[90] S. Menkes and H. Opat, "Broken beams," *Exp. Mech.,* vol. 13, pp. 480-486, 1973.

[91] G. Nurick and G. Shave, "The deformation and tearing of thin square plates subjected to impulsive loads—an experimental study," *Int. J. Impact Eng.,* vol. 18, pp. 99-116, 1996.

[92] N. Jones, "Recent studies on the dynamic plastic behavior of structures," *Appl. Mech. Rev.,* vol. 42, pp. 95-115, 1989.

[93] G. Nurick and J. Martin, "Deformation of thin plates subjected to impulsive loading—a review: Part i: theoretical considerations," *Int. J. Impact Eng.,* vol. 8, pp. 159-170, 1989.

[94] A. Paykani, M. Khosravi, M Saeimi-Sadigh and M. Mahmoodi-Kaleidar "Dynamic analysis and design of V-shape plates under blast loading." *Journal of Vibroengineering,* vol. 15, 2013.

[95] E. G. Pickering, S. Chung Kim Yuen and G.N Nurick "The response of quadrangular plates to buried charges," *Int. J. Impact Eng.,* vol. 49, pp. 103-114, 2012.

[96] N. Ranwaha, *The use of Cellular Materials to Alleviate the Damage from Blast-Induced Fragments,* 2014.

[97] S. C. K. Yuen *et al*, "The response of circular plates to repeated uniform blast loads," in *Key Engineering Materials,* 2013, pp. 44-47.

[98] S. C. K. Yuen, G. Nurick and M. C. du Plessis, "Response of sandwich panels with tubular cores to blast load," in *Applied Mechanics and Materials,* 2014, pp. 581-585.

[99] R. Matthews, *Investigating the Influence of Thermomechanical Variables on Ridging in Aisi 430 Stainless Steel,* 2001.

[100] N. Machio, *Influence of Composition and Thermomechanical Processing on Microstructure Evolution in AISI 430 Ferritic Stainless Steel (FSS),* 1998.

[101] B. Jha, P. Jha and C. Singh, "Process Technology for the Continuous hot band annealing of 17% Cr ferritic stainless steel," *Journal of Materials Engineering and Performance,* vol. 11, pp. 180-186, 2002.

[102] T. Maitland and S. Sitzman, *Electron Backscatter Diffraction (EBSD) Technique and Materials Characterization Examples.* Springer Berlin, 2007.

[103] S. I. Wright and M. M. Nowell, "EBSD image quality mapping," *Microscopy and Microanalysis,* vol. 12, pp. 72-84, 2006.

[104] P. Session, "Scientific Program MicroscopyAND Microanalysis," 2004.

[105] C. Panait, W. Bendick and A. Fuchsmann "Study of the microstructure of the Grade 91 steel after more than 100,000 h of creep exposure at 600 C," *Int. J. Pressure Vessels Piping,* vol. 87, pp. 326-335, 2010.

[106] N. Jacob, G. Nurick and G. Langdon, "The effect of stand-off distance on the failure of fully clamped circular mild steel plates subjected to blast loads," *Eng. Struct.,* vol. 29, pp. 2723-2736, 2007.

[107] S. C. K. Yuen and G. Nurick, "The significance of the thickness of a plate when subjected to localised blast loads," in *Proc 16th Int Symp Military Aspects of Blast and Shock,* 2000, pp. 491-499.

[108] B. M. Thomas, *The Effect of Boundary Conditions on the Failure of Thin Plates Subjected to Impulsive Loading,* 1995.

[109] T. F. Henchie, S. Chung Kim Yuen and N. Ranwaha "The response of circular plates to repeated uniform blast loads: An experimental and numerical study," *Int. J. Impact Eng.,* vol. 74, pp. 36-45, 2014.

[110] M. P. Smith, *Microstructural Analysis of Plates with Large Strains as a Result of Central Localised Blast loading,* 1999.

[111] M. S. Ahmad, *Study of Dynamic Behaviour of Multi-Layered Structures Subjected to Blast loading, PhD thesis, UCT,* 2012.

[112] M. P. Smith, *Microstructural Analysis of Plates with Large Strains as a Result of Central Localised Blast loading, MSc thesis, UCT* 1999.

[113] K. Hartley, J. Duffy and R. Hawley, "Measurement of the temperature profile during shear band formation in steels deforming at high strain rates," *J. Mech. Phys. Solids,* vol. 35, pp. 283-301, 1987.

[114] J. A. Rodríguez-Martínez *et al*, "Experimental and numerical analysis of the martensitic transformation in AISI 304 steel sheets subjected to perforation by conical and hemispherical projectiles," *Int. J. Solids Structures,* vol. 50, pp. 339-351, 2013.

[115] W. D. Callister and D. G. Rethwisch, *Materials Science and Engineering: An Introduction.* Wiley New York, 2007.

[116] M. Sheen, *Static Recrystallization Behaviour of AISI 304 Stainless Steel during Hot Rolling Intervals,MSc thesis,UCT,*2001

[117] Kumar, K. S., H. Van Swygenhoven, and S. Suresh. "*Mechanical behaviour of nanocrystalline metals and alloys*." *Acta Materialia* 51.19 (2003): 5743-5774.

[118] Arzt, El. "*Size effects in materials due to microstructural and dimensional constraints: a comparative review*." *Acta materialia* 46.16 (1998): 5611-5626.

APPENDIX A

A.1 Material Specification Certificate

The material used for this study is 430 Stainless Steel cut from stainless steel sheets with the material inspection certificate indicated below.

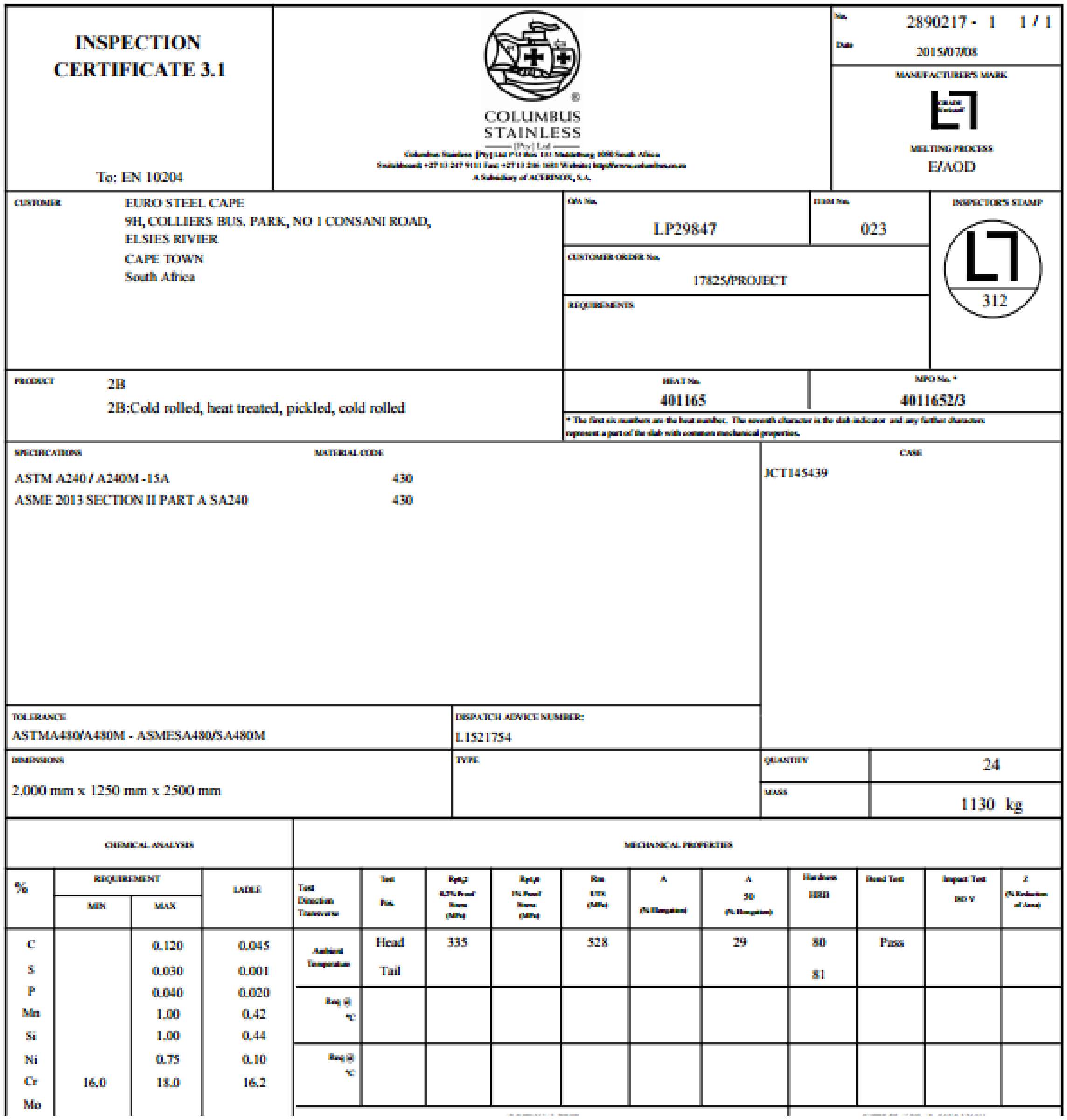

INSPECTION CERTIFICATE 3.1

To: EN 10204

COLUMBUS STAINLESS
(Pty) Ltd
Columbus Stainless [Pty] Ltd P O Box 133 Middelburg 1050 South Africa
Switchboard: +27 13 247 9111 Fax: +27 13 246 1681 Website: http://www.columbus.co.za
A Subsidiary of ACERINOX, S.A.

No.	2890217 - 1 1 / 1
Date	2015/07/08
MANUFACTURER'S MARK	
MELTING PROCESS	E/AOD
CUSTOMER	EURO STEEL CAPE 9H, COLLIERS BUS. PARK, NO 1 CONSANI ROAD, ELSIES RIVIER CAPE TOWN South Africa
O/A No.	LP29847
ITEM No.	023
CUSTOMER ORDER No.	17825/PROJECT
REQUIREMENTS	
INSPECTOR'S STAMP	312
PRODUCT	2B 2B:Cold rolled, heat treated, pickled, cold rolled
HEAT No.	401165
MPO No. *	4011652/3

* The first six numbers are the heat number. The seventh character is the slab indicator and any further characters represent a part of the slab with common mechanical properties.

SPECIFICATIONS	MATERIAL CODE
ASTM A240 / A240M -15A	430
ASME 2013 SECTION II PART A SA240	430

CASE	JCT145439
TOLERANCE	ASTMA480/A480M - ASMESA480/SA480M
DISPATCH ADVICE NUMBER:	L1521754
DIMENSIONS	2.000 mm x 1250 mm x 2500 mm
TYPE	
QUANTITY	24
MASS	1130 kg

CHEMICAL ANALYSIS

%	REQUIREMENT MIN	REQUIREMENT MAX	LADLE
C		0.120	0.045
S		0.030	0.001
P		0.040	0.020
Mn		1.00	0.42
Si		1.00	0.44
Ni		0.75	0.10
Cr	16.0	18.0	16.2
Mo			

MECHANICAL PROPERTIES

Test Direction Transverse	Test Pos.	Rp0,2 0,2% Proof Stress (MPa)	Rp1,0 1% Proof Stress (MPa)	Rm UTS (MPa)	A (% Elongation)	A 50 (% Elongation)	Hardness HRB	Bend Test	Impact Test ISO V	Z (% Reduction of Area)
Ambient Temperature	Head	335		528		29	80	Pass		
	Tail						81			
Req @ °C										
Req @ °C										

Figure A.1: A material inspection certificate for the material

A.2 Tensile Testing Raw Data

Tensile tests were carried out on dog bone specimens cut out from a sheet of AISI 430 Stainless Steel metal. The tensile tests were performed on the Zwick/Roell 1484 Mechanical Testing machine. The raw data for the tensile tests performed are presented in this section and also include the graphs drawn without the removal of machine compliance.

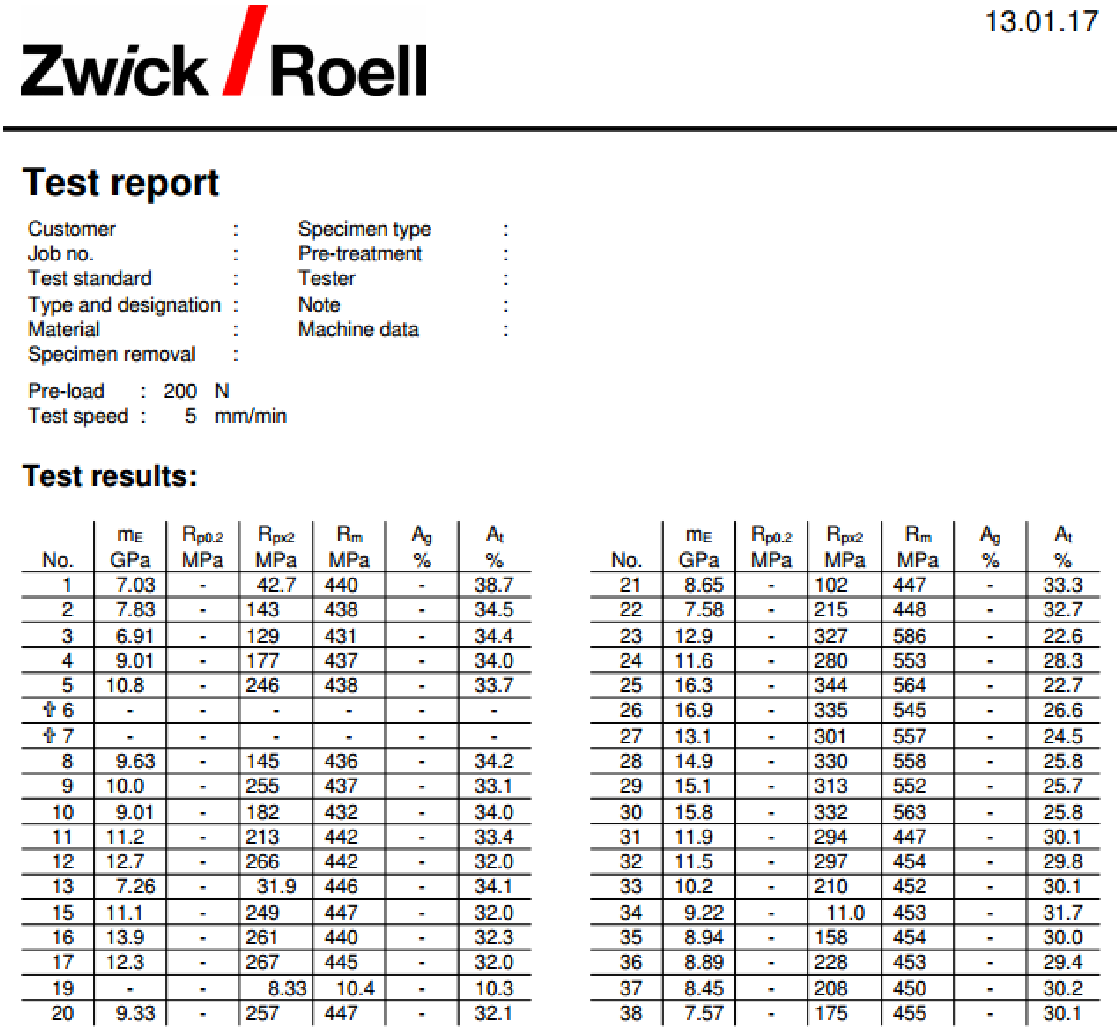

Zwick / Roell

13.01.17

Test report

Customer :
Job no. :
Test standard :
Type and designation :
Material :
Specimen removal :
Specimen type :
Pre-treatment :
Tester :
Note :
Machine data :

Pre-load : 200 N
Test speed : 5 mm/min

Test results:

No.	m_E GPa	$R_{p0.2}$ MPa	R_{px2} MPa	R_m MPa	A_g %	A_t %
1	7.03	-	42.7	440	-	38.7
2	7.83	-	143	438	-	34.5
3	6.91	-	129	431	-	34.4
4	9.01	-	177	437	-	34.0
5	10.8	-	246	438	-	33.7
⇧ 6	-	-	-	-	-	-
⇧ 7	-	-	-	-	-	-
8	9.63	-	145	436	-	34.2
9	10.0	-	255	437	-	33.1
10	9.01	-	182	432	-	34.0
11	11.2	-	213	442	-	33.4
12	12.7	-	266	442	-	32.0
13	7.26	-	31.9	446	-	34.1
15	11.1	-	249	447	-	32.0
16	13.9	-	261	440	-	32.3
17	12.3	-	267	445	-	32.0
19	-	-	8.33	10.4	-	10.3
20	9.33	-	257	447	-	32.1
21	8.65	-	102	447	-	33.3
22	7.58	-	215	448	-	32.7
23	12.9	-	327	586	-	22.6
24	11.6	-	280	553	-	28.3
25	16.3	-	344	564	-	22.7
26	16.9	-	335	545	-	26.6
27	13.1	-	301	557	-	24.5
28	14.9	-	330	558	-	25.8
29	15.1	-	313	552	-	25.7
30	15.8	-	332	563	-	25.8
31	11.9	-	294	447	-	30.1
32	11.5	-	297	454	-	29.8
33	10.2	-	210	452	-	30.1
34	9.22	-	11.0	453	-	31.7
35	8.94	-	158	454	-	30.0
36	8.89	-	228	453	-	29.4
37	8.45	-	208	450	-	30.2
38	7.57	-	175	455	-	30.1

Series graph:

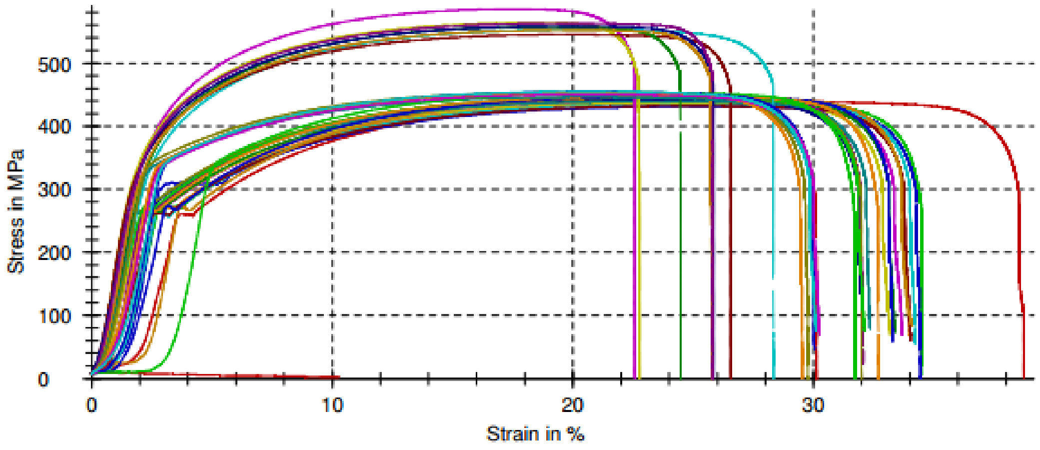

Figure A.2 Stress-Strain Raw Data

APPENDIX B

B.1 Horizontal Ballistic Pendulum

The blast tests were performed with the use of a ballistic pendulum. The pendulum used two different clamp frames for the two loading conditions. The resultant impulse was determined by the consideration of all the variables. The ballistic pendulum with two types of clamping rigs for both the localised and the uniform conditions is represented by Figure B.1.

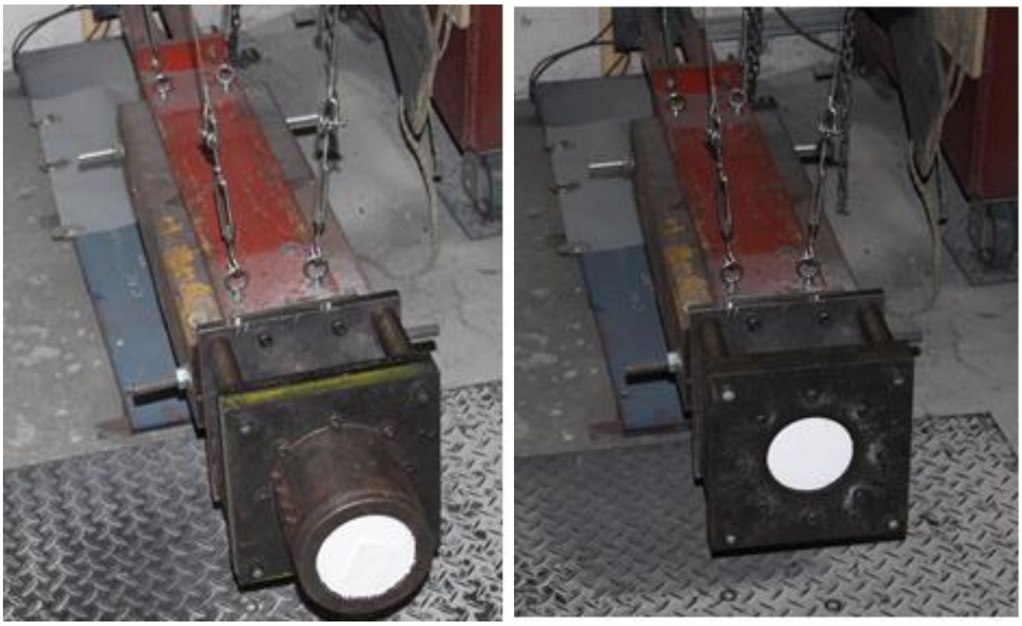

a)Uniform b) Localised

Figure B.1: Ballistic Pendulum with two different clamp rigs a) uniform b) localised

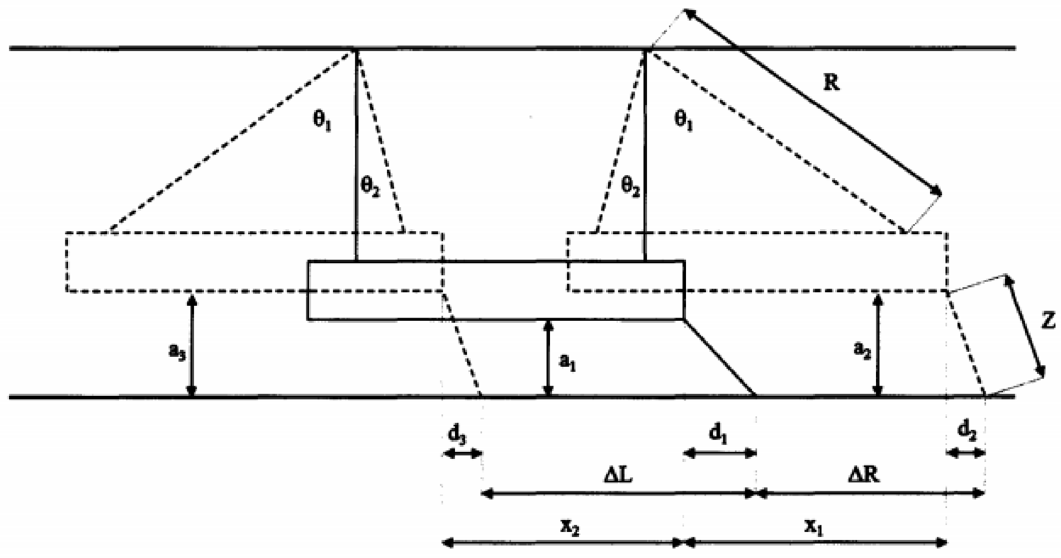

Figure B.2: A Schematic of the horizontal ballistic pendulum

From Figure A3, the horizontal distance between the end of the pendulum and the pen is given as:

$$d_1 = \sqrt{Z^2 - a^2} \qquad \text{Eq. B.1}$$

While at the pendulum's maximum amplitude, the distance decreases and is given as:

$$d_1 = \sqrt{Z^2 - a^2} \qquad \text{Eq.B.2}$$

In blast testing the pendulum oscillates at low amplitudes, giving a small angle on the suspension wires and therefore:

$$x_1 = R\theta \qquad \text{Eq.B.3}$$

$$y = \frac{R\theta}{2} \qquad \text{Eq.B.4.}$$

Substituting equation B.3 into B.2:

$$y = \frac{x_1^2}{2R} \qquad \text{Eq.B.5}$$

From Figure B.3:

$$d_2 = [Z^2 - (a - \frac{x_1^2}{2R})^2]^{0.5} \qquad \text{Eq. B.6}$$

$$x_1 = \Delta R + d_1 - d_2 \qquad \text{Eq. B.7}$$

$$x_2 = \Delta L - d_1 + d_2 \qquad \text{Eq. B.8}$$

$$x_1 = \Delta R + \sqrt{Z^2 - a^2} - [Z^2 - (a + \frac{x_1^2}{2R})^2]^2 \qquad \text{Eq.B.9}$$

$$x_1 = \Delta L - \sqrt{Z^2 - a^2} + [Z^2 - (a + \frac{x_1^2}{2R})^2]^2 \text{ E} \qquad \text{Eq.B.10}$$

$$\mathrm{X} + 2\beta\mathrm{X} + \omega_n\mathrm{X} = 0 \qquad \text{Eq. B.11}$$

B.2 Ballistic Pendulum Theory

The ballistic pendulum theory uses a pendulum that swings in a two-dimensional motion and that satisfies an amplitude equal to sin θ≈θ. This is displayed by figure 2.6 below:

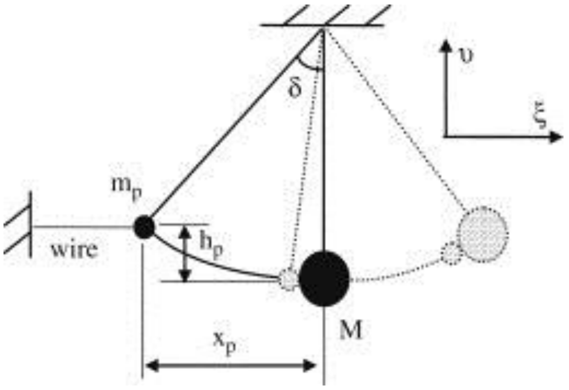

Figure 2.6: A schematic of simple pendulum

A pendulum undergoes a simple harmonic motion. β is the damping coefficient. The two-dimensional motion of the pendulum has a specific angular period depending on the number of oscillations. This is represented as ω_n.

β and ω_n are defined as:

$$\beta = \frac{C}{2m_p} \text{ and } \omega_n = \frac{2\pi}{T}$$

where C is the damping coefficient, m_p is the pendulum's total mass and T is the period of the swing.

The solution to Eq B.11 is given by the equation:

$$X(t) = \frac{(e^{-\beta t})x_o \sin(\omega_d t)}{w_d} \qquad \text{Eq.B.12}$$

where x_o is the initial velocity of the pendulum and w_d is calculated as:

$$w_d = \sqrt{w_n^2 - \beta^2} \qquad \text{Eq. B.13}$$

x_1 is the maximum positive displacement of the pendulum while x_2 is the maximum negative displacement. The period at which the displacement point x_1 occurs is $t = \frac{T}{4}$ and that of x_2 is at $t = \frac{3T}{4}$ and substituting these period values on equation (2) gives

$$x_1 = \frac{x_o T}{2\pi} e^{-\frac{\beta T}{4}} \qquad \text{Eq. B.14}$$

$$x_2 = \frac{x_o T}{2\pi} e^{-\frac{3\beta T}{4}} \qquad \text{Eq.B.15}$$

β is obtained by dividing x_1 by x_2 as represented by equation 6 below :

$$\beta = \frac{2}{T} \ell n \frac{x_1}{x_2} \qquad \text{Eq.B.16}$$

Substituting equation (6) into equation (2) gives:

$$x_o = \frac{2\pi}{T} x_1 e^{-\frac{\beta T}{4}} \qquad \text{Eq.B.17}$$

The Impulse is then obtained to be: $I = m_p x_o$

Applying this method for a blast test using the ballistic pendulum would have to include an account of the distances recorded by an attached pen. These are ΔR (front distance) and ΔL (back distance).

APPENDIX C

Drawings

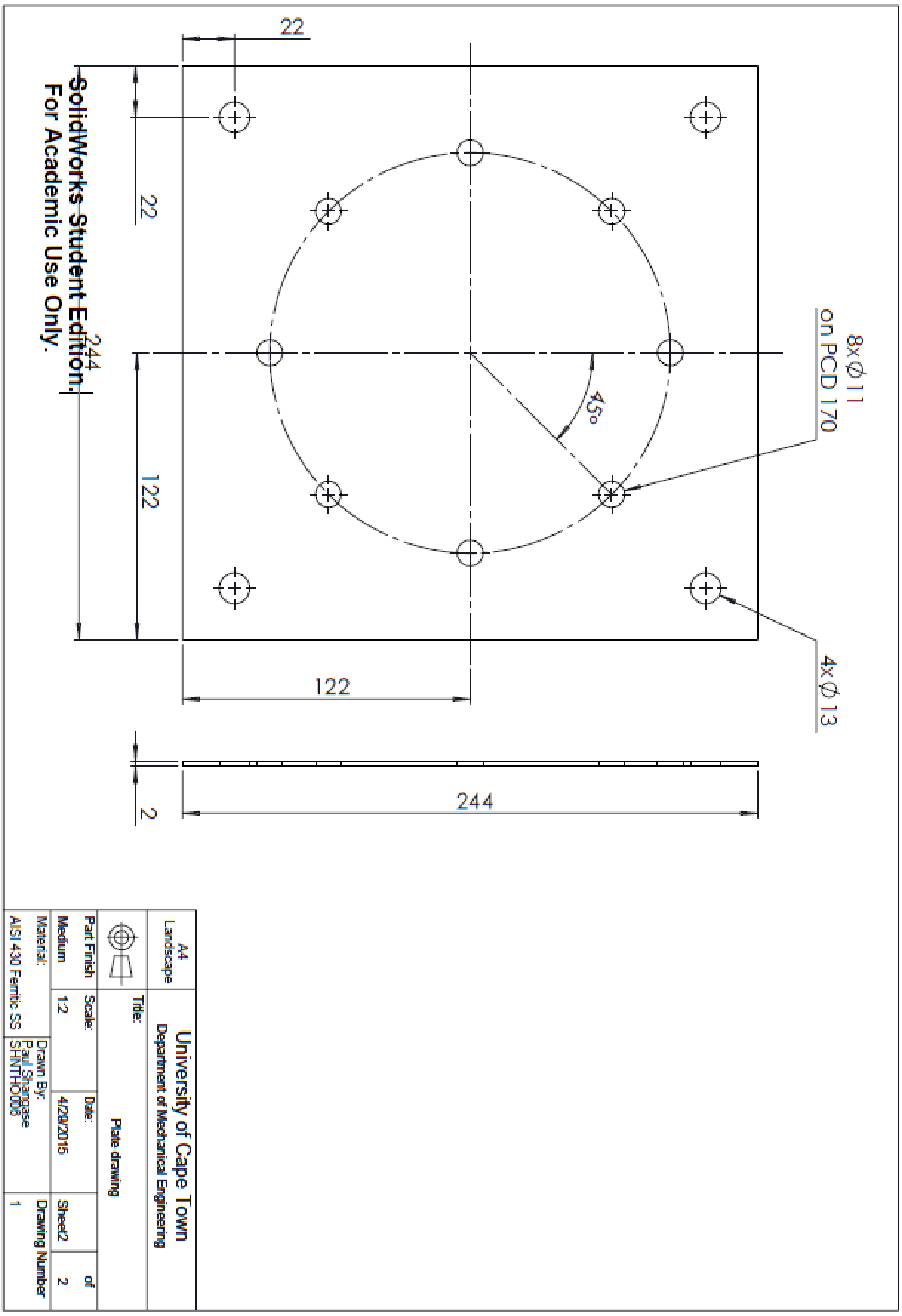

Tensile Dog Bone Drawing

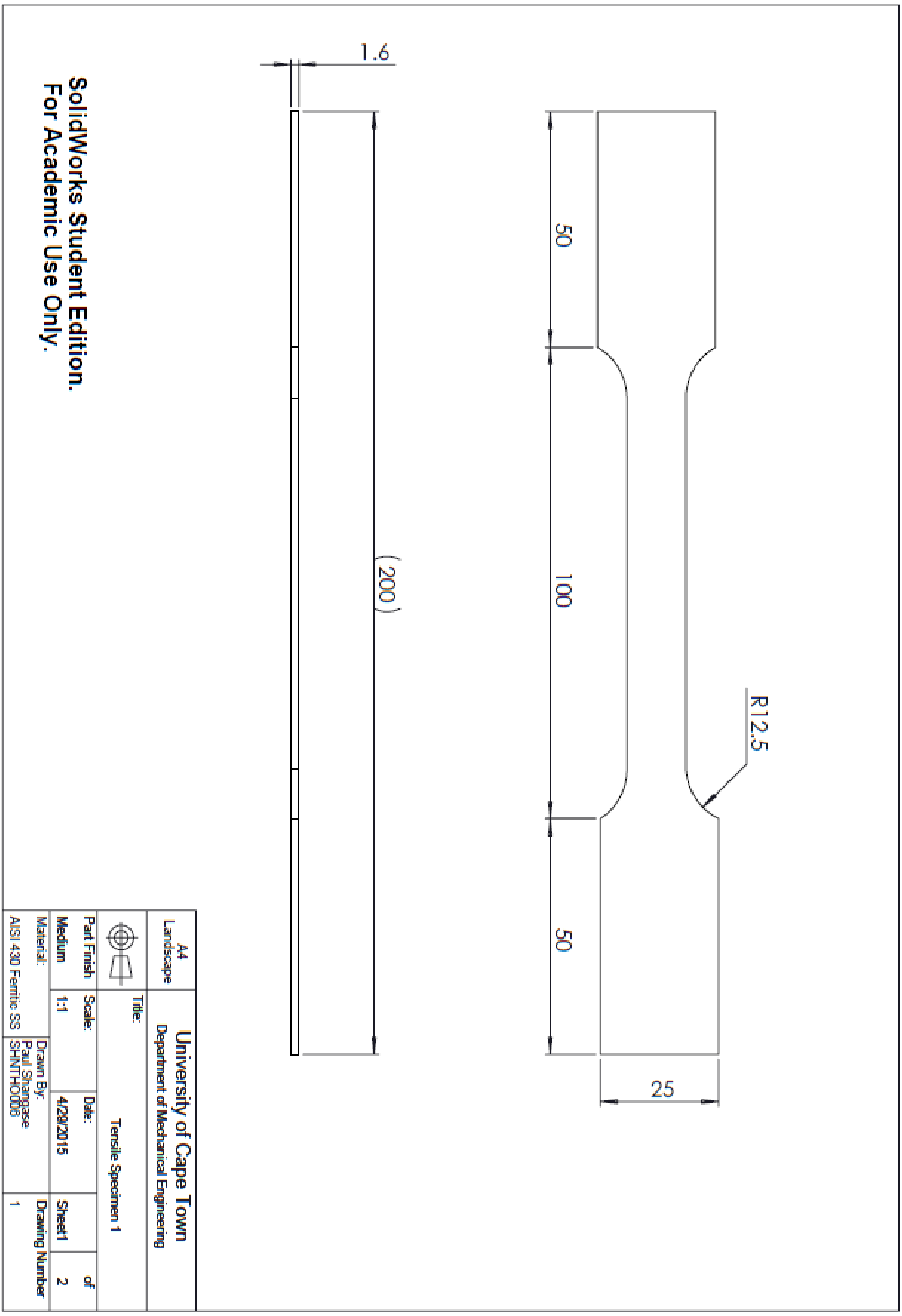

APPENDIX D

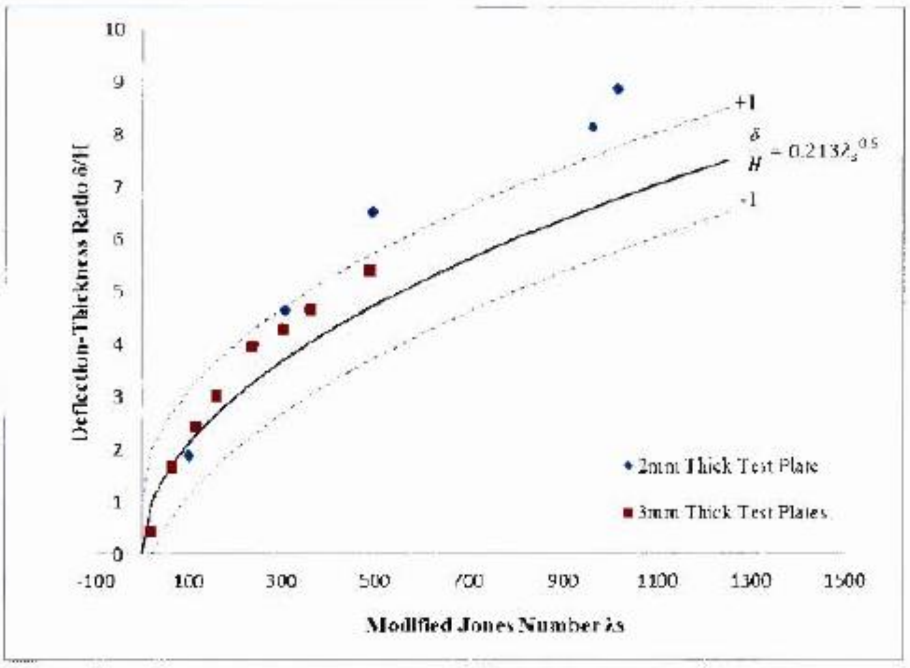

a) Single blast loads

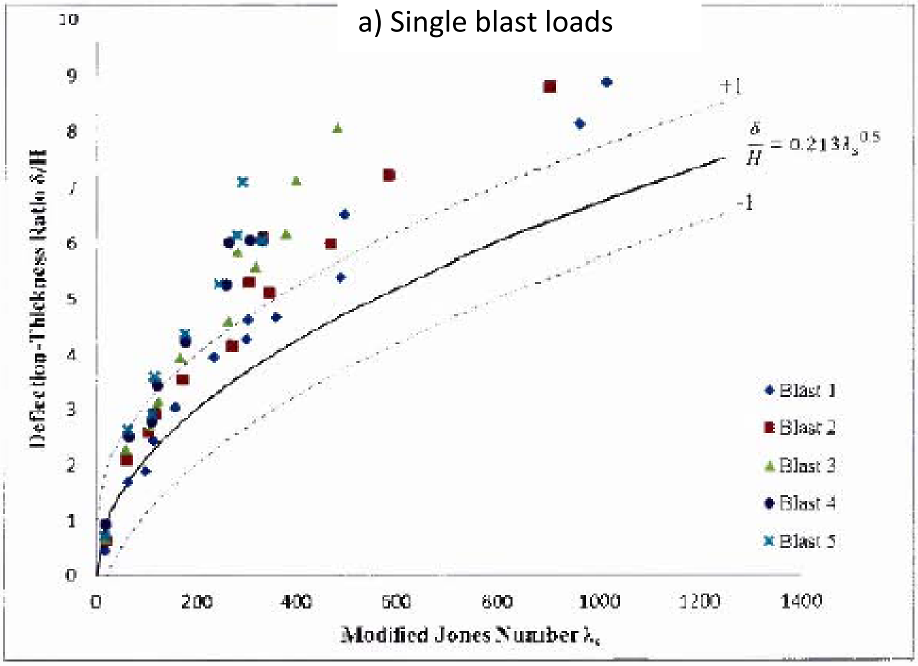

b) Repeated blast loads

Figure D3: Graphs of modified jones number vs deflection-thickness ratio obtained by Henchie *et al*.

D.2 Equivalent Circle Diameters

The equivalent circle diameter method was used to determine the grain size change between the microstructures and to change the grain morphology changes along the plate profile. The workings for the four plate compared for both the localised condition and the uniform are attached to this appendix.

D.3 Stitched Images

Stitched micrographs of the adiabatic shear band in chapter 5 are presented in Figure D4.

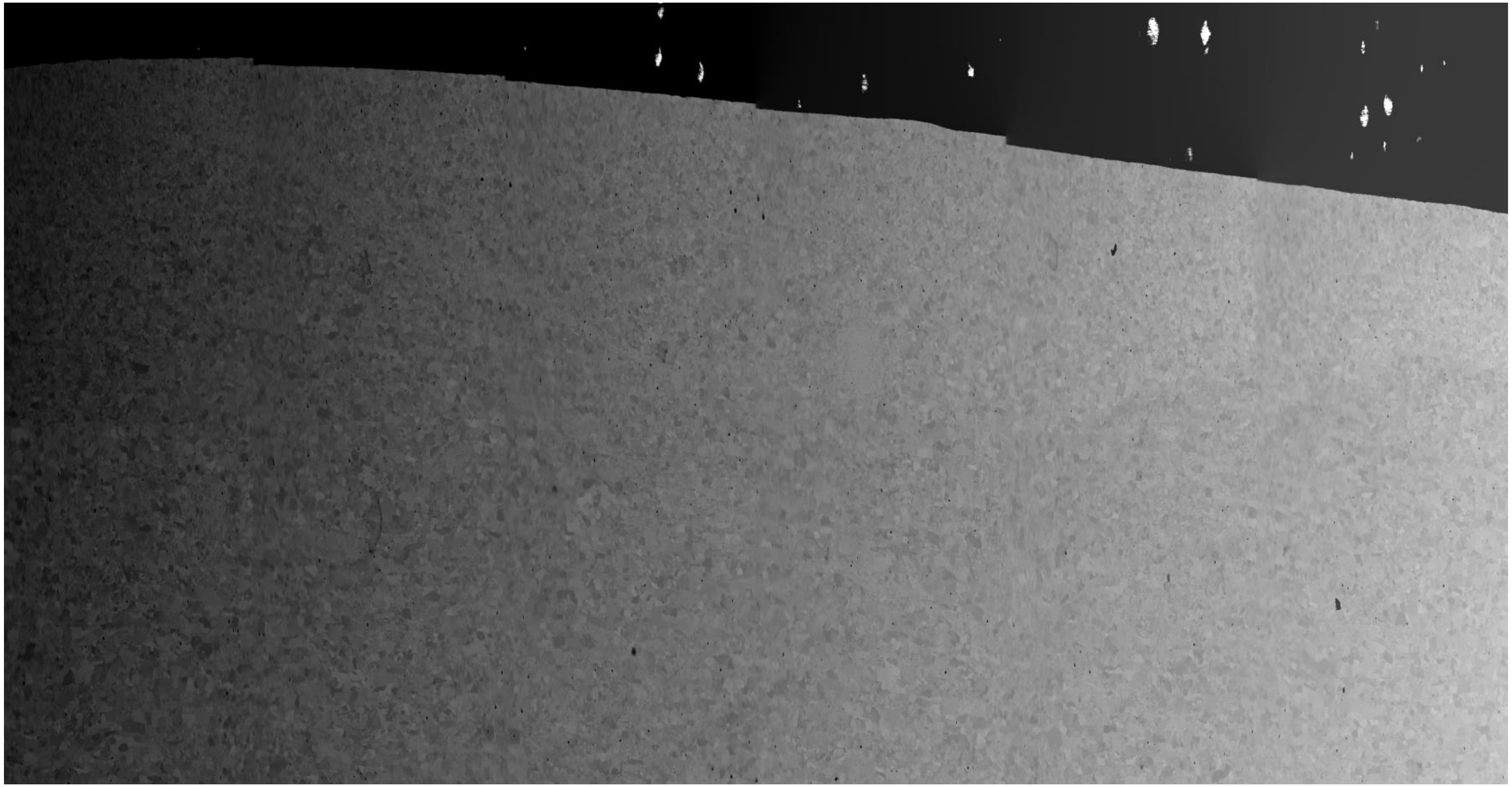

Figure D4: Stitched micrograph of a shear band.

4A

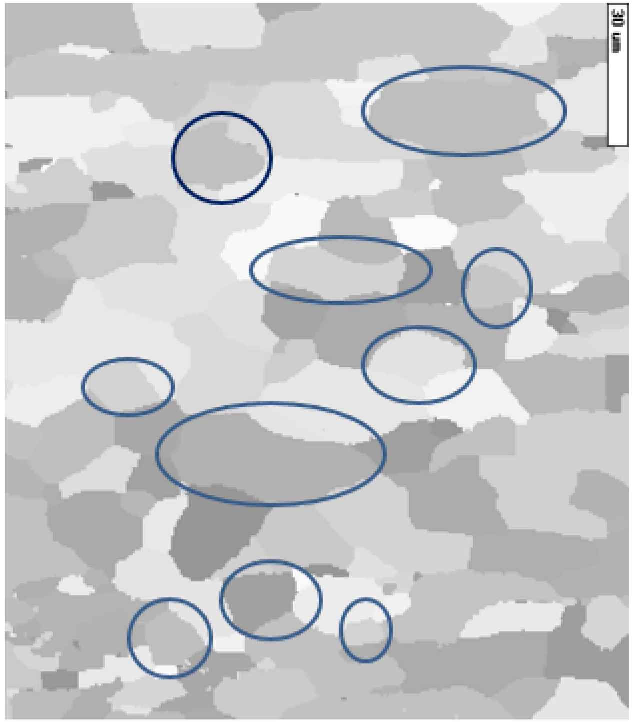

Image is rotated by 90 degrees.Therefore x and y in this table must be swapped.Aspect ratio is manually calculated

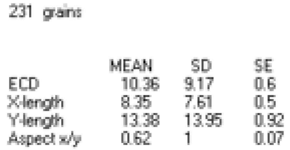

```
231  grains


              MEAN     SD      SE
ECD            10.36   9.17    0.6
X-length       8.35    7.61    0.5
Y-length       13.38   13.95   0.92
Aspect x/y     0.62    1       0.07
```

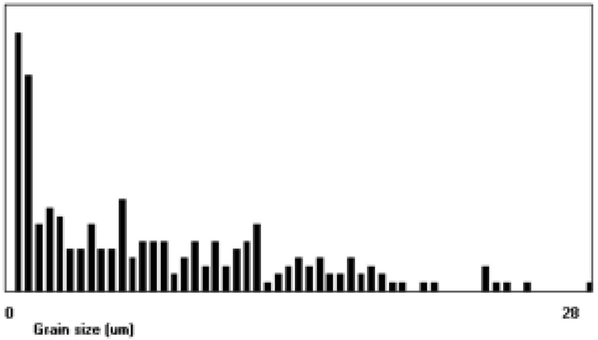

4C

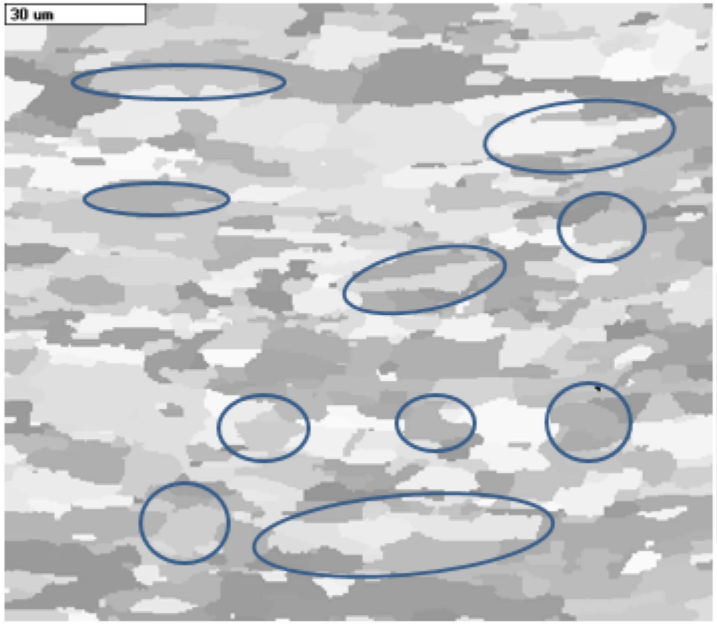

```
646  grains

              MEAN    SD     SE
ECD           6.07    4.79   0.19
X-length      9.85    9.66   0.38
Y-length      4.01    3.44   0.14
Aspect x/y    2.45    2.83   0.11
```

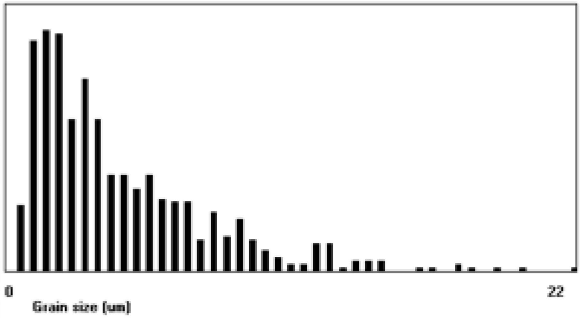

4E

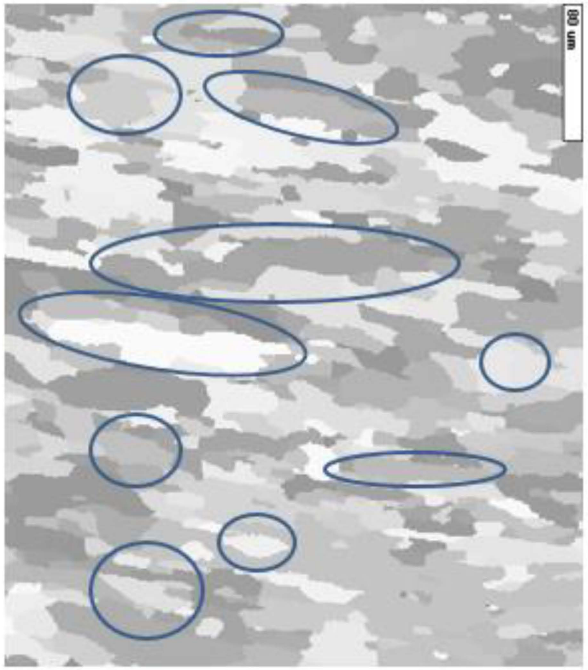

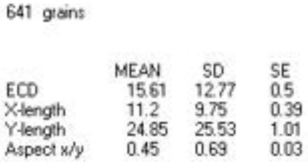

```
641  grains

              MEAN     SD      SE
ECD           15.61    12.77   0.5
X-length      11.2     9.75    0.39
Y-length      24.85    25.53   1.01
Aspect x/y    0.45     0.69    0.03
```

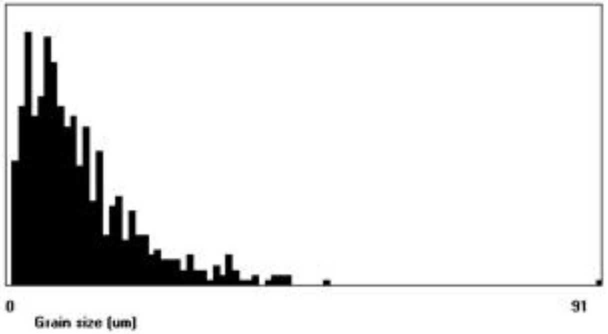

3C

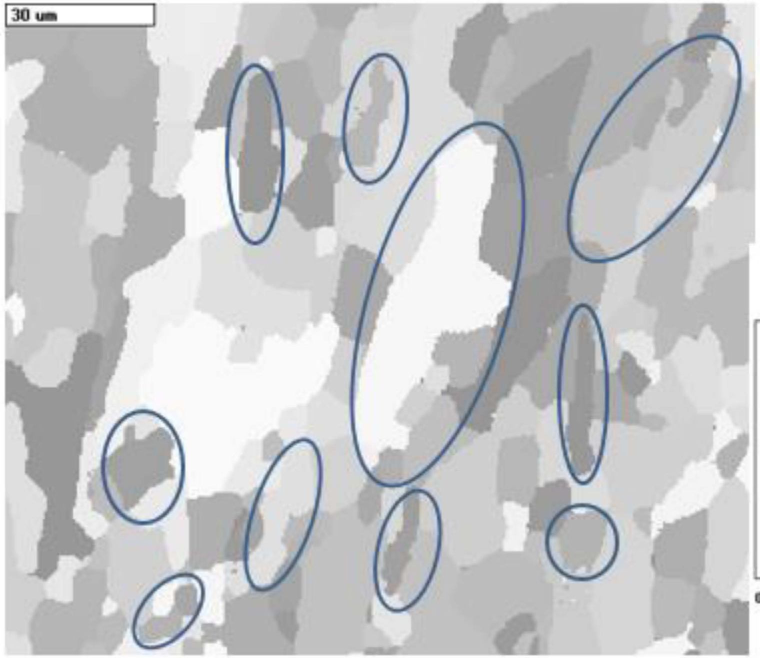

```
288  grains

               MEAN     SD      SE
ECD             9.08    8.15    0.48
X-length        7.79    7.46    0.44
Y-length       11.75   12.28    0.72
Aspect x/y      0.66    1.12    0.07
```

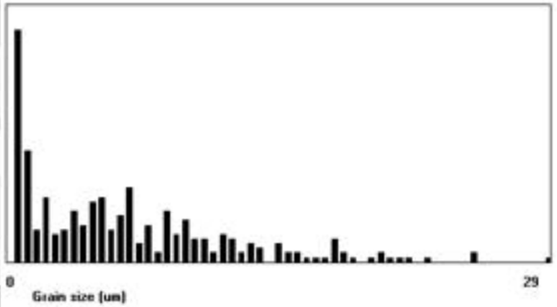

3E

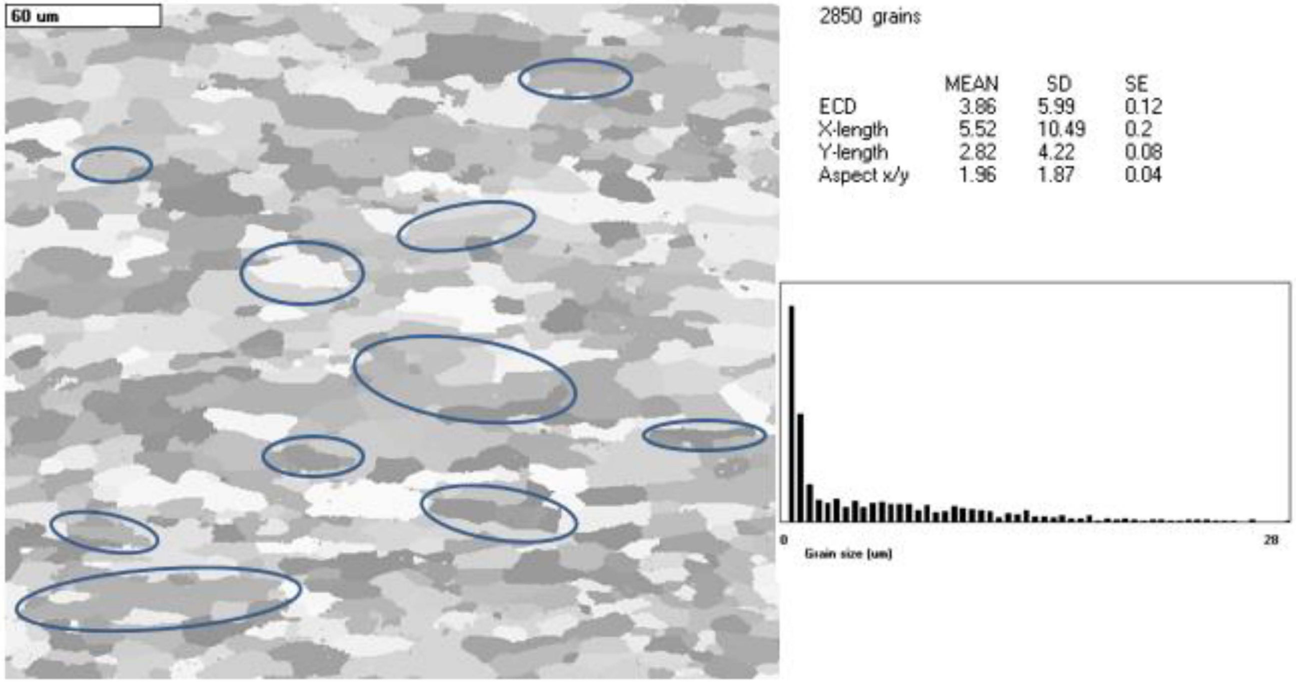

```
2850  grains

              MEAN    SD      SE
ECD           3.86    5.99    0.12
X-length      5.52    10.49   0.2
Y-length      2.82    4.22    0.08
Aspect x/y    1.96    1.87    0.04
```

11E

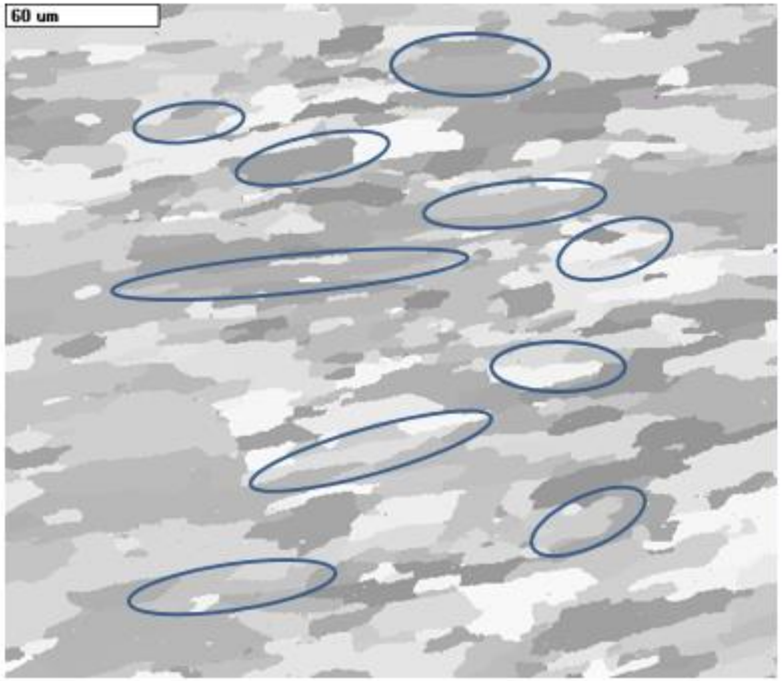

```
1218  grains

               MEAN     SD      SE
ECD             6.6     9.21    0.27
X-length       11.63   19.49    0.56
Y-length        4.53    6.45    0.18
Aspect x/y      2.57    2.32    0.07
```

11C

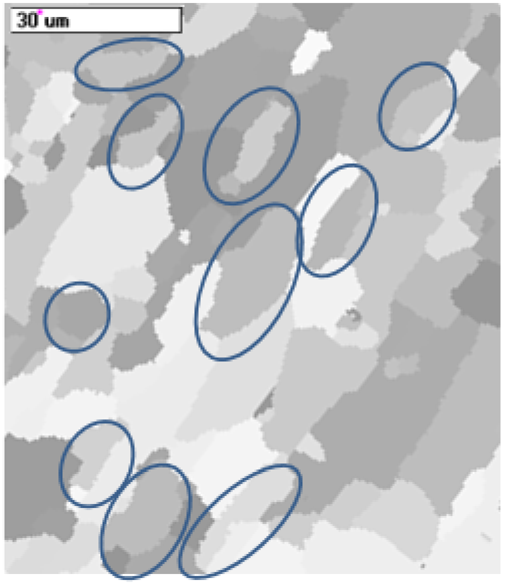

```
290  grains

              MEAN     SD      SE
ECD            9.1     8.05    0.47
X-length       7.54    6.54    0.38
Y-length      11.76   12.66    0.74
Aspect x/y     0.64    1.06    0.06
```

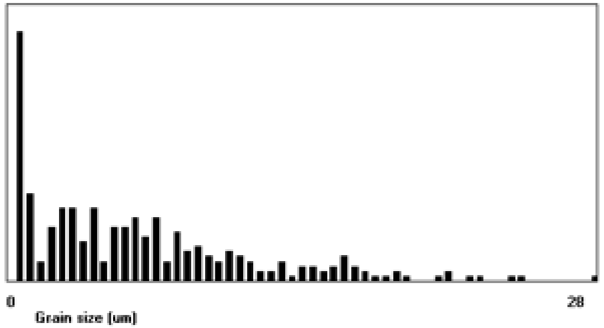

6A

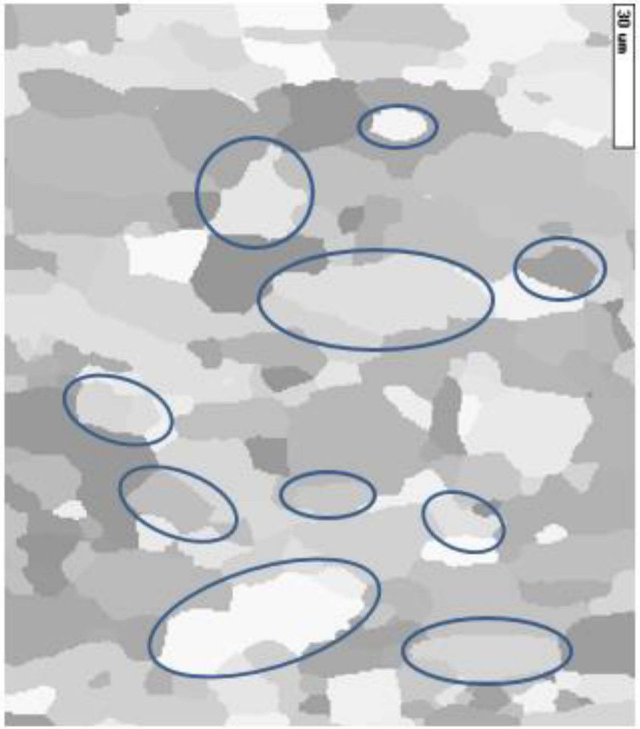

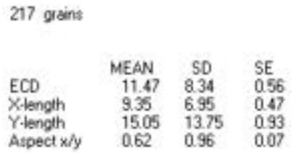

```
217  grains

                MEAN     SD      SE
ECD              11.47   8.34    0.56
X-length         9.35    6.95    0.47
Y-length         15.05   13.75   0.93
Aspect x/y       0.62    0.96    0.07
```

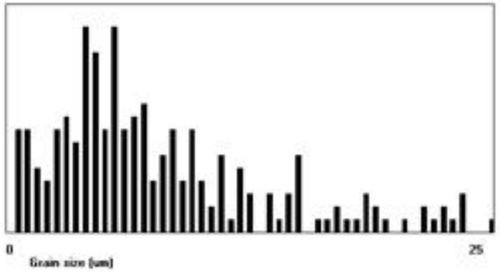

6C

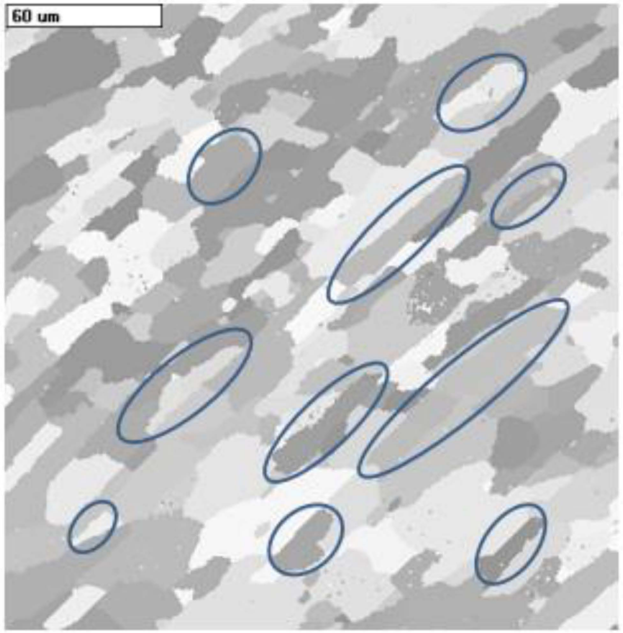

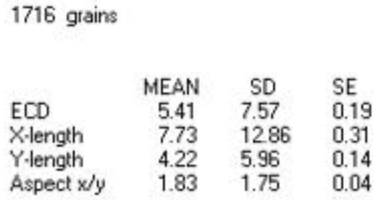

```
1716  grains

               MEAN     SD      SE
ECD            5.41     7.57    0.19
X-length       7.73     12.86   0.31
Y-length       4.22     5.96    0.14
Aspect x/y     1.83     1.75    0.04
```